



*Faculty of Materials Science and Engineering  
University of Miskolc*

ANTAL KERPELY DOCTORAL SCHOOL OF  
MATERIALS SCIENCE & TECHNOLOGY



**Doctoral Dissertation**

**Molecular dynamics aided green transition of the  
chemical industry.**

**Molecular-level understanding of membrane permeation of  
some chemicals and the phase diagram of 1,3-butadiene.**

**Zsófia Borbála Rózsa**

*Supervisor*

**Dr. Milán Szóri**

Institute of Chemistry

University of Miskolc

**Miskolc, Hungary**

**2022**

*I'm questioning my education  
Rewind and what does it show?  
Could be, the truth it becomes you  
I'm a seed, wondering why it grows...  
(Pearl Jam – Education)*

# TABLE OF CONTENTS

1	Introduction .....	1
1.1	Biological Membranes .....	2
1.1.1	Structure of Biological Membranes.....	2
1.1.2	Passive Transport Phenomena .....	5
1.1.3	Modeling Membrane Systems .....	6
1.1.4	Biological Membranes and Small Molecule Interactions Inspected by Molecular Dynamics Simulations .....	7
1.2	Species From The Classical Chemical Industrial Era. Passive Membrane Permeation of 1,4-dioxane, Morpholine, Oxane and Phenol .....	9
1.3	Species from the Potential Future of Chemical Syntheses. The Case of the CO <sub>2</sub> – 1,3-Butadiene Reaction .....	11
1.4	The Vapor-Liquid Equilibria and Supercritical Phase of 1,3-Butadiene.....	14
1.5	Motivation of this Thesis .....	15
2	Methods.....	16
2.1	Molecular Dynamics Simulations.....	16
2.1.1	Parameterization and Calculation of the Potential Energy.....	16
2.1.2	Algorithms of Molecular Dynamics Simulations.....	21
2.1.3	Molecular Simulation of Different Ensembles.....	23
2.1.4	General Protocol for Classical MD Simulations .....	25
2.2	Free Energy Calculations.....	25
2.2.1	Concepts of thermodynamic free energy.....	25
2.2.2	Free energy difference of states.....	26
2.2.3	Estimation of free energy .....	28
2.2.4	Applied methods for free energy calculations.....	29
2.3	Two-phase Molecular Dynamics (2φMD) simulations .....	34
2.3.1	Voronoi tessellation (VT) based density calculation.....	34
2.3.2	Phase Determination.....	34

2.4	Analysis of Membrane Parameters .....	36
2.4.1	Membrane Structural Parameters .....	36
2.4.2	Orientation of Molecules in the Membrane Vicinity.....	38
3	Computational Details.....	40
3.1	Transmembrane Penetration Mechanism of NSO-HET Molecules, 1,4-Dioxane, Phenol, Morpholine and Oxane .....	40
3.1.1	System Preparation .....	40
3.1.2	Parameters of MD simulations .....	40
3.1.3	Free Energy of Permeation .....	41
3.2	Effects of the Derivatives of the CO <sub>2</sub> and 1,3-Butadiene Reaction on Biomembranes .....	42
3.2.1	System Preparation .....	42
3.2.2	Parameters of MD simulations .....	42
3.2.3	Free Energy Calculations.....	43
3.3	Vapor Liquid Equilibrium and Supercritical Phase of 1,3-Butadiene .....	44
3.3.1	System Preparation .....	44
3.3.2	Two-phase Molecular Dynamics (2φMD) simulations.....	45
3.3.3	Supercritical phase simulations .....	46
3.4	Validation.....	46
3.4.1	CHARMM and OPLS-AA lipid force fields.....	46
3.4.2	Cut-off dependence of the density of 1,3-butadiene.....	47
4	Results and Discussion.....	49
4.1	Transmembrane Penetration Mechanism of NSO-HET Molecules. 1,4-Dioxane, Phenol, Morpholine and Oxane .....	49
4.1.2	The Effect of NSO-HETs on Structural Membrane Parameters .....	51
4.1.3	WT-MD based free energy profiles of NSO-HETs.....	53
4.1.4	Concentration Dependence of Free Energy of Permeation. 1,4-dioxane and phenol. ....	54

4.1.5	Free energy profile of penetrating water molecules in the presence of NSO-HETs. ....	56
4.1.6	Detailed analysis of the effect of 1,4-dioxane on DPPC model membranes. ....	60
4.1.7	Summary and Conclusions .....	68
4.2	Effects of the Derivatives of the CO <sub>2</sub> and 1,3-Butadiene Reaction on Biomembranes.....	69
4.2.1	Predicted properties of the studied organic molecules .....	69
4.2.2	Structural changes of DPPC membranes induced by the studied molecules .....	71
4.2.3	Free energy profiles of the studied organic compounds.....	76
4.2.4	Summary and Conclusions .....	78
4.3	Conclusions of membrane permeation studies .....	79
4.4	Vapor Liquid Equilibrium and Supercritical Phase of 1,3-Butadiene .....	83
4.4.1	VLE and critical parameters of 1,3-butadiene.....	83
4.4.2	Density based calculation of the critical temperature and density .....	84
4.4.3	Critical parameters based on thermochemical properties.....	86
4.4.4	Partitioning of molecules.....	87
4.4.5	Temperature and pressure dependence of the specific surface area of 1,3-butadiene.....	90
4.4.6	Summary and Conclusions .....	91
5	Summary .....	93
6	Összefoglaló.....	95
7	New Scientific Results – Theses .....	97
8	References .....	100
9	List of Publications.....	119

# 1 INTRODUCTION

To this day, over 350 000 chemicals and mixtures of chemicals are registered for production and use [1], which annual production rate exceeds  $10^8$  tons. [2] While chemicals are essential to our life standards, a non-negligible portion of the produced substances is released into the environment due to improper handling during their production, usage and disposal. Environmental exposure is a key contributor to diseases, premature death and the alteration of ecosystems, chemical pollution is also considered as one of the major factor in climate change and responsible for disintegration of the biosphere. [3], [4]

Information on emerging compounds has been collected in several databases. For instance, the CECscreen annotation database [5] contains information on chemicals with emerging environmental and health concerns, in which over 70 000 structures were identified, and their Phase I metabolites were simulated, resulting in further 300 000 concerning structures. Another example is the suspect lists of the NORMAN network [6], [7], developed by a network of reference laboratories, research centers and related organizations for monitoring of emerging environmental substances database, include over 109 000 emerging substances and pollutants, which have already been detected in environmental samples, but are not yet monitored. Moreover, even if these contaminants are identified, the concentration dependence of their effect stays unknown in most cases. [8] Recently, multiple programs and strategies, such as REACH [9], [10] and Tox21c [11], were established for better understanding of the biochemical interference and biopersistence of environmental pollutants.

It is clear that the physicochemical properties of the present chemicals are multifarious, thus it is necessary to label, classify and predict their mode of toxic action (MOA) in order to understand their toxicological properties for accurate environmental risk assessment. [12] Veerhar classified organic pollutants based on their physicochemical and structural properties into four classes, which are the (1) baseline chemicals causing narcosis; the (2) more toxic compounds leading to polar narcosis; the (3) reactive compounds with enhanced toxicities; and the (4) specifically acting chemicals leading to receptor mediated toxicity. [8], [13]–[15] As the majority of industrial chemicals were not designed to interfere with biological activities, aside from reactive chemicals, industrial compounds generally lack the structural attributes to initiate specific toxic pathways. This places the majority of industrial compounds into the first two categories of the Veerhar classification scheme. [16]–

[20] Even if these chemicals cannot bind selectively to biological receptors, they are able to interact with biological membranes through weaker and reversible hydrophobic interactions.

[16]–[20]

Firstly Meyer and Overton related the effects of narcosis to the hydrophobic partitioning of compounds, in the lipid theory of narcosis, [21], [22] which was later linked to their octanol-water partition coefficient ( $\log K_{OW}$ ). [18], [23] Substituted hydrocarbons, such as alkanes, alcohols, esters or halogenated benzenes compose mainly the first class of Veerhar's scheme. [13] The MOA of these chemicals is via narcosis, which is the non-specific toxic action on the cell membranes, leading to the reversible disruption of its functions. [16], [24] In the cases of first class chemicals, a linear relationship can be observed between their  $\log K_{OW}$  and toxicity. [13] The polar narcotics in the second Veerhar's class are substituted phenols, anilines, nitrobenzenes, pyridines and amines of which target site is still the cell membrane. At the same time their toxicity is higher compared to narcotics, as they possess numerous hydrogen bond acceptors and donors, which helps in establishing interactions with the phospholipids of the cell membrane. [13], [15] In these cases, instead of  $\log K_{OW}$ , the membrane-water partition coefficient ( $\log K_{mem-bulk}$ ) correlates with the MOA. [13], [25]

Even if narcosis is defined as the perturbation of membrane structure, there is still no precise description of its mechanism. While it is clear, that narcotic chemicals accumulate within biological membranes, the exact cause of toxicity is still undefined. [24] According to Mullins if the volume fraction ( $V/V$ ) of a narcotic compound in the membrane is higher than 0.003, narcosis will occur. [26] Even if by now more complex theories have been developed, the volume fraction theory still remains as a useful tool to understand the membrane affecting phenomena of substances. [27], [28]

For the support of environmental and toxicological sciences,  $\log K_{OW}$ ,  $\log K_{mem-bulk}$  and other properties of less-known, chemically inert industrial compounds can be characterized while their hydrophobic partitioning can be inspected, all by using the modern tools of computational chemistry. [29]–[32]

## **1.1 BIOLOGICAL MEMBRANES**

### **1.1.1 Structure of Biological Membranes**

Biological membranes are semi-permeable structures present in all living organisms. Every living cell use membranes to control the movement of biomolecules, to define its physical boundaries and to defend itself from harmful compounds coming from

environment. Their thickness is around 30-100 Å (3-10 nm). [33], [34] As being the borders of cells, they must have specific characteristics: they must be sturdy and selective but still flexible and permeable enough to communicate and adapt to the conditions of the surrounding environment. [35] The fluid mosaic model (**Figure 1**), proposed by Singer and Nicholson in 1972 [36] was one of the first models regarding the structure of cell membranes. It suggests that the base of a biological membrane is composed of a phospholipid bilayer, which provides the necessary fluidity and elasticity, and within, protein molecules are embedded in the presence of a small amount of carbohydrates and cholesterol.

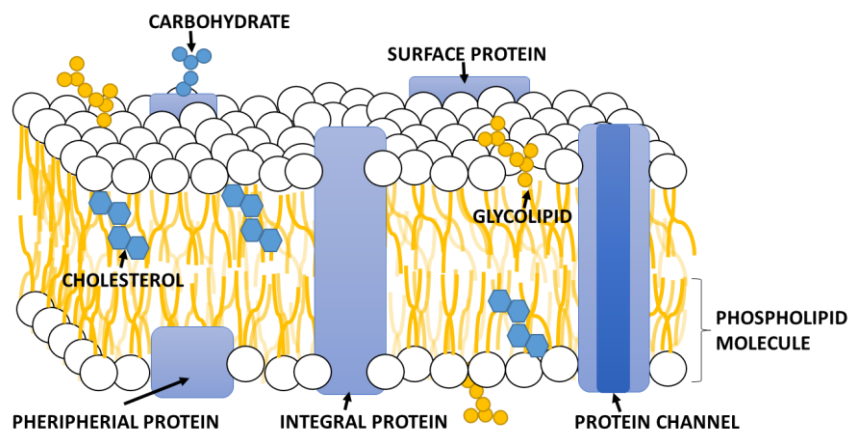


**Figure 1** Singer-Nicholson model of biological membranes

A typical membrane can consist of several hundreds of different types of lipids and proteins. [37] In eukaryotic cells phosphatidylcholine (PC) is the most commonly found headgroup type for phospholipids (~50%), but others, like phosphatidylserine, phosphatidylethanolamine, sphingomyelins and cholesterol can also be found as membrane components. [38], [39] In terms of lipid chains several different types can be observed in cells, which can be characterized by their length, degree of unsaturation and branching. [40], [41]

Even though the variety of membrane lipids is enormous, they possess a critical common structural motif: they are amphipathic molecules, meaning they are built up by hydrophobic fatty acid tails and a hydrophilic headgroup. [42], [43] The balanced interactions of the membrane lipids maintain the conformation of lipid bilayers: weak interactions between lipid tails and water, van der Waals interactions between the tails and strong electrostatic and hydrogen bonding forces between headgroups and water. [28], [42], [44]

For these reasons water and membrane/water interfaces are just as critical to the cellular functions and stability, as lipids. Water influences stability, fluidity and phase behavior of phospholipid membranes, and also has a crucial role in the electric properties of

the bilayer. [45], [46] Both experiments and molecular simulations have shown that water molecules lose their bulk-like nature near membrane surfaces, [47]–[50] as their translational mobility and rotational entropy decrease when their interactions with the lipid headgroups become stronger, [51] which means that different interfacial water regions belong to different membrane compositions. [45], [52] The hydrating water molecules form an ordered, typically 1-2.5 nm thick stable layer (maximum 5 layers of structured water) at the membrane interface [45], where adjacent water molecules are oriented by the headgroups as the dipoles of individual water molecules are aligned counter to the bilayer dipole. [46] These layers are stable enough to present multiple energy barriers to approaching nanoscale objects. [48], [53] Preferred molecular orientations can capture most of the structural features of these interfacial layers and can be used for defining interfacial sublayers. The orientation of molecules relative to a macroscopic membrane/water interface can be analyzed in terms of their orientation statistics. [54]–[56]

As phospholipids being major component of the membrane, there are many experimental methods to quantify their structural and dynamic parameters. [57] X-ray scattering can be used to define the electron density profiles (EDP) of bilayers to gain insight into the inner structure and thickness ( $D_{HH}$ ) of a membrane. [58] Molecular-level structure and dynamics can be studied using nuclear magnetic resonance (NMR) with isotopically labeled lipids to investigate headgroup and chain orientation with respect to the bilayer normal, and to define the deuterium order parameter ( $S_{CD}$ ) for lipids with fully deuterated acyl chains. [59], [60] This parameter provides general information on lipid chain order, fluidity and phase changes. NMR can also be used to investigate the dynamic motions in bilayers using  $^{13}\text{C}$  [61] and  $^{31}\text{P}$  isotopes. [62] Vibrational sum frequency generation (VSFG) [63] and Raman microscopy [64] can be used to probe bilayer surfaces. Although experimental techniques offer a detailed description of lipid bilayers, many of these require models to interpret results (X-ray, NMR or VSFG measurements). [65], [66]

The molecular dynamics (MD) simulation of lipid bilayers has contributed a great deal to the understanding of the structure and dynamics of lipid bilayers since its inception made in the late 1980s. [66]–[70] By the late 1990s it became possible to simulate bilayers built from hundreds of lipids, for tens of nanoseconds. These extensions enabled the computation of several dynamic properties, [71] which can be directly compared to experimentally available values, such as  $S_{CD}$ . The quality of agreement between simulated and measured carbon-deuterium order parameters since then became a standard metric for the validation of simulations and lipid force fields. [72]–[74] In 2005 Benz et al.

demonstrated that EDPs can be obtained directly from all-atom simulations providing easily comparable results with X-ray scattering data. [75] The growth of the system size enabled the calculation of membrane undulations and area compressibility, which are important elastic properties of biological membranes. [76], [77] The outcome of these results challenged the MD community and developers to create better representation for the interatomic interactions (force fields) and for computational methods that can reproduce experimental data. [72], [78], [79]

### 1.1.2 Passive Transport Phenomena

While several significant membrane transport processes involve special proteins, small uncharged molecules, such as water, oxygen or urea, can permeate the cell membrane without any regulatory mechanism in an acceptable rate, via passive diffusion. While this basal permeation has a great importance in establishing osmotic balance, it can also lead to the penetration of narcotics which can promote the loss of cell functions. [31], [80]–[82]

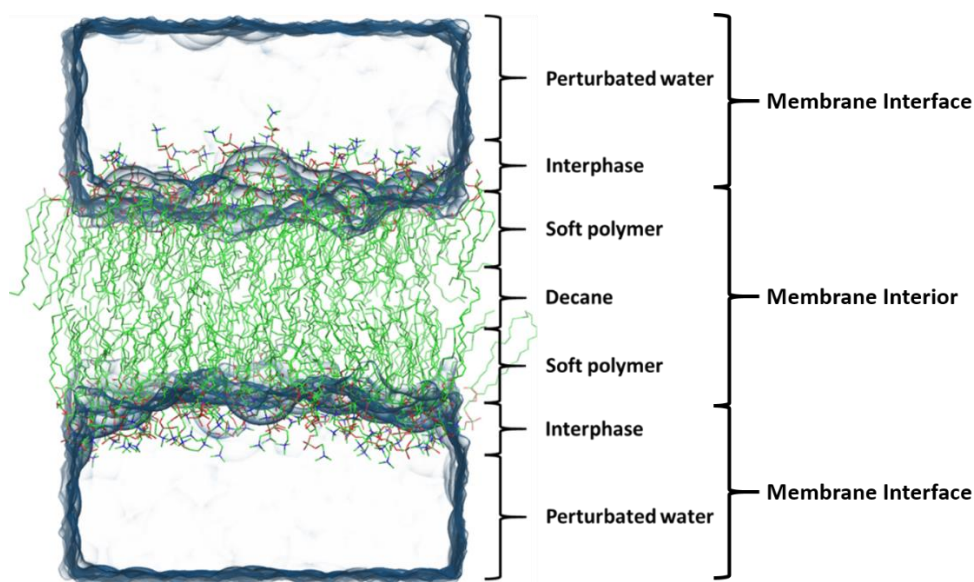


**Figure 2** Inhomogeneous solubility-diffusion model of lipid bilayers

A key property of the passive transport of an investigated substance is its partitioning between water and membrane phases which is affected by the kinetics and thermodynamics of the specific permeation process. [57], [83], [84] Nowadays membrane permeation is conceptualized by the ‘inhomogeneous solubility-diffusion model’ (**Figure 2**), which divides the lipid bilayer into four distinctive regions in a single leaflet: low headgroup density (Perturbed water phase), high headgroup density (Interphase), high tail density (Soft polymer phase) and low tail density regions (Decane phase). Each region has different properties, thus different resistance to the permeants, while all are separated by rough interfaces especially at the water/membrane interface. [81]–[83], [85], [86]

In this model [67], [85] the first two regions belong to the interface of the membrane, while the latter two describe the membrane interior. The perturbed water region is dominated by the interactions of the water molecules, where their behavior can be described as bulk water, and has the least effect on the permeation processes. In the interphase the water molecules are bound to the atoms of the lipid headgroups, and therefore their diffusion is coupled. As a result, this region presents a large barrier for most molecules.

In the membrane interior, starting from the high viscosity soft polymer region, a negligible amount of water molecules is present. This means that the last remaining hydrogen bonds with water molecules needs to be broken up and solely short-range electrostatic interactions can be established with the present carbonyl groups. Due to the high density of lipid tails the membrane behavior is fluid-like and it has high viscosity and minimal free volume. This region is considered as the main resistance to the permeation of water and additional small molecules. In the central region the lipid density drops, the tails are more disordered and large “free volume pockets” are present, compared to the previous regions. [67], [85]

Small molecule membrane interactions can be classified as adsorption and permeation across the membrane. During adsorption the molecule interacts with the membrane at the water-lipid interface and the molecule changes its state from being solvated to being reversibly bound to the membrane surface. In contrast, membrane permeation is a process, when the molecules from the solvated phase move through the lipophilic (hydrophobic) core to the other side of the membrane. [87] The penetration of molecules through biomembranes also plays essential role in drug intake [87], [88], therefore empirical guidelines have been set up in the field of pharmaceutical research. ‘Lipinski’s rule of five’ is used to evaluate the druglikeness of a chemical species. Aside from specifying the criteria of a drug-like molecule, it also describes the major determinants of passive permeability, which are lipophilicity, polarity, but mainly size and the hydrogen bond donor properties. [89]–[92] From this aspect, most drugs and environmental pollutants share similarities regarding their ability to act as permeants thus the rule could also be applied in this field.

### **1.1.3 Modeling Membrane Systems**

Due to the high complexity of biomembranes, they are most commonly studied by using model membranes, which compose of the most relevant lipids found in the membrane of interest. Reducing the complexity of the investigated system not only helps in carrying out the simulations, but also gives opportunity to systematically investigate the effects of different factors separately, such as pH, temperature or pressure, for the small molecule-

membrane interactions. By simplifying the investigated systems it also helps in a more direct comparison of the penetration and binding abilities of compounds with varying properties. [83], [87]

For modeling mammalian plasma membranes the most commonly used lipids are neutral phospholipids, such as 1,2-dipalmitoyl-sn-glycero-3-phosphatidylcholine (DPPC, shown in **Figure 3**) which is one of the most abundant species. [93]

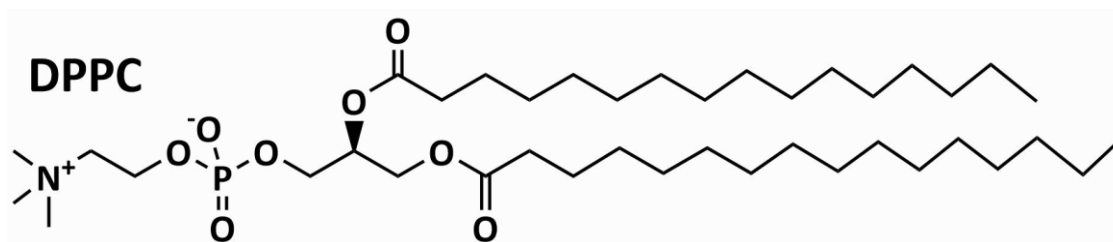


Figure 3 2D structure of a DPPC molecule

Besides the building blocks of the model membranes, its thermophysical state is also important since. Bilayers can be found in nature in a variety of phases such as subgel ( $L_C$ ), gel ( $L_\beta'$ ), rippled ( $P_\beta'$ ) or the liquid crystalline ( $L_\alpha$ , fluid) states. Each phase has different characteristic molecular arrangements which can be described with a set of structural properties, such as area per lipid (APL), membrane thickness or the order parameter of the lipid tails. For understanding small molecule membrane interactions the most relevant state of the membrane is the fluid phase. [87], [94], [95]

Phase transitions represent a structural rearrangement of the bilayer. Phase transitions can be induced by the changes in environmental factors, such as temperature and pressure, hydration or pH. [87], [94], [95] At the same time the interaction of narcotics and small molecules with membranes can also induce the phase transition of membranes, shift the fluid-to-gel transition temperature and broaden the temperature range of the phase transition. [28], [87] As the balanced interactions of the phospholipids are disturbed by the adsorption of compounds on the membrane-water interface the attractions between the phospholipid tails become more dominant and interdigitation of lipid tails may occur, and a monolayer might form. [96], [97] The disruption of water molecules around the bilayer and the penetration of additional molecules can change the membrane properties, such as fluidity, which can also disturb the functioning of lipids and proteins. [28], [87]

#### 1.1.4 Biological Membranes and Small Molecule Interactions Inspected by Molecular Dynamics Simulations

Molecular Dynamics (MD) is a powerful tool to describe and understand the time evolution of a computational model of a complex chemical (biochemical) system. In the case

of classical MD simulations the interatomic interactions are described by force fields – which are mathematical expressions describing the dependence of the systems’ potential energy on the atomic positions –, and atomic motions with the Newtonian equations of motion. [98] MD enables a thorough view of structure and dynamics of the simulated system and can provide relevant details which would be either inaccessible or expensive and time consuming via current experiments. [99] In the case of biological membranes several studies have been carried out recently with the help of MD to describe the structure and understand the phase transitions of membrane models of different lipid compositions [100], [101]; the self-assembly of bilayers [102], [103]; the effect of ions [104]; interactions with proteins [105], [106]; the permeation of small molecules. [84], [107]–[110]

While the structural changes of such processes can be understood via the analysis of general membrane parameters [111], [112], the energetic properties of the interactions remain hidden. The partitioning and preferred position of a molecule interacting with the membrane – like in the case of membrane penetration – can be determined by a free energy profile along the bilayer normal, under controlled condition (e.g. temperature and pressure), where the change in the free energy provides a clear view whether a penetration process is thermodynamically and kinetically favorable or not. [113], [114] To obtain the free energy profile of such process classical MD simulations may not be well suited, as high free energy barriers restrict the detailed sampling of the entire configuration space as the system is likely to be found trapped in local free energy minima. Thus enhanced sampling algorithms were developed which bias the system towards high energy regions which would be hard to access otherwise [107], [115] such as umbrella sampling [116], adaptive biasing [117], thermodynamic integration [118], metadynamics [119], [120] and its improved version, well-tempered metadynamics. [121]

While permeability coefficients are experimentally accessible, the mechanism of penetration is not observable, as the local membrane-solute interactions are difficult to probe and also the kinetics of the process stays unknown. [31], [82] In contrast, modern molecular dynamics (MD) simulations provide a detailed view of both the interactions and the kinetics of the process. By now molecular simulations have been successfully used to describe the general mechanism of passive transport across membranes in atomic resolution. [31], [32], [84], [122] The key is to obtain the free energy profile along the membrane normal which can provide a quantitative description on the energetics and the structural preferences of the penetrating molecules in the passive transport. [83], [113], [114]

## 1.2 SPECIES FROM THE CLASSICAL CHEMICAL INDUSTRIAL ERA. PASSIVE MEMBRANE PERMEATION OF 1,4-DIOXANE, MORPHOLINE, OXANE AND PHENOL

Aromatic hydrocarbons are present in several classical industrial processes. The family of these molecules is diverse and includes species such as polyaromatic hydrocarbons (PAHs), chlorinated aromatic hydrocarbons, furans and also the less focused nitrogen, sulfur or oxygen containing heterocyclic hydrocarbons (NSO-HETs). [123] The presence of heteroatoms makes these compounds more water soluble and mobile compared to their homocyclic analogues [124], fulfilling ‘Lipinski’s rule of five’, leading to a lasting and easily spreading contamination in industrial sites [125] and also an enhanced risk of contaminated drinking water resources. [126],[123] NSO-HETs have been regarded as emerging contaminants by the European Union’s NORMAN network as of their increasing concern in different areas. [7] Selected PAHs, benzene, toluene, ethylbenzene, xylene and phenols are often monitored in polluted groundwater sites, but other NSO-HETs are frequently not measured, potentially because of the absent data on their human- and ecotoxicological effect for adequate risk assessments. Still the knowledge on their mode of interaction with cells and their way of toxicity is insufficient.

Due the lipophilic nature of NSO-HET the primary site of their toxicity is the cell membrane. [127]–[131] Accumulation of compounds in the membrane may lead to the alteration of the membrane structure and function, [132], [133] which can lead to the penetration of additional molecules. [134]–[136] At the same time several NSO-HETs are suspected or proven to be embryotoxic [137] or carcinogenic [123], [124], [138], which means that they must be able to permeate into the cell interior to inflict these effects.

**Table 1** Properties of the investigated cyclic compounds: 1,4-dioxane, oxane, morpholine and phenol. All data were obtained from [139] if not indicated else. The abbreviations are the following: M is molecular mass, S is solubility, logK<sub>OW</sub> is the octanol-water partition coefficient,  $\mu$  is the electric dipole moment,  $\rho$  is the density and N<sub>donors</sub> and N<sub>acceptors</sub> are the hydrogen bond donors and acceptors, respectively.

Name	Molecular formula	M (g/mol)	S (g/l)	log K <sub>ow</sub>	$\mu$ (D)	$\rho$ (g/cm <sup>3</sup> )	N <sub>donors</sub>	N <sub>acceptors</sub>
<b>1,4-dioxane</b>	C <sub>4</sub> H <sub>8</sub> O <sub>2</sub>	88.11	miscible	-0.27	0	1.03	0	2
<b>Oxane</b>	C <sub>5</sub> H <sub>10</sub> O	86.134	80.2	0.95	1.74 [140]	0.88	0	1
<b>Morpholine</b>	C <sub>4</sub> H <sub>9</sub> NO	87.122	miscible	-0.86	1.48 [141]	1.02	1	2
<b>Phenol</b>	C <sub>6</sub> H <sub>5</sub> OH	94.113	82.8	1.46	1.224	1.07	1	1

1,4-dioxane, morpholine, oxane and phenol are industrially applied NSO-HET molecules (**Figure 4**) which are able to passively permeate inside biomembranes, since their properties fulfill Lipinski's rule of five, as collected in **Table 1**. In contrast with their wide usage, their behavior in the vicinity of biomembranes, the kinetics of their penetration and their membrane altering effects are yet to be understood. As homo- and heterocycles are suggested to be able to penetrate inside bilayers and alter their properties, they can be considered as possible narcotics, which can be investigated by using model membranes and molecular dynamics simulations. My goal with this study was to broaden the knowledge on the possible risks these compounds promote on biomembranes, using DPPC composed model membrane systems and molecular dynamics simulations.

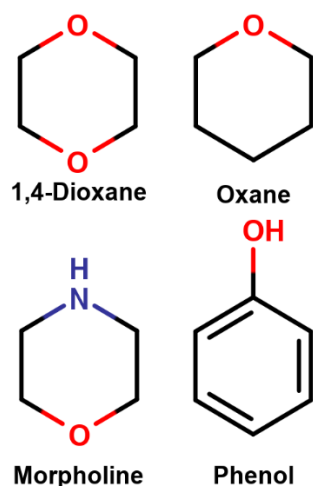


**Figure 4** Schematic figure of the investigated NSO-HETs, 1,4-dioxane, oxane, morpholine and phenol.

Phenol is a widely used chemical and intermediate such as in the production of food additives, energy, fine chemicals or phenolic resins just to name a few. [142], [143] The production of phenol is increasing at a yearly average rate of 1.8% since 2010, but is still unable to meet the consumption needs. Phenol is present in the effluents of various industries with high concentration up to several thousand mg/L and it contaminates the surface and groundwater. [144] The Environmental Protection Agency (EPA) considers phenol as a priority pollutant because of its high toxicity and ability to accumulate in the environment. At the same time the discharge of phenol without treatment is a serious threat to human health as it irritates the human skin, eye and mucous membranes, and severe cases of chronic exposure leads to coma and respiratory arrest. [145]–[148]

Oxane (tetrahydropyran, THP) is a cyclic ether, and a core structure of several biomolecules such as glucose or ribose and is found as an intermediate during the low-

temperature oxidation of alkenes. THP is nowadays tested as a next generation heterocyclic oxygenated fuel [149] widely used in petrochemical and pharmaceutical industries, and for the synthesis of biologically active compounds, thus it is expected that its concentration in the environment will grow in the future. [150]–[155]

1,4-dioxane was used as a stabilizing agent for chlorinated solvents, such as 1,1,1-trichloroethane (TCA) before the restrictions of the Montreal Convention. Nowadays, it is used as an industrial solvent and appears as a side product of industrial processes like the production of organic compounds, disinfectants, cooling liquids and hygienic products. [156], [157] Contamination caused by 1,4-dioxane has been detected in different areas worldwide, from surface- and groundwater to landfills, due to industrial waste and wastewater and illegal dumping. [157]–[159] 1,4-dioxane has several health effects and it is considered as a B2 type ‘Probable human carcinogen’. [157], [160]

Morpholine is a cyclic secondary amine which is used widely in the industry like in pharmacology, as a vulcanization accelerator, as a coating for fruits or as an emulsifier in the food industry. [161]–[163] Morpholine is highly soluble in water and a large amount is released into the environment via industrial effluents which leaks into groundwater and drinking water sources. [164] Only a restricted strains of bacteria is able to degrade and utilize it as a sole source of carbon, nitrogen and energy. [164]–[167] It is severely dangerous to humans as it is irritating to the eyes, skin and mucous membranes. [161], [162] Animal studies have shown that it induces stomach and intestine hemorrhage. [163]

### **1.3 SPECIES FROM THE POTENTIAL FUTURE OF CHEMICAL SYNTHESSES. THE CASE OF THE CO<sub>2</sub> – 1,3-BUTADIENE REACTION**

Carbon dioxide is one of the main contributors to global warming. Its constantly rising levels are a result of anthropogenic emissions, such as transportation, energy or food production. Regulating its emissions and decreasing its atmospheric concentration is an urgent concern of humanity. While on one hand carbon dioxide is a dangerous byproduct of fossil fuel combustion, on the other hand it has excellent properties as an eco-friendly carbon and oxygen source, thus its chemical fixation could be a favored strategy for attenuating its rising levels. As a chemical for synthesis it has several practical advantages, such as abundance, availability, economic efficiency and lack of toxicity. [168]–[173] At the same time it is hard to utilize it in industrial processes as a raw material, because carbon is found in the most oxidized state in CO<sub>2</sub>. As a result reactions of carbon dioxide is chemically highly inert and must be combined with a high-energy reactant to gain a thermodynamic driving force. [168], [174]–[178]

Olefins are widely used as co-reagents since the high energy density of their carbon–carbon double bonds leads to high reactivity.[179] The five most important synthetic polymers - low-density polyethylene, high-density polyethylene, polyvinyl chloride, polystyrene, polypropylene and polyethylene terephthalate - are all made by olefins via C-C bond formations. [180], [181]

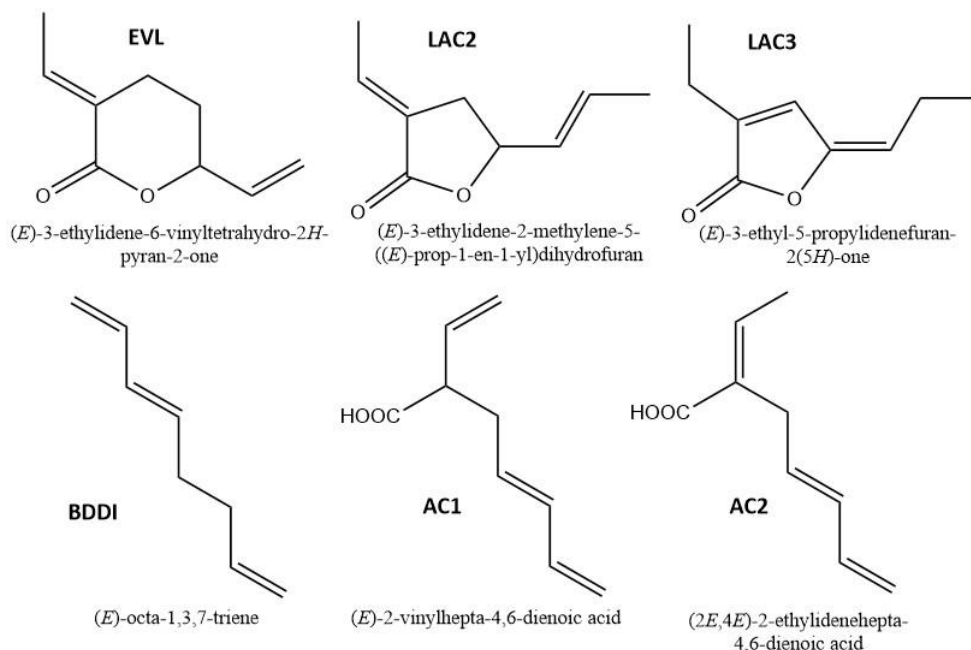


**Figure 5** 2D image of the products of the CO<sub>2</sub>-1,3-butadiene reaction. [179] The simplified names of the molecules indicated next to the structures are used throughout this study.

So far several studies have focused on the catalytic coupling of carbon dioxide with olefins to form useful products. [182]–[186] Out of these reactions, one of the most promising is the telomerisation of CO<sub>2</sub> with 1,3-butadiene. 1,3-butadiene is a component of the C<sub>4</sub> fraction of oil cracking, and widely applied in the rubber industry as a major monomer. [187] Alternatively, 1,3-butadiene can also be derived from succinic acid, which is ranked as one of the top 12 biomass platform compounds best suited to replace petrochemicals. [188], [189] The reaction of CO<sub>2</sub> and 1,3-butadiene results in the synthesis of a highly functionalized  $\delta$ -lactone, 3-ethylidene-6-vinyltetrahydro-2*H*-pyran-2-one (EVL, **Figure 5**). [169], [174], [175], [179], [190], [191] As EVL has both internal and terminal carbon-carbon double bonds, it could be converted into several products of industrial relevance, [175], [192] thus functional polymers made from CO<sub>2</sub> and 1,3-butadiene is a promising technology of great interest. [170] Efforts have been made to improve the conversion rate and selectivity of the reaction for EVL formation. [169], [174], [179], [193], [194] At the same time about a 14% yield of side products appear during the reaction, such as a covalent butadiene dimer (octa-1,3,7-triene, BDDI), acids (2-vinylhepta-4,6-dienoic

acid, AC1 and 2-ethylhepta-4,6-dienoic acid, AC2) and other lactones composed of five membered heterocycles (3-ethylidene-2-methylene-5-(prop-1-en-1-yl)-dihydrofuran, LAC2; 3-ethyl-5-propylidene-furan-2-one, LAC3) (**Figure 5**). [170], [175], [179] Aside from the known reaction of 1,3-butadiene and CO<sub>2</sub>, there is a lack of information in previous studies on the products, either their pure liquid properties or their environmental effects. At the same time, several methods exist to predict the properties of molecules, as shown in **Table 2**. Based on these predicted data, all molecules of the investigated reaction are able to permeate into membrane bilayers based on Lipinski's rule of five.

**Table 2** Pure liquid properties of the products of the CO<sub>2</sub> – 1,3-butadiene reaction. Chemicalize [195] was used for the prediction of water solubility and logK<sub>OW</sub>, and ACD/Labs Percepta Platform – PhysChem Module [196] for the prediction of logK<sub>OW</sub>, density and boiling point. The permanent dipole moment of the molecules was calculated by Gaussian 09 [197], at B3LYP/6-31G(d) [198], [199] level of theory.

Short Name	Molecular formula	Molecular weight (g/mol)	Water solubility (g/l) [195]	log K <sub>OW</sub>	Dipole moment (D)	Density (g/cm <sup>3</sup> ) [196]	Number of hydrogen bond donors	Number of hydrogen bond acceptors
<b>EVL</b>	C <sub>9</sub> H <sub>12</sub> O <sub>2</sub>	152.19	2.044	$\frac{1.601}{2.456}$ [196] [195]	4.452	1.2±0.1	0	2
<b>LAC2</b>	C <sub>9</sub> H <sub>12</sub> O <sub>2</sub>	152.19	1.774	$\frac{1.710}{2.398}$ [196] [195]	4.893	1.2±0.1	0	2
<b>LAC3</b>	C <sub>9</sub> H <sub>12</sub> O <sub>2</sub>	152.19	0.449	$\frac{1.990}{2.554}$ [196] [195]	4.439	1.1±0.1	0	2
<b>BDDI</b>	C <sub>8</sub> H <sub>12</sub>	108.184	0.043	$\frac{3.180}{3.050}$ [196] [195]	0.207	0.7±0.1	0	0
<b>AC1</b>	C <sub>9</sub> H <sub>12</sub> O <sub>2</sub>	152.19	0.542	$\frac{1.960}{2.273}$ [196] [195]	1.348	1.0±0.1	1	2
<b>AC2</b>	C <sub>9</sub> H <sub>12</sub> O <sub>2</sub>	152.19	0.332	$\frac{2.427}{1.972}$ [195]	1.972	no predicted properties	1	2

The goal of this study was to provide a first estimation of the pure liquid properties of the products of the CO<sub>2</sub>-1,3-butadiene reaction by using classical molecular dynamics simulations combined with OPLS-AA force fields. As the interaction of these molecules

with biological membranes is not yet understood, our further goal is to understand the effects of these potential pollutants on biomembrane systems by using MD and WT-MD.

#### **1.4 THE VAPOR-LIQUID EQUILIBRIA AND SUPERCRITICAL PHASE OF 1,3-BUTADIENE**

In the previous section the products of the highly investigated reaction of 1,3-butadiene and CO<sub>2</sub> reaction were introduced. This reaction faces several hardships for setting the proper environment to reach high selectivity rate for the preferred product, EVL. To be able to reduce or eliminate the amount of added solvents, the use of supercritical CO<sub>2</sub> would be beneficial for this reaction. Solvents are often the major (by mass) component in process chemistry, especially in the case of multi-step manufacturing, where the number of reactions additionally contribute to the overall solvent need. [200], [201] They can also promote the desired equilibrium position, adapt the kinetic profile of the reaction and influence the product selectivity. [202]

Physicochemical properties of supercritical fluids (SCFs) such as density, diffusivity, viscosity and dielectric constant can be modified on a large scale by changing the pressure and/or temperature, therefore SCFs can be used broadly as reaction media and their application can also allow selective and faster extraction in separation processes. [203]–[211] These features make SCFs an attractive alternative to liquid solvents, while collecting experimental data from these extreme conditions can be challenging due to the increased hazards and the need of specialized equipment, where a wide range of variables are needed to be investigated. [210]

As an alternative to experimental methods, molecular dynamics simulations can make an efficient tool to study the local structure of not only liquids [212]–[214] gases [212], [215] and the vapor-liquid equilibria (VLE) [216]–[220], but also SCFs. [210], [221] The great advantage of MD is that it can be applied successfully to a wide range of physical conditions if the validity of the force field parameters are carefully checked. [210] The analyses of the results provide molecular level understanding of the solvent behavior in the investigated phases which would be either inaccessible or expensive and time consuming via experiments. [99], [210]

In my work an important raw material for the synthesis of different polymers, cycloalkanes and –alkenes, 1,3-butadiene is investigated structurally and thermochemically from the VLE to the supercritical phase by means of classical molecular dynamics simulations. The critical properties of the molecular system have been obtained through four different methods, based on density, potential energy, surface tension and specific surface

area, which have been compared and evaluated. This work also proposes a method to distinguish liquid, vapor and ‘phase transferring’ molecules in the VLE.

As accurate models for supercritical CO<sub>2</sub> are already published [222]–[224], the simulation of the binary mixture of 1,3-butadiene and CO<sub>2</sub> under supercritical conditions is only one step away, which may help to promote a possibly more environmentally friendly alternative for this reaction.

## **1.5 MOTIVATION OF THIS THESIS**

Due to this day, several xenobiotics are emitted into the environment without proper handling and understanding the dangers they can pose to biological entities. The motivation of my work was to better understand the pollution mechanism of potential environmental pollutants on biological membranes, and to promote the development of greener technologies by using molecular dynamics simulations. Even if using the means of MD for these problems is still in the early stage, understanding molecular processes can be of great help to broaden the knowledge on pollution pathways, classify chemicals based on their membrane altering effects and to help in setting up environmental risk assessments. At the same time modern computational methods also provide atomistic level of understanding of hardly accessible chemical states. By using these information, chemical processes can be optimized for higher selectivity or lower solvent usage, in order to reduce the amount of unwanted side products and prevent the production of further environmental pollutants.

## 2 METHODS

### 2.1 MOLECULAR DYNAMICS SIMULATIONS

Molecular simulations based on detailed atomistic models and realistic microscopic interactions represent a powerful tool to gain insight into the structure and dynamics of complex molecular systems and to understand the microscopic origin of a given phenomena. [225], [226] Simulations are frequently used supporting experimental studies to help interpret results and to further guide the research. [227], [228] Just to mention a few examples of the advances of MD, in 2013 1 ms ( $10^6$  ns) of simulation have been carried out to understand the folding mechanism of ubiquitin in the presence of explicit solvent molecules. [229] By 2015 an enveloped influenza virion in explicit solvent was also examined on a microsecond timescale. [230] In 2017 Shibuta et al. have managed to simulate over  $10^9$  atoms for 2 ns to further understand the solidification of pure metal. [231] In 2021 the whole SARS-CoV-2 virion was modelled by Nguyen et al.. [232]

#### 2.1.1 Parameterization and Calculation of the Potential Energy

Force fields (FF) are mathematical expressions and the corresponding parameters describing the dependence of the systems' potential energy on the coordinates of its particles. The mathematical expressions are chosen in such a way that they can provide an accurate description of the potential energy surface and the number of parameters are minimal and as universal as possible. FF parameters can be obtained from fitting to results of high level *ab initio* or semi-empirical quantum mechanical calculations or using experimental data from neutron, X-ray or electron diffraction, NMR, infrared, Raman or neutron spectroscopy. [78], [225], [233] Although the potential energy ( $E_{pot}$ ) can be constructed in several ways, the summation of the intra- and intermolecular interactions affecting each atom was expressed by the following formula in this work:

$$E_{pot} = E_{str} + E_{angles} + E_{torsion} + E_{vdW} + E_{ele} \quad Eq. 1$$

, where the first four terms refer to intramolecular contributions to the total energy ( $E_{str}$ : bond stretching,  $E_{angles}$ : angle bending and  $E_{torsion}$ : dihedral), and the last two terms refer to the van der Waals ( $E_{vdW}$ ) and Coulombic ( $E_{ele}$ ) interactions (**Figure 6**).

In the following sections the general form of the intra- and intermolecular terms will be shown, as included in the CHARMM36 [72] force field.

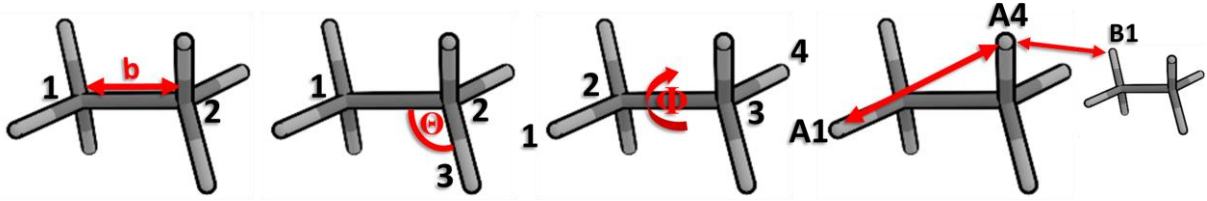


**Figure 6** Schematic figure of the potential energy terms: stretching, bending, torsion and intermolecular interactions

### 2.1.1.1 Intramolecular energy terms

Intramolecular interactions represent a set of bonded interactions within a molecule from 1,2 to 1,4 interactions (**Figure 6**). Bond stretching is usually represented with a harmonic function:

$$E_{str} = \sum_{bonds} k_b (b - b_0)^2 \quad Eq. 2$$

, where  $k_b$  is a force constant representing the strength of the bond,  $b$  is the actual distance between two covalently connected atoms and  $b_0$  is the equilibrium distance between them. While harmonic constants are computationally cheap to calculate, additionally their usage prevents the breaking of bonds, making classical MD simulations unsuitable for modeling chemical reactions. [225]

Angle bending is also assumed to be a harmonic potential:

$$E_{angle} = \sum_{angles} k_\theta (\theta - \theta_0)^2 \quad Eq. 3$$

, where  $k_\theta$  is a force constant specific for the angle ( $\theta$ ) between two covalent bonds with a common atom with an equilibrium value of  $\theta_0$ .

For molecules building up from more than 3 atoms in a row a torsional or dihedral term needs to be included to be able to reproduce conformational changes. Torsional energy is usually represented by a Fourier cosine series expression:

$$E_{torsion} = \sum_{torsions} k_\phi [1 + \cos(n\Phi - \delta)] \quad Eq. 4$$

, where  $\Phi$  is the torsional angle,  $\delta$  is the phase of the dihedral term,  $n$  represents the multiplicity, and  $k_\phi$  defines the force constant.

### 2.1.1.2 Representation of non-covalent interactions

Non-bonded interactions describe connections between atoms within a molecule, or between atoms of different molecules. These generally comprise van der Waals and electrostatic interactions. Non-bonded interactions within a molecule are accounted if the

atoms are separated by at least four bonds. Due to small distances potential energy could become strongly repulsive or attractive, so interactions between 1,2 or 1,3 pairs are considered to be already described by the intramolecular terms. In the case of 1,4 interactions some force fields introduce a scaling factor or exclude it from the calculations as a non-bonded interaction, as the size of the repulsive and attractive Lennard-Jones terms would make the simulation unstable. [226]

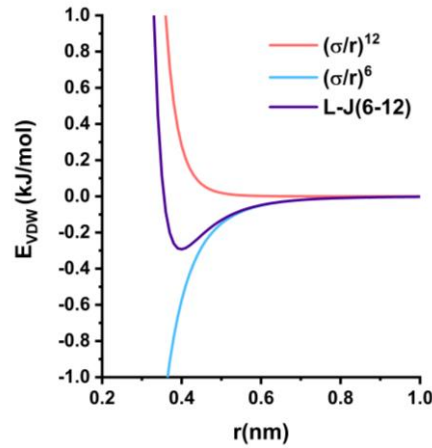


**Figure 7** Lennard-Jones pair potential of two carbon atoms from the CGenFF force field showing the repulsion and attractive components of the function

Repulsive and attractive dispersive interactions at short distances are most commonly treated with 12-6 Lennard-Jones (LJ) terms:

$$E_{vdw} = \sum_{\substack{i \neq k \\ \text{for nonbonded}}} 4\pi\epsilon_{ik} \left( \left( \frac{\sigma_{ik}}{r_{ik}} \right)^{12} - \left( \frac{\sigma_{ik}}{r_{ik}} \right)^6 \right) \quad \text{Eq. 5}$$

, where  $r_{ik}$  is the distance between non-bonded particle  $i$  and  $k$ ,  $\sigma_{ik}$  is the distance at which the particle-particle potential energy is zero and  $\epsilon_{ik}$  is the depth of the potential well. In the equation the first part resembles to the repulsion due to the overlap of the electron clouds and the second part to the attractive component of the interaction (**Figure 7**). In the case of heteroatomic interactions  $\epsilon_{ik}$  and  $\sigma_{ik}$  are often treated with the empirical Lorentz-Berthelot combining rule:

$$\epsilon_{ik} = \sqrt{\epsilon_{ii} \cdot \epsilon_{kk}} \quad \text{Eq. 6}$$

$$\sigma_{ik} = \frac{\sigma_{ii} + \sigma_{kk}}{2} \quad \text{Eq. 7}$$

Electrostatic interactions are most often included by using the Coulombic term:

$$E_{ele} = \sum_{\substack{i \neq k \\ \text{for nonbonded}}} \frac{q_i q_k}{4\pi\epsilon_D r_{ik}} \quad \text{Eq. 8}$$

, where  $q_i$  and  $q_k$  are static point charges located at the non-bonded atomic nuclei or at charged non-atomic interaction sites (e.g. in the case of additional dummy atoms of water models) which are  $r_{ik}$  distance from each other and  $\epsilon_D$  is the dielectric constant which equals as one in simulations using explicit solvent. Though electron density distribution can be obtained with high accuracy from quantum-mechanical methods, it is not trivial to reduce it to point charges used in MD. [226] Also, as electrostatic interactions are the longest-ranged interaction types, they require a special treatment throughout force evaluation such as Ewald summation [234] [235], which will be discussed later.

Basically, the potential energy surface is defined by the connectivity of the atoms in molecules presented in the system of interest and a corresponding set of geometrical ( $b_0$ ,  $\theta_0$ ,  $\Phi$ ,  $\delta$ ,  $n$ ,  $\psi_0$ ,  $\sigma_{ii}$ ), charge ( $q_i$ ) parameters as well as force constants ( $k_0$ ,  $k_\Phi$ ,  $k_\psi$ ) and an energy value ( $\epsilon_{ii}$ ). Most of the cases, the different force fields (e.g. CHARMM, OPLS-AA) mean different parameter values.

### 2.1.1.3 Water Models

Since aqueous environment is generally presented in systems of interest and water itself has special physicochemical features, distinguished attention is taken for its appropriate representation in MD simulations. The most accurate method is using its explicit representation, in the expense of further increasing the size of the simulated systems. [233] Other types of solvent representations are also available, like implicit solvent models [236], [237] or coarse-grained methods [238], [239] to gain speed in expense of accuracy. Regardless the selection of the water model, it must be compatible with the force field representation of the non-water species for the appropriate treatment of the solute-solute, solvent-solute, solvent-solvent interactions [240]. Explicit solvent models can be classified by the number of interaction sites (**Figure 8**), by being rigid or flexible, and polarizable.

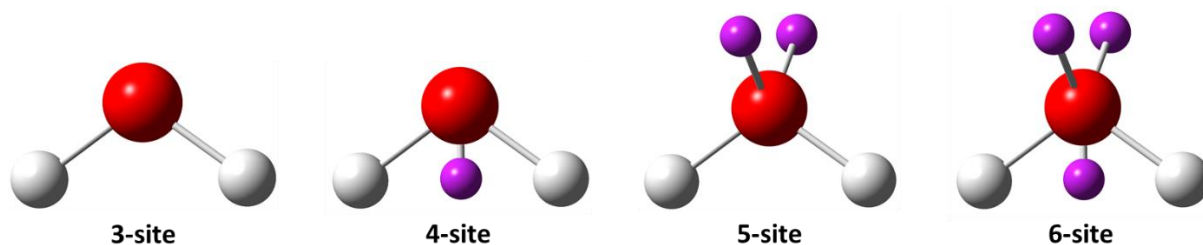


**Figure 8** General arrangement of 3-6 interaction-site containing water models

The classical TIP3P water model involves 3 interaction sites with a rigid body, and applies also Lennard-Jones parameters on the H atoms, to earn higher accuracy and avoid instabilities during simulations. [235] Multiple-site models apply dummy atoms as

interaction sites to the original structure of a water molecule to improve electrostatic behavior. [241], [242]

#### 2.1.1.4 Periodic Boundary Conditions (PBC)

To obtain results without unwanted surface or boundary effects, the system must be bounded without physical walls. This is realized by employing periodic boundary conditions (PBC) that mimics the presence of a bulk by surrounding the simulation box with an infinite number of its identical copies (**Figure 9**). [227]

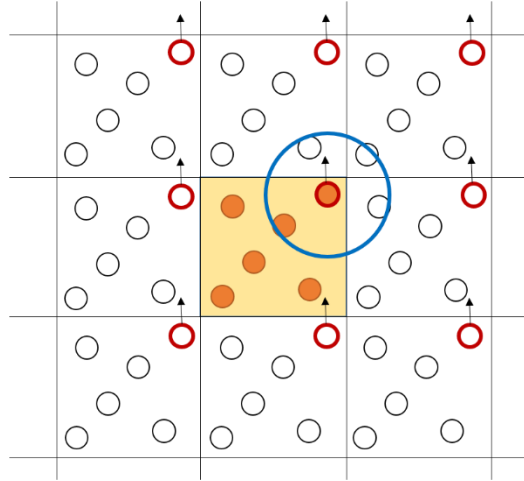


**Figure 9** 2D visualization of the PBC including the cut-off range [243]

During the simulation an image particle copies the movement of the original one in the central box. As a molecule exits the box an image particle will move in to replace it on the opposite side, so the number of particles in the central box is conserved. [226] In the case of intermolecular interactions PBC would result in to calculate the LJ terms between all periodic images. By the usage of cut-off values ( $r_{\text{cut-off}}$ ) intermolecular interactions are ignored outside the radius of  $r_{\text{cut-off}}$ , significantly reducing the computational time. It is a reasonable approximation in the case of LJ interactions, which decay rapidly with distance, or if the distribution of the system is homogenous beyond  $r_{\text{cut-off}}$ . [226]

#### 2.1.1.5 Electrostatic interactions under PBC condition

When PBC is applied in the force field calculations the total electrostatic interaction due to all pairs of charges can be given by:

$$E_{ele,total} = \frac{1}{2} \sum_n \sum_{i=1}^N \sum_{k=1}^N \frac{q_i q_k}{4\pi\epsilon_D (r_{ik} + nL)} \quad Eq. 9$$

, where the length of a cubic cell is  $L$ , and it has to be taken into account for every  $i$  and  $k$  pairs of charges. The factor of  $\frac{1}{2}$  is introduced in order to cancel the double counting. This infinite sum (due to PBC) not only converges very slowly, but the result also depends on the

summation order. [226] The most accurate but computationally most expensive method to handle the charges is the Ewald summation. [244] In this method the electric potential field generated by the charges are considered as charge clouds around the particles, which are described by Gaussian distributions. The Gaussians are split up into two parts with opposite sign one for the calculation of long-ranged interactions ( $E^L$ ), the other for the short ranged ( $E^S$ ) ones. As the Gaussian charge clouds also interact formally with themselves ( $E^{\text{self}}$ ), it must be subtracted from the formula.

The Smooth Particle Mesh Ewald (SPME) [234] method improves the Ewald summation with a more efficient computation method. The calculation of SPME is based an approximation of the charge clouds by a gridded distribution, where charges are attributed by mesh points. This leads to a discretized charge distribution which can be solved more efficiently, but with less accuracy. SPME is widely used and implemented in most popular MD simulation packages. [245], [246]

### 2.1.2 Algorithms of Molecular Dynamics Simulations

In order to sample the relevant part of the configurational space of the system of interest, MD simulations generate a trajectory. A trajectory is an ordered list of the atomic coordinates and velocities for each simulation time step for the total simulation time including the time evolution of the potential energy of the system. [227] The trajectory (**Figure 10**) then can be obtained by the numerical integration of Newton's second law, which states that the force ( $F_i$ ) acting on a particle, which has a mass of ( $m_i$ ) results in its acceleration ( $a_i$ ). The acceleration is the second time derivative of the particle's position ( $x_i$ ), and the force acting on the particle is obtained by its interactions with the other particles, and is derived from the gradient of the potential energy of the system. As ergodicity is assumed over the simulation, the results should be insensitive to the initial configuration, but it should allow the system to relax to an equilibrium structure under the planned simulation time. [247]. Initial velocities are assigned to atoms randomly using a Maxwellian distribution on the desired temperature [226]. As each particle interacts simultaneously with all others in the system, the motions of all particles are coupled. Therefore, numerical integration is needed to solve this problem which is earned with the use of finite-difference methods, in which the integration over the time interval is broken into a series of short time steps ( $\delta t$ ). In each time step the forces ( $F_i$ ) experienced by atoms in their current position ( $x_i(t)$ ) are computed. It is then assumed that the force remains constant during  $\delta t$ , so that it can be combined with known dynamic information (position, velocity etc.) to predict new positions and dynamic properties in the next time step, ( $t + \delta t$ ).

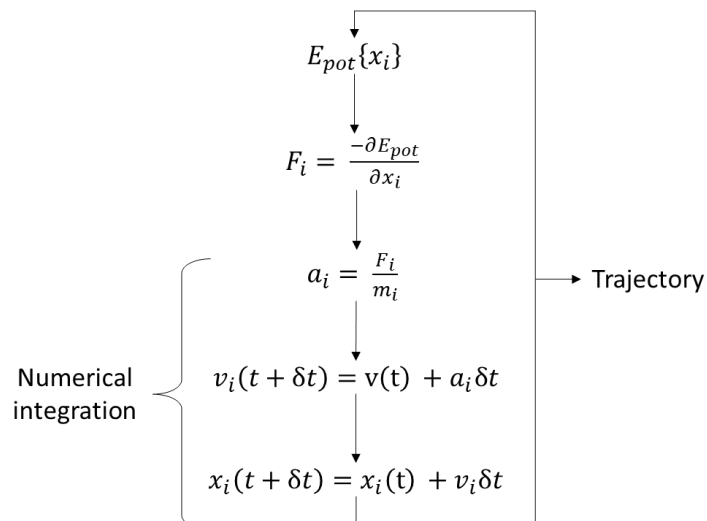


**Figure 10** The basic algorithm of MD [233] Abbreviations:  $E_{pot}$ : Potential energy;  $t$ : simulation time;  $\delta t$ : iteration time;  $x_i$ : atom coordinate for each spatial coordinate of the atoms;  $F_i$ : force component;  $a_i$ : acceleration;  $m_i$ : atomic mass;  $v_i$ : velocity

The most widely used finite-difference methods in MD are based on the Verlet algorithm, which are computationally inexpensive, accurate and stable, able to conserve energy, simple and numerically stable. [227] In Velocity Verlet algorithm [248] (**Figure 11**) the current positions ( $x_t$ , velocities ( $v_t$ ) and accelerations ( $a_t$ ) of the particles are used to estimate their new positions ( $x_{t+\delta t}$ ) (Panel A). Then velocity and acceleration are used to estimate the mid-step velocities ( $v_{t+\frac{1}{2}\delta t}$ ) (Panel B). From the new positions acceleration ( $a_{t+\delta t}$ ) is derived (Panel C), which is then used to evaluate velocity ( $v_{t+\delta t}$ ) (Panel D). As both velocity and position is available, energy can be calculated.

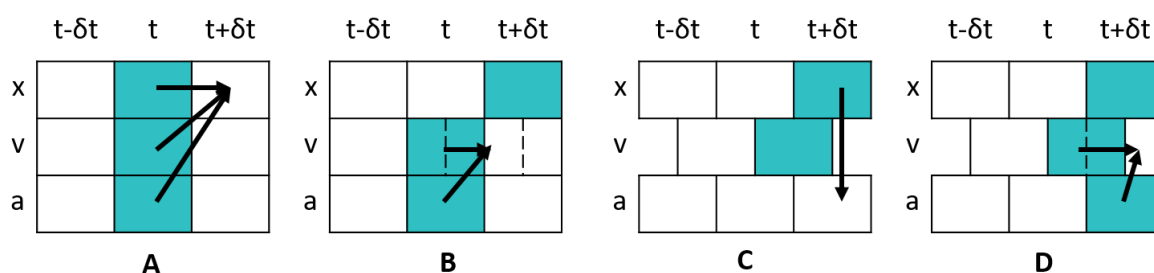


**Figure 11** Illustration of the Velocity Verlet algorithm

The purpose of simulations is not only to observe the motions of particles, but also molecules, which are composed of a certain amount of specific atoms. In the case of molecules atoms are treated as individual bodies that experience different forces coming from inter- and intramolecular interactions. The time step used in the integration of the equation of motion should be shorter by a factor of 10 than the period of the highest vibrational frequency to avoid improper structures from atomic collisions. [226] As intramolecular motions are high frequency vibrations these set the upper limit of the time

step to be around 1 fs. Removing the fastest degrees of freedom and constraining high frequency changes, allows to increase the time step of MD simulations. Thus bonds and angles are often constrained, especially in the case of X-H bonds, and small molecules can even be treated as single rigid units, where their movement is tracked by their center of mass. [226], [227]. Nowadays iterative schemes are used to satisfy the constraints at the end of each time step. The scheme for the Leapfrog Verlet algorithm is called SHAKE [249], and for the Velocity Verlet algorithm, RATTLE [250].

During simulations to set the proper environment thousands of solvent molecules can be necessary. Keeping water molecules rigid during simulations can significantly speed up simulations. The analytical method SETTLE [251] combines SHAKE and RATTLE for water molecules in order to be able to calculate positions and velocities to satisfy holonomic constraints. P-LINCS (parallel linear constraint solver) [252] allows constraining of all bonds in a macromolecule and enable parallel communication between computer nodes during the calculation of constrained molecules, enabling high speed and stability.

### 2.1.3 Molecular Simulation of Different Ensembles

Microcanonical (NVE) ensemble simulations are performed with a constant number of particles (N), in a fixed volume (V), where the total energy (E) of the system can be obtained from the sum of the kinetic energies ( $E_{kin}$ ) of the particles and the total potential energy of this isolated system ( $E_{pot}$ ). Though the internal energy of the system is constant, it is continuously redistributed between its particles. In order to gain thermophysical properties, it is necessary to perform a simulation either at constant temperature (T) or pressure (P). This can be obtained using ‘thermostats’ and ‘barostats’, respectively, which are modifying standard NVE simulations.

A canonical ensemble represents n copies of a closed system, in which the volume (V), temperature (T) and the number of particles (N) is set, is called an NVT ensemble. All copies of the system are being arranged in an external isothermal heat bath while staying in thermal contact. The energy of the particles of the ensemble may fluctuate. [226] As the velocity distribution of the particles is set by using Maxwell-Boltzmann distribution, one of the simplest ways to adjust temperature, is velocity scaling. [225] Berendsen thermostat [253] does not involve a full velocity scaling at each time step, but employs a time scale ( $\tau_T$ ) to do so. This enables fast calculation, but will not generate a canonical distribution of configurations as does not involve interactions with an external heat bath. [226] This connection can be set with more complex methods, like the Andersen, the Gauss or the Nosé-Hoover thermostats.

The Nosé-Hoover thermostat [254], [255] is a deterministic approach to generate canonical distribution by introducing an extra degree of freedom ( $s$ ), which represents the thermal heat reservoir. The external heat bath is dynamic, has a momentum and an effective mass, which extends the energy term.

$$E = E_{kin} - E_{pot} + E_{kin,s} - E_{pot,s} \quad Eq. 10$$

This approach is called an extended ensemble method and it scales the movement of the particles to adjust the temperature to the required value.

In an isothermal-isobaric system (NPT ensemble) not only the temperature, but also the pressure (P) of the simulation box is kept constant, while the number of molecules stay the same. A macroscopic system reacts to an imposed pressure by changing its volume, so these simulations involve the fluctuations of the simulation box. [226] The simplest approach is the Berendsen barostat [253], which involves a scaling factor to the volume with a  $\tau_p$  time scale.

For dynamic coupling of the system to a barostat Andersen introduced an extended ensemble barostat approach [256] with an equation of motion for the system volume, to allow dynamic volume exchange of the system with its surroundings. With coupling the system to an external volume it responds with either isotropic expansion or compression. Parrinello and Rahman [257] extended Andersen's approach to enable the control of pressure and stress. With this the simulation box is also allowed to change its shape, as the shape of the cell is described by a cell matrix. This way a new potential and kinetic energy term is introduced and associated with the change of the box size and shape.

## 2.1.4 General Protocol for Classical MD Simulations

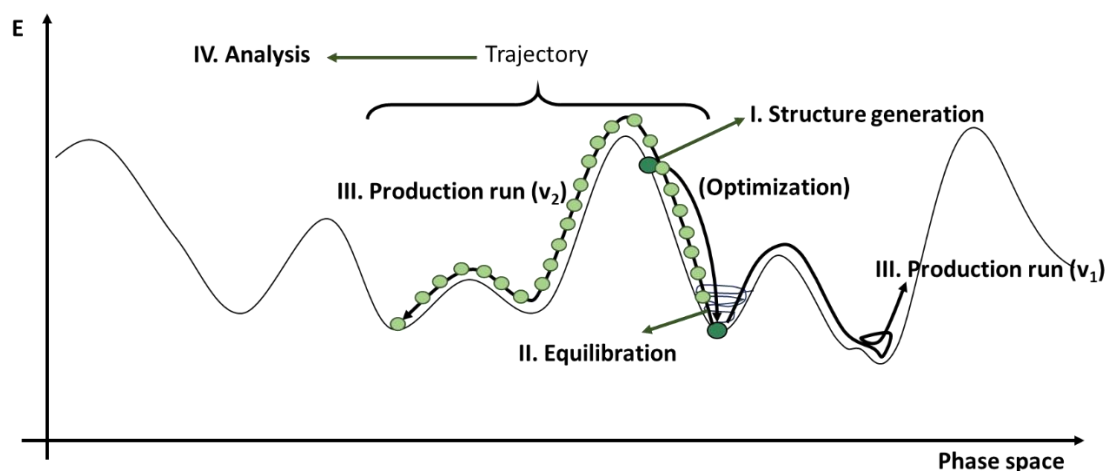


**Figure 12** Steps of a Molecular Dynamics simulation

A general MD simulation consists of four stages: structure generation and optimization, equilibration, production run and analysis (**Figure 12**). During the structure generation the simulation box is filled up with molecules. In the next step, a short geometry optimization of the system is required, where by changing the configuration the system gets closer to a local minimum and more plausible configuration of the system. As the first step of the equilibration, initial velocities are assigned to the particles and the simulation box evolves to be able to respond the phase behavior at the given temperature and pressure during equilibration. By the end of the equilibration an average value of the computed parameters should be reached. The production run must be executed for a longer time range than the relaxation time of the examined process and the obtained time dependent atomic positions, velocities, forces has been stored for the detailed analysis. The desired physico-chemical and other time-independent properties can be accessed by averaging of the trajectories over sufficient simulation time. [225]

## 2.2 FREE ENERGY CALCULATIONS

### 2.2.1 Concepts of thermodynamic free energy

Free energy is one of the basic concepts of thermodynamics. [42], [258] Free energy comes from the first-law of thermodynamics: it is the available energy to perform thermodynamic work at constant temperature and its sign indicates whether a process is thermodynamically favorable or not. There are two types of free energy. The Gibbs free energy ( $G$ ), which is the maximum amount of work a system can do at a constant pressure and temperature, and Helmholtz free energy ( $A$ ), which is the maximum amount of work a system can do at constant volume and temperature, ergo in the canonical ensemble.

Gibbs free energy can be calculated as  $G = H - TS$ , where  $T$  is the absolute temperature,  $S$  is the entropy and  $H$  is the enthalpy, which is the function of internal energy ( $U$ ), pressure ( $P$ ) and volume ( $V$ ):  $H = U + PV$ . Helmholtz free energy ( $A$ ) can be calculated as  $A = U - TS$ . Thus change in  $A$  can be described as:

$$\Delta A = \Delta U - T\Delta S \quad \text{Eq. 11}$$

while change in  $G$  is:

$$\Delta G = \Delta U - T\Delta S + P\Delta V \quad \text{Eq. 12}$$

To connect macroscopic properties to statistical mechanics the molecular partition function can be used, with which the free energy of a system in a canonical ensemble and at constant temperature and pressure can be given by the formulas:

$$A = -k_B T \ln Q_{NVT} \quad \text{Eq. 13}$$

$$G = -k_B T \ln Q_{NPT} \quad \text{Eq. 14}$$

where  $k_B$  is the Boltzmann constant,  $T$  is the temperature and  $Q$  is the partition function of the system. The partition function ( $Q$ ) for a system at thermodynamic equilibrium at NVT and NPT ensembles can be expressed as:

$$Q_{NVT} = \frac{1}{h^{3N} N!} \int \int e^{-\frac{H(p,r)}{k_B T}} dp dr \quad \text{Eq. 15}$$

$$Q_{NPT} = \frac{1}{h^{3N} N! V_0} \int \int \int e^{-\frac{H(V,p,r)+PV}{k_B T}} dV dp dr \quad \text{Eq. 16}$$

where  $N$  is the number of particles,  $h$  is Planck's constant,  $V$  is the volume and  $V_0$  is a basic unit of volume chosen to make  $Q_{NPT}$  dimensionless. The integral is performed over all 3N positions ( $r$ ) and momenta ( $p$ ) of the particles. [259] In the case of NPT ensembles volume also has to be taken into account as it determines the size of the system. The Hamiltonians ( $H(p,r)$ ) and ( $H(V,p,r)$ ) gives the total energy of the system in a given conformation. [259]–[261] As molecular dynamics simulations are carried out in an NPT ensemble throughout this dissertation, free energy denotes Gibbs free energy, if not indicated else.

### 2.2.2 Free energy difference of states

To transform a molecular system from one thermodynamic state to another, free energy is needed. To estimate the difference in free energy ( $\Delta G_{BA}$ ) between configurations  $A$  and  $B$  of the same system, one has to estimate the ratio of partition functions between them. [98], [260]

$$\Delta G_{BA} = G_B - G_A = -k_B T \ln \frac{Q_{NPT,B}}{Q_{NPT,A}} \quad \text{Eq. 17}$$

The configurations belonging to  $G_A$  and  $G_B$  are called the end states or initial and final states of the simulations. End states define the beginning and ending of free energy calculations. These can be distinguished from each other by the way their particles are arranged and interact with each other. [260] The ratio of full partition functions can be reduced to configurational partition functions by using momentum integrations, as according to the equipartition theorem the kinetic energy is constant at constant temperature. The configurational partition functions ( $Z_A$  and  $Z_B$ ) solely depend on the potential energy of the system. [261]

$$\begin{aligned}\Delta G_{BA} &= -k_B T \ln \frac{Z_{NPT,B}}{Z_{NPT,A}} \\ &= -k_B T \ln \frac{\int e^{-\frac{U_B(V,r)+PV}{k_B T}} dV dr}{\int e^{-\frac{U_A(V,r)+PV}{k_B T}} dV dr}\end{aligned}\quad Eq. 18$$

In an NPT ensemble obtained from a molecular dynamics simulation, each configuration obeys to a given probability density ( $\rho(V,r)$ ), depending on the potential energy of a given molecular arrangement.

$$\rho(V,r) = \frac{e^{-\frac{U(V,r)}{k_B T}}}{\int e^{-\frac{U(V,r)}{k_B T}} dV dr}\quad Eq. 19$$

Configurations obeying to this probability density are called Boltzmann distributed. From a Boltzmann distribution the average of a particular observable ( $C(V,r)$ ) can be defined as:

$$\langle C \rangle = \int C(V,r) \rho(V,r) dV dr\quad Eq. 20$$

To calculate such an ensemble average from a simulation, a method is needed, which can generate configurations with a probability density of  $\rho(V,r)$ .

During an MD simulation the ensemble average of an observable  $C(r)$  is obtained by averaging over all the generated configurations. In this case it is assumed that the ensemble average ( $\bar{C}$ ) is equal to the time average ( $\langle C \rangle$ ).

$$\bar{C} = \langle C \rangle\quad Eq. 21$$

**Eq. 21** is called the ergodic hypothesis. While most systems cannot be proven to have ergodic behavior, if all configurations with a relevant probabilities have been visited, the ergodic hypothesis holds up as a first estimation. If high probability regions are separated by remarkable energy barriers, it becomes unlikely, that all significant configurations have been sampled. This is called the problem of quasi-nonergodicity. [260]

If one well defined chemical, mechanical or thermodynamic process needs to be analyzed, it can frequently be represented by a set of low dimensional, generalized coordinates. These coordinates are usually called reaction coordinates or collective variables (CV), and the latter is used throughout this work. A CV is a function of the atomic coordinates that is capable of describing the physics behind the process under investigation. By using a CV the probability density function of a process can be obtained along the coordinates of interest. [261] This CV can be a torsional angle for a conformation change process [119], or a set of coordinates for a distance related energy, like in the case of membrane penetration, or ligand binding [84], where a set of coordinates is defined where a particle/or particles move along during the simulation. [120] As CVs are a function of atomic coordinates they can be indicated as  $CV(s(V,r))$ , but for simplification, in this work CV(s) is used.

By applying the theory of thermodynamic cycle to obtain the thermodynamic free energy, the total free energy difference between the end states of a process can be calculated by the sum of free energy difference between intermediate steps. [113] To determine the total free energy difference of two predefined end states of a simulation a series of intermediate structures has to be defined leading from one state to the other. While these intermediate steps might be artificial and unphysical, together they form a thermodynamic cycle. By the end of the simulation, from the probability distribution of the molecules in the end states, the free energy of the process can be directly obtained. [113], [259]

In simulations sampling can be done two ways: *biased* or *unbiased*. Unbiased sampling is a casual MD simulation, where the evolution of the CV is inspected without modifying its occurrence. In unbiased MD simulations the average kinetic energy per degree of freedom is only about  $k_B T/2$  (which is about 1.2 kJ/mol at 298 K), which means that it takes a lot of simulation time to cross a large energy barrier. In enhanced sampling/biased sampling methods a bias potential is added to the CV which enhances the probability of visiting relevant configurations during the evolution of the simulation by decreasing the free energy differences between the end states by enabling higher transition rates and better sampling of rare events. Enhanced sampling methods are generally based on some assumptions on the underlying system, such as the choice of meaningful collective variables or the definition of the end states. [262]

### **2.2.3 Estimation of free energy**

Once the appropriate set of configurations have been sampled, the free energy difference of states needs to be estimated. [263] The probability density distribution of the

CV at state A and state B ( $\rho(CV(s)_A)$  and  $\rho(CV(s)_B)$  respectively) can be calculated from the ratio of partition function of states A and B:

$$\frac{\rho(CV(s)_B)}{\rho(CV(s)_A)} = \frac{Q_{NPT,B}}{Q_{NPT,A}} \quad \text{Eq. 22}$$

Therefore, the free energy difference between states A and B can be obtained as the ratio of the probability of the different states:

$$\Delta G_{BA} = -k_B T \ln \frac{\rho(CV(s)_B)}{\rho(CV(s)_A)}. \quad \text{Eq. 23}$$

As the free energy is directly related to the probability of the states along a chosen collective variable ( $CV(s)$ ), the free energy landscape the process ( $G(s)$ ) can be directly obtained from the probability density distribution of the configurations along ( $\rho(s)$ ) [119]:

$$G(s) = -k_B T \ln \langle \rho(s) \rangle \quad \text{Eq. 24}$$

A simplified free energy landscape can be seen on **Figure 13**. Here, a stable state (A) and a metastable state (B) are shown, which has higher free energy thus it is less populated in an equilibrium configuration. Between these states, an intermediate region (where the peak belongs to a non-reactive transition state) is located, with high free energy and a very small probability. The free energy difference ( $\Delta G^\ddagger$ ) of the free energy of the stable state and the transition state called the free energy barrier. [98], [262]

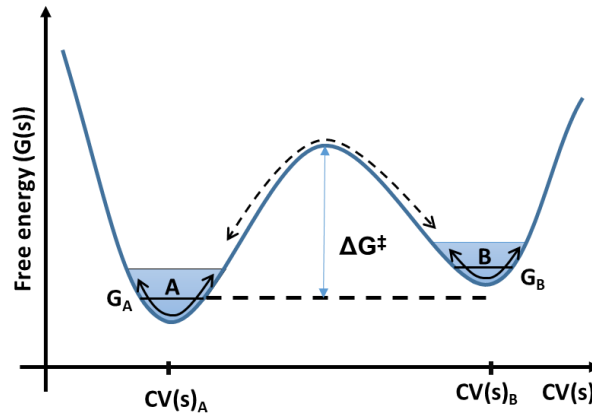


**Figure 13** A model double-well free energy landscape. A stable and a metastable state (A and B respectively) are indicated. The colored regions show where the system fluctuates because of its thermal energy.  $G_A$  and  $G_B$  indicate the free energy levels between which  $\Delta G^\ddagger$  indicates the height of the free energy barrier.

## 2.2.4 Applied methods for free energy calculations

### 2.2.4.1 Free energy perturbation (FEP)

The general perturbation formula describes the difference of A and B systems, whose Hamiltonians are related through small perturbation ( $H_B = H_A + \Delta H_{AB}$ ), and  $\Delta G_{AB}$  can be calculated using **Eq. 25**. [259] The original free energy perturbation (FEP) formula relates

the free energy difference of an initial (state  $\lambda=0$  or state A) and a final (state  $\lambda=1$  or state B) state as an average obtained from their energy difference, obtained by sampling the initial state.

$$\Delta G_{AB} = -k_B T \ln \left\langle e^{\frac{-(E_B - E_A)}{k_B T}} \right\rangle_A \quad Eq. 25$$

Generally, state A and B indicate different molecules, media or molecular arrangements. The thermodynamic cycle can be used to investigate the free energy change for the conversion from one state to the other. [259], [264]

#### 2.2.4.1.1 Molecular Dynamics based FEP calculation

Using MD for FEP calculations enables the treatment of a large ensemble of molecules, the direct representation of solutes, solute-solvent and solvent-solvent interactions. For the simulation to be able to sample all the important regions of the phase space the total free energy change needs to be calculated as a number of intermediate changes using  $n$  windows (**Figure 14**).

$$\Delta G_{total} = \sum_{i=1}^n \Delta G_{i,i+1} \quad Eq. 26$$

This can be achieved by if the Hamiltonian of the intermediate states is related to  $H_A$  and  $H_B$  via a coupling parameter,  $\lambda$ , which can take any value between 1 and 0.

$$H = \lambda H_A + (1 - \lambda) H_B \quad Eq. 27$$

Over the simulation windows, the coupling parameter scales all interaction parameters of the force-field, such as Coulombic and Lennard-Jones parameters. [259], [264]

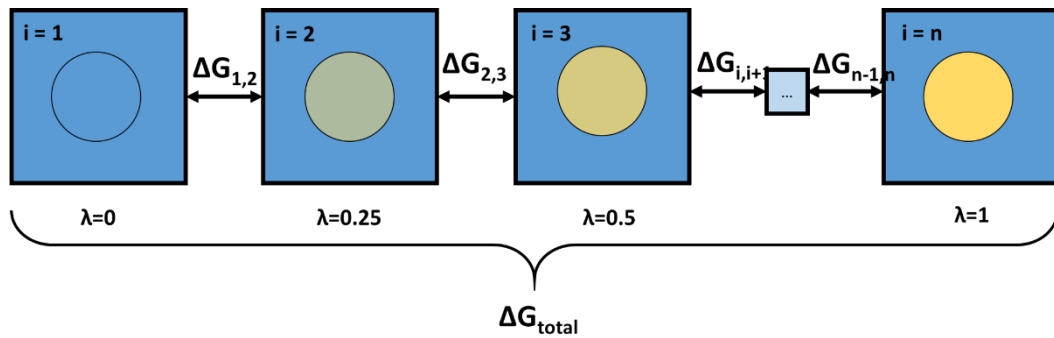


**Figure 14** Schematic figure of FEP calculations using molecular dynamics simulations

#### 2.2.4.1.2 Free energy of hydration from ab initio calculations

By definition, the free energy of hydration, which indicates the free energy needed to transfer a solute from the gas phase to the condensed phase, can be calculated, as:

$$\Delta G_{hyd} = G_{aq} - G_{gas} + RT \ln \left( \frac{RT}{P} \right) \quad Eq. 28$$

Where  $\Delta G_{hyd}$  is the free energy of hydration,  $G_{gas}$  is the free energy in the gas phase and  $G_{aq}$  is the free energy in the solvent phase, while the final term is a correction term, due to the different standard state in the gas and solvent phases. The schematic figure of the calculations is shown on **Figure 15**.

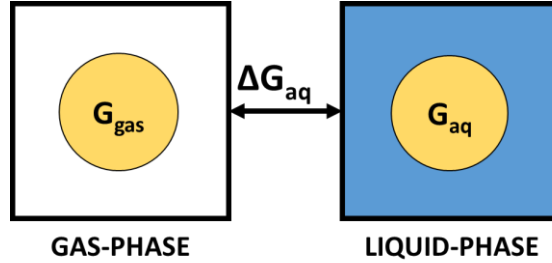


**Figure 15** Schematic figure of obtaining solvation free energy from ab initio simulations

In the gas phase molecular structure with its electron density and the potential energy can be obtained by using ab initio calculations, from which  $G_{gas}$  can be obtained. In ab initio calculations the solvent phase can be represented by continuum solvent models, such as the SMD implicit model. [265] In this representation the solute is present at an atomic level of detail in an electrostatic cavity, surrounded by a dielectric medium representing the solvent. The interactions between the molecule, the cavity and the medium is calculated by using high accuracy atomistic calculations to obtain  $G_{hyd}$ . By the end of the calculations a correction term needs to be applied in order to convert the gas-phase standard state (defined by T and P) to the solution-phase standard state, which is defined as a 1 M solution. [266]

#### 2.2.4.2 Free energy of permeation

The low transition rate between two states of a free energy surface can lead to insufficient sampling of the collective variable. As the barrier height affects the transition rate of a process gravely, by modifying its height the increment in the observed events can be achieved. For this cause an additional potential, a biasing potential ( $P(s(V,r))$ ) can be added to the potential energy ( $U(V,r)$ ), which acts only along CV(s). This results that the explored conformations are distributed according to a biased canonical distribution:

$$\rho'(V,r) = e^{-\frac{U(V,r)+P(s(V,r))}{k_B T}} \quad Eq. 29$$

From this, the free-energy landscape will lead to a  $\tilde{G}(s)$  amount of free energy along CV(s), which is related in the following way with the ‘quasi original’ one, where C and C’ are arbitrary constants:

$$\tilde{G}(s) = P(s) + G(s) + C' - C \quad Eq. 30$$

From this the ‘quasi original’ free energy ( $\tilde{G}(s)$ ) landscape on CV(s) can be recovered by subtracting the bias potential from the obtained value of  $\tilde{G}(s)$ :

$$P(s) = -\tilde{G}(s) \quad \text{Eq. 31}$$

In this case the simulation explores the following distribution:

$$\rho'(V, r) \propto e^{-\frac{G(s)+P(s)}{k_B T}} = e^{-\frac{G(s)-\tilde{G}(s)}{k_B T}} \quad \text{Eq. 32}$$

As the simulation evolves, this distribution gets more and more flat (flat histogram method) as the barriers vanish, and the values of  $s$  become equally likely, the simulation becomes more accurate. [98]

#### 2.2.4.2.1 Metadynamics

Metadynamics [120] is a biasing technique, where a history-dependent bias potential ( $P(s, t)$ ) is used for the collective variable (CV(s)), which itself is a function of the positions of the particles throughout the simulation time ( $t$ ). This bias potential appears during the simulations as a repulsive Gaussian, centered on the explored points of a CV(s) space, leading the system towards previously not explored configurations. These Gaussians can be called ‘hills’ and have a preassigned width ( $\sigma$ ) and height ( $\omega$ ) and are deposited at every  $t'$  time step as the simulation proceeds, where the collective variable has a value of  $s(t')$ . Then the bias potential at time  $t$  can be calculated the following way:

$$P(s, t) = \sum_{t'=1}^{t/t'} \omega e^{-\frac{(s-s(t'))^2}{2\sigma^2}} \quad \text{Eq. 33}$$

On **Figure 16** the process of metadynamics is shown. [98], [120] By adding the Gaussians the system is discouraged of the exploration of already visited states of the CV space, and their sum provides an immediate estimate of the free-energy surface. After a suitable filling time the bias will start growing parallel to itself, and  $G(s)$  can be directly obtained from  $-P(s)$ , for an additional arbitrary constant (**Equation 35 and 36**) [98], [119], [120].

While metadynamics is a widely used method for free energy simulations, it has two known problems: its estimation of free energy landscape does not converge to an exact value, but fluctuates around it. The other problem is that, as it is a flat histogram method it tries to sample the whole CV space, which can lead to the exploration of “nonphysical” states with extremely high free energy and/or nonrelevant configurations.

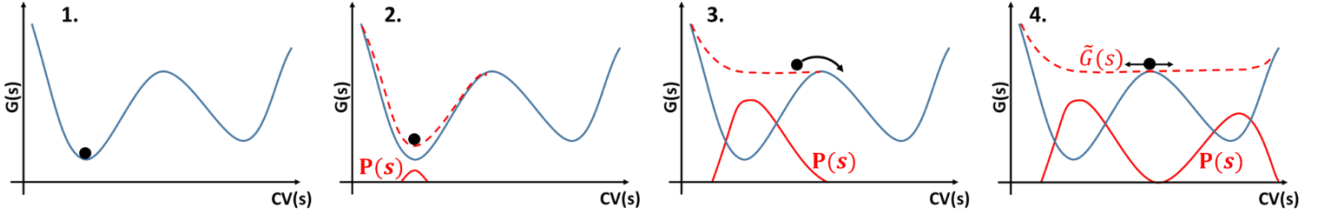


**Figure 16** The process of metadynamics. First the system evolves according to normal dynamics. Then a Gaussian potential ( $P(s)$ ) is deposited, which lifts the system and modifies the free energy landscape in order for the dynamics to evolve and explore new configurations. After the sum of  $P(s)$  fills up the first free energy basin the system is able to move to the second. After the second basin is filled up the system reaches a flat landscape ( $\tilde{G}(s)$ ). The summation of the deposited bias provides the estimate of the free energy profile ( $G(s)$ ).

#### 2.2.4.2.2 Well-Tempered Metadynamics (WT-MD)

In well-tempered metadynamics the height of Gaussians are rescaled ( $\omega_{t'}$ ) as the system passes previously explored configurations of the CV(s) space which enables the free energy profile to converge to an exact value. [115], [121], [267]  $\omega_{t'}$  is rescaled by the following equation:

$$\omega_{t'} = \omega_0 e^{-\frac{P(s,t')}{k_B \Delta T}} \quad \text{Eq. 34}$$

where  $\Delta T$  is a parameter in units of temperature and  $k_B$  is the Boltzmann constant. This means that after the initial filling of the profile, along the CV(s) different height Gaussians are deposited. This implies that the sum of  $P(s) + G(s)$  will no longer be flat, and the bias potential on a long time limit will converge to:

$$P(s, t \rightarrow \infty) = -\frac{\Delta T}{\Delta T + T} (G(s) - C) \quad \text{Eq. 35}$$

where  $C$  is an arbitrary constant and  $\frac{\Delta T}{\Delta T + T}$  is the bias factor in which  $T$  is the simulation temperature. This indicates that the bias does not become the negative of the free energy anymore, but the bias, scaled by the bias factor. As a consequence, the CV(s) is explored at an effective temperature ( $T + \Delta T$ ). If  $\Delta T \rightarrow \infty$ , standard metadynamics is reached, and when  $\Delta T = 0$ , unbiased sampling happens. Finally the free energy can be estimated as:

$$G(s) = -\frac{T + \Delta T}{\Delta T} P(s, t \rightarrow \infty) - C \quad \text{Eq. 36}$$

#### 2.2.4.2.3 Free energy profiles from classical molecular dynamics

A computationally inexpensive approach for calculating the free energy of penetration is to retrieve it from classical molecular dynamics simulations, as there is a one-to-one relation between free energies and density profiles. [268], [269] If the activity

coefficient is independent of the density, the free energy can be obtained by using the following equation:

$$G(s) = -RT \ln \frac{\rho(s_z)}{\rho(s_0)} \quad \text{Eq. 37}$$

where  $\rho(s_0)$  belongs to the bulk phase density and  $\rho(s_z)$  is the mass density at position  $Z$  along the membrane normal.

## 2.3 TWO-PHASE MOLECULAR DYNAMICS (2 $\phi$ MD) SIMULATIONS

Coexisting liquid and vapor phases in the vapor-liquid equilibria (VLE) [216]–[220] and the supercritical phase [210], [221] can be investigated by performing two-phase (2 $\phi$ ) simulations, where the resulting bimodal distribution of the mass density can be used to obtain critical parameters. [217], [218], [270], [271] Several methods exist to directly simulate the VLE, such as Gibbs Ensemble Monte Carlo (GEMC) [272]–[274], the NPT plus test particle method [275]–[277] or the two-phase Molecular Dynamics. [217], [218], [270], [271], [278]

In two-phase Molecular Dynamics (2 $\phi$ MD) the VLE is simulated in an NVT ensemble, where the liquid and vapor phases are in the same simulation box separated by an interface. The great advantage of 2 $\phi$ MD is that the time evolution of the phases and the interface is observable throughout the VLE to the supercritical phase. At the same time the challenging part of 2 $\phi$ MD arises from the presence of the interface which makes selecting the distinct phases complicated, especially near the critical point. Several techniques have been proposed to define the coexisting phases, such as fitting a hyperbolic tangent function [279], [280] or using inverse histograms [281], Monte Carlo sampling [218] or Voronoi tessellation. [217], [270], [271]

### 2.3.1 Voronoi tessellation (VT) based density calculation

Voronoi Tessellation (VT) [243], [282] is a procedure where a subvolume (‘Voronoi cell’) is assigned to an associated point (e.g. defined by the Cartesian coordinate of atoms) which is geometrically closer to that point than to any other. If the atomic volumes belonging to each molecule are summed, the molecular volumes composing the system are obtained. Thus, a set of molecular volumes, the mean molecular volume and the variance of molecular volumes can also be obtained, which can be directly converted to density distribution of the simulated systems. [217], [270], [271]

### 2.3.2 Phase Determination

To obtain a self-consistent method, two-phased simulations are complemented with one phase (1 $\phi$ ) simulations in both liquid and vapor phase at the investigated temperatures

to ensure that the correct values for the density are obtained, thus removing all arbitrary choices in phase definition. Gas phase simulations can be run in the NVT ensemble with same settings as the general slab simulations, while NPT ensemble can be used for liquid simulations. The initial configurations of the 1 $\phi$  simulations can be selected from the final configurations of the slab simulations. From the one-phase simulations general parameters, such as density or Voronoi-volumes can be used for comparison with the two-phased simulations. [217], [270], [271]

In my work [271], the method proposed by Fern et al. [217], [270] was slightly modified to be able to select liquid and vapor phase, and ‘phase transferring’ molecules. In this method Voronoi polygons are created for the center of mass (COM) of each molecule. The distance of the COM and Voronoi vertex  $i$  ( $r_i$ ) is calculated for each vertex in the simulation box. In the case of liquid phase molecules higher sphericity and smaller  $r_i$  values are expected, while vapor phase molecules tend to have larger, irregular polygons with low sphericity. ‘Phase transferring’ molecules can be found at the interface, thus their Voronoi polygons are expected to have irregular shapes also, while on one of their sides they have to have similar properties to the molecules in the liquid phase.

To identify the phase that a molecule belongs to, the maximum value of  $r_i$ , noted as  $r_{max,liq}$ , can be calculated from the 1 $\phi$ MD liquid phase simulations. According to my initial proposition, each liquid phase molecule has to fit into a sphere with a radius equal to  $r_{max,liq}$ , while vapor phase and phase transferring molecules cannot meet this requirement. In 2 $\phi$ MD simulations each Voronoi cell has a  $k$  amount of Voronoi vertices which are closer or in equal distance to the COM of the corresponding molecules than  $r_{max,liq}$ . Taking the two extremes, the molecule is surely in liquid phase if  $k/i = 1$ , while in vapor phase if  $k/i = 0$ , where  $i$  is the total amount of Voronoi vertices belonging to a Voronoi cell. Considering instantaneous structural disturbances, wider interval for  $k/i$  ratio is required for the proper sorting, therefore an empirical interval parameter,  $\alpha$ , has been introduced and its value is chosen to be 0.1. The effect of  $\alpha$  are shown on **Figure 17**. So, if  $k/i < \alpha$ , a molecule is considered as gas phase; while if  $k/i > 1-\alpha$  it is a liquid phase; and if  $\alpha \leq k/i \leq 1-\alpha$  it is a ‘phase transferring’ molecule.

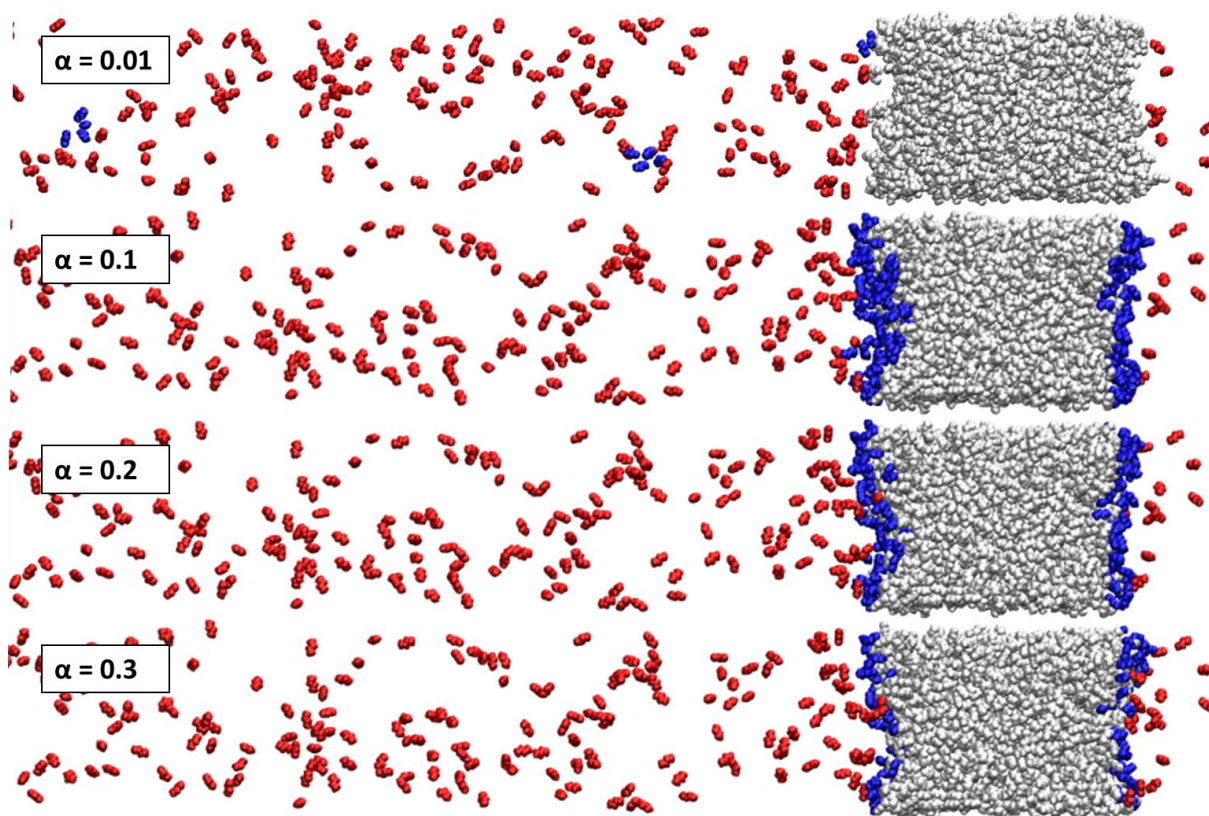


**Figure 17** The effect of  $\alpha$  on the selection of molecules

## 2.4 ANALYSIS OF MEMBRANE PARAMETERS

### 2.4.1 Membrane Structural Parameters

Membrane structural parameters obtained from MD simulations provide primary information on the bilayer structure, which is also directly comparable with experimental information. [60], [283] Such structural parameters are area per lipid (APL), volume per lipid (VPL), electron density profiles (EDP), membrane thickness ( $D_{HH}$ ), deuterium order parameter ( $S_{CD}$ ) and the compressibility modulus ( $K_A$ ). A summary of the formulas of the parameters is shown in **Table 3**.

Mass density profiles (MDP) show the partial densities of predefined atom groups across the simulation box along the Z axis. Electron density profiles are calculated by defining the number of electrons for each present atoms in the system. It can also be measured experimentally using X-ray scattering thus the accuracy of membrane simulations can be checked. From EDPs membrane thickness can be obtained by investigating the peak-to-peak distance on the diagram but it also involves the direct hydrate shell of the membrane. [58], [78]

**Table 3** Definitions and formulas of the general membrane structural parameters

Membrane parameter	Definition	Formula	Abbreviation
APL	Area per lipid [284]	$\frac{2 \times L_x \times L_y}{n_{lipid}}$	$L$ : average x and y dimensions of the simulation box
VPL	Volume per lipid [284]	$\frac{V_{box} - n_{water}V_{water} - n_{comp}V_{comp}}{n_{lipid}}$ $\frac{APL \times D_{HH}}{2}$	$V_{box}$ : average volume of the simulation box $V_{water}$ : the volume of a TIP3P water molecule (0.03053 nm <sup>3</sup> ) [78] $V_{comp}$ : derived from the density of neat compound $D_{HH}$ : membrane thickness
$K_A$	Isothermal compressibility modulus, a dynamic parameter to measure stress resistance of the membrane [285]	$\frac{2k_B T \langle APL \rangle}{n_{lipid} \sigma_{APL}^2}$	$k_b$ : Boltzmann's constant $T$ : temperature $\sigma_{APL}^2$ : the variance of APL
$S_{CD}$	Deuterium order parameter, which measures the orientation of C-H bonds with respect to the bilayer normal [78]	$\frac{1}{2} \langle 3 \cos^2 \theta - 1 \rangle$	$\theta$ : the angle between bilayer normal (Z) and the vector between C <sub>i</sub> -H <sub>i</sub>

For a planar bilayer the area per lipid (APL) can be obtained as the average lateral dimensions of the simulation box ( $L_x$  and  $L_y$ ) divided by the number of lipids found in one membrane leaflet, but in this case the APL distribution remains unknown. Besides the conventional APL calculation, the average APL can also be obtained *via* a Voronoi tessellation (VT) based technique for simple and multicomponent lipid bilayers [286], [287] as well as complex protein-membrane [288], [289] systems. The great advantage of VT technique is that it also provides not only APL distribution beyond the average but also local structural information of the bilayer surface. [289] For instance, local disturbances caused by the direct permeation of small molecules can be identified by VT-based APL distribution. [286], [290], [291] To find such local disturbances, the trajectories can be analyzed by a self-wrote VT-based Python script (powered by Python 2.7 [292] and MDAnalysis 0.18.1 [293]), in which the phosphorous atoms are projected to the macroscopic  $XY$  surface of the membrane [294], while the periodic boundary conditions are also taken into account. The

area belonging to each phospholipid molecule can be calculated as the area of a Voronoi polygon by using Delaunay triangulation. [295]

VPL can be obtained either as the product of the APL and the thickness of a single bilayer ( $D_{HH}/2$ ), or by removing the total volume of water (and additional) molecules from the average volume of the simulation box. Both methods were tried, and the difference between their results is scarce. Deuterium order parameter defines the ordering of the lipid acyl chains by measuring the relative orientation of the C-H (experimentally C-D) bonds along the acyl chains with respect to the bilayer normal, Z. [78], [284]

$$S_{CD} = \left| \frac{1}{2} \langle 3\cos^2\Theta - 1 \rangle \right| \quad Eq. 43$$

where  $\Theta$  is the angle between bilayer normal (Z) and the vector between  $C_i-H_i$ , and  $\langle \rangle$  represents the ensemble average. The compressibility modulus provides information on the membrane resistance against the effects of surface changes/environmental stress. [283], [296]

#### 2.4.2 Orientation of Molecules in the Membrane Vicinity

To be able to describe the orientational preference of water and additional molecules in the membrane/water interface Cartesian coordinates are bound to each molecule then vectors are defined bound to each investigated species. Three local vectors can be defined to describe the orientation of water molecules (upper panel of **Figure 18**): the dipole vector ( $z$ ), the vector joining the two hydrogen atoms (H-H vector,  $y$ ) and the normal vector ( $x$ ) of the  $zy$  plane, in order to obtain their relative orientation to the membrane surface normal (Z). Their orientation is characterized by their angles denoted  $\alpha$ ,  $\beta$  and  $\gamma$  respectively, formed with the interface normal.

Out of all the investigated permeants only 1,4-dioxane have been analyzed with such detail. In this case, two vectors are needed, and the corresponding angles ( $\alpha$ ,  $\beta$  in the bottom panel of **Figure 18**). Here the vector joining the two oxygen atoms (O-O vector,  $z$ ), and the normal of this vector ( $x$ ). It should be noted that due to the symmetry of the molecules the molecular normal, and H-H vectors (in the case of water molecules) can be directed in two opposite directions, and there is no physical way to distinguish them. Therefore, their corresponding angles ( $\beta$  and  $\gamma$ ) can only be scattered between  $0^\circ$  and  $90^\circ$ , and thus their cosines between 0 and 1, while  $\alpha$  angles defined by the dipole moment vector of water or O-O vector of dioxane (as a direction is defined by selecting the O-O vector) can fall into the entire angular range of  $0^\circ$  to  $180^\circ$ , and cosine range of -1 and 1. To make interpretation easy for their ensemble averages, uniformly distributed orientation belongs to value 0, which is

the case for the expected value ( $\langle \rangle$ ), of  $\cos(\alpha)$ , while  $\cos(\beta)$  and  $\cos(\gamma)$  must be shifted downwards by 0.5. To characterize the variations of the average orientation of water and dioxane molecules along the interface normal axis,  $Z$  can be divided into 1 Å slices (0.1 nm), where  $\Phi_\alpha(Z)$ ,  $\Phi_\beta(Z)$  and  $\Phi_\gamma(Z)$  – orientational function – profiles have been calculated, defined as:

$$\Phi_\alpha(Z) = \rho(Z)\langle\cos(\alpha)\rangle(Z) \quad \text{Eq. 44}$$

$$\Phi_\beta(Z) = \rho(Z)\langle\cos(\beta) - 0.5\rangle(Z) \quad \text{Eq. 45}$$

$$\Phi_\gamma(Z) = \rho(Z)\langle\cos(\gamma) - 0.5\rangle(Z) \quad \text{Eq. 46}$$

where  $\rho(Z)$  is the number density of the molecule (water or dioxane) in the corresponding slice of the simulation box. It is important to note that while any two of these angles can describe the orientation of a single molecule relative to the interface,  $\alpha, \beta$  and  $\gamma$  are not independent of each other. To create bivariate angle distribution maps of the water and 1,4-dioxane molecules two independent angles are needed as angular polar coordinates of the interface normal vector (**Figure 18**):  $\alpha$  and  $\delta$ , which are the angle of the molecular dipole vector enclosing with the bilayer normal, and the angle formed by the molecular normal vector and the projection of the interface normal ( $Z$ ) to the plane perpendicular to the molecular dipole vector ( $xy$  plane, shown in blue in **Figure 18**), respectively.

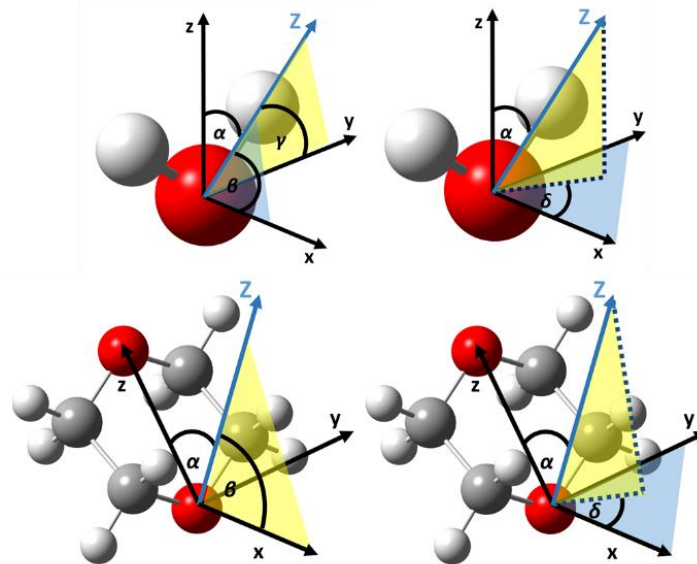


**Figure 18** Definition of the local vectors ( $x, y, z$ ) bound to water and 1,4-dioxane molecules. The orientation of the molecules relative to the membrane normal ( $Z$ ) are defined by  $\alpha, \beta, \gamma, \delta$ .

### 3 COMPUTATIONAL DETAILS

In this chapter the detailed settings of the MD simulations will be summarized. In all studies the simulations were carried out using GROMACS (versions 5.1.2, 5.1.4 and 2019) [79], while VMD [297] was used for molecular visualization. For WT-MD and Metadynamics simulations PLUMED 2.3 [298], [299] was used. In the end of the chapter the validation of the methods is shown.

#### 3.1 TRANSMEMBRANE PENETRATION MECHANISM OF NSO-HET MOLECULES, 1,4-DIOXANE, PHENOL, MORPHOLINE AND OXANE

##### 3.1.1 System Preparation

Total five different systems were examined in this work to understand the effects of NSO-HET molecules on DPPC composed membrane bilayers: DPPC in the presence of 1,4-dioxane (DIOX), phenol (PHE), morpholine (MOR) and oxane (OXA) (**Figure 4**) and a substance free system for comparison. Initial membrane configurations were generated by using CHARMM-GUI [300], [301] with 64 lipid molecules in each membrane leaflet ( $n_{lipid} = 128$ ), and 50 water molecules per headgroup ( $n_{water} = 6400$ ). The size of the membrane was used in several works [84], [107], [110], [302], [303] where it proved to be sufficiently large to reproduce membrane structural parameters, and it is well hydrated as the number of water molecules exceeds the needed value for the hydration of DPPC membranes. [58] Aside from these components an additional 100 NSO-HET molecules have been inserted into each simulation box in random positions (noted as  $N=100$ ), except for the substance free system. Such high concentration ( $c_{MOR} = 74.23 \text{ g/dm}^3$ ,  $c_{PHE} = 80.20 \text{ g/dm}^3$ ,  $c_{OXA} = 73.40 \text{ g/dm}^3$ ,  $c_{DIOX} = 75.10 \text{ g/dm}^3$  [304]) had been chosen to exaggerate the caused structural and energetic changes to distinguish it from statistical noise. [305] CHARMM36 [72] force field was used to model DPPC, CHARMM TIP3P [306] to model water and CGenFF [307] was used to model the NSO-HET molecules. Periodic boundary conditions were applied in  $xyz$  directions in a cubic simulation box.

##### 3.1.2 Parameters of MD simulations

The production runs have been set up with a three step equilibration protocol. As a first step a minimization was carried out with a maximum of 5000 steps. During the first 25 ps long NVT equilibration the P atoms were restrained to their positions along axis Z to preserve the membrane structure [72]. The following equilibration step was carried out for 800 ps in an NPT ensemble using the Berendsen temperature and pressure control. [253] The production runs were 125 ns long where Nosé-Hoover temperature [254], [255] and

Parrinello-Rahman pressure [257] control was used. Out of the 125 ns of the last simulation step the first 25 ns were discarded from the evaluation, as in previous publications [78], [304] it has been found that in the case of NSO-HET containing systems the box size – thus the membrane parameters – still drastically change in this time interval.

During all simulation steps the temperature was 330 K and the pressure was 1 atm, to ensure that a biologically relevant alpha-crystalline phase ( $L_\alpha$ ) is maintained throughout the simulations [308]–[310]. The coupling constants for temperature and pressure control were set as  $\tau_T = 1.0$  ps and  $\tau_p = 5.0$  ps respectively. Heavy atom-hydrogen distances were constrained by using the P-LINCS algorithm [252] and SETTLE [251] was used to keep water molecules rigid. The cut-off for non-bonded interactions was set as 1.2 nm [72] while the smooth Particle Mesh Ewald summation method [311] was used for the treatment of long distance electrostatic interactions. During the simulations the equations of motions were integrated at every 2 fs and coordinates were saved in every 10 ps. For each system 500 ns of total production runs were carried out from five parallel simulations. Results are presented as averages of the five repeats and their standard deviation.

### 3.1.3 Free Energy of Permeation

Free energy was calculated from classical molecular dynamics simulations based on the density profiles of the investigated compounds along axis Z, by using WT-MD and in the case of 1,4-dioxane metadynamics was also used.

In WT-MD simulations the collective variable was selected to sample the free energy profile of the NSO-HET molecules moving along the membrane normal (Z), from the bulk phase to the opposite side of the membrane. Throughout WT-MD simulations the pulled molecules were treated as a whole, and the center of mass was used to sample the free energy profile. During these simulations the bias potential was set to be 8.0 and Gaussians were deployed at every 3 ns, with an initial height of 2.2 kJ/mol and width of 0.1 nm. The walls of the pulling mechanism were 3.7 nm away from the bilayer center. Other parameters of the WT-MD were identical to the production runs as in **Section 3.1.2**.

In the case of the metadynamics simulations of 1,4-dioxane Gaussians were deposited at every 2500 ps, with a height of 0.1 kJ/mol and a width of 0.5 nm. Walls for the pulling were also set 3.7 nm from the center of the membrane bilayer.

A total 11 systems were compared in this study by the means of WT-MD. The penetration of NSO-HET and water molecules (in the presence of NSO-HET molecules) into DPPC membranes. In the case of phenol and 1,4-dioxane the penetration was investigated in two different concentrations 80.20 g/dm<sup>3</sup> (N=100) and 0.080201 g/dm<sup>3</sup> (N=1) and

75.10 g/dm<sup>3</sup> (N=100) and 0.7510 g/dm<sup>3</sup> (N=10) respectively, while for morpholine and oxane the previously indicated concentrations were used solely. The length of WT-MD simulations in the case of NSO-HET molecules were 1  $\mu$ s long, while in the case of water molecules 500 ns were sufficient for convergence.

## **3.2 EFFECTS OF THE DERIVATIVES OF THE CO<sub>2</sub> AND 1,3-BUTADIENE REACTION ON BIOMEMBRANES**

### **3.2.1 System Preparation**

#### **3.2.1.1 OPLS-AA membranes**

In this study all-atom optimized potentials for liquid simulations (OPLS-AA) membranes were used for primary analysis. The initial membrane configuration was obtained from the work of Maciewski et al. [312], where 64-64 lipids can be found in each membrane leaflet ( $n_{lipid} = 128$ ) while an additional 50 water molecules per headgroup were inserted in the simulation box ( $n_{water} = 6400$ ). Lipid molecules were modelled by OPLS-AA [312] and water molecules by TIP3P [312] in a cubic simulation box, using periodic boundary conditions.

#### **3.2.1.2 Studied organic molecules**

The OPLS-AA force field parameters with 1.14\*CM1A partial atomic charges have been generated using the LigParGen [313]–[315] for all the studied organic molecules. Total 6 different systems were used to understand the structural effects of the products of CO<sub>2</sub>-1,3-butadiene reaction on biological membranes, and pure DPPC membranes were used as reference: DPPC in the presence of EVL, LAC2, LAC3, BDDI, AC1 and AC2 (**Figure 5**).

After the equilibration of the DPPC membranes, an additional 100 permeant molecules have been inserted into simulation boxes in random positions. The final concentrations are  $c_{EVL} = 119.19$  g/dm<sup>3</sup>,  $c_{LAC2} = 119.04$  g/dm<sup>3</sup>,  $c_{LAC3} = 118.81$  g/dm<sup>3</sup>,  $c_{BDDI} = 115.67$  g/dm<sup>3</sup>,  $c_{AC1} = 118.5$  g/dm<sup>3</sup> and  $c_{AC2} = 118.65$  g/dm<sup>3</sup>.

### **3.2.2 Parameters of MD simulations**

#### **3.2.2.1 Membrane simulations**

The same simulation protocol was applied here as in the case of the NSO-HET molecules. Each simulation was 1125 ns long, except for the additive free DPPC membranes, where the simulation was 125 ns long. Out of these simulations the first 25 ns were considered as part of the equilibration, so total we had 1100 and 100 ns long simulations to evaluate.

#### **3.2.2.2 Pure Liquid Densities**

Pure liquid densities of the compounds were obtained from pure liquid simulations

where 1500 molecules were inserted into each simulation box. The simulation protocol was the same as in the case of membrane simulations, where production runs were 20 ns long. The density distribution of the liquid phase was obtained by Voronoi tessellation as described in **Chapter 2.3.1** and. [271]

### **3.2.3 Free Energy Calculations**

#### **3.2.3.1 Free Energy of Hydration**

Hydration free energies ( $\Delta G_{\text{hyd}}$ ) of the solutes were calculated based on the thermodynamic cycle, by annihilating the molecules from vacuum to solvent phase. [316] To obtain  $\Delta G$  of the investigated compounds both ab initio and MD based methods were used.

##### **3.2.3.1.1 Ab initio Based Calculations of $\Delta G_{\text{hyd}}$**

For the ab initio calculations the G3MP2B3 composite method [317], [318] was used as implemented in the Gaussian09 [197] program package. According to this method, single point calculations were carried out using QCISD(T)/6-31G(d) and MP2/GTMP2large levels of theories based on B3LYP/6-31G(d) [319] geometries. During optimization ‘tight’ convergence criteria was applied, while the harmonic wavenumbers were scaled by a factor of 0.96 [317], [318]. For the solvent phase calculations SMD [266] was used as an implicit solvent model for water to obtain  $\Delta G_{\text{hyd,G3MP2B3}}$  values.

##### **3.2.3.1.2 MD Based FEP Calculations for $\Delta G_{\text{hyd}}$**

To obtain the hydration free energies ( $\Delta G_{\text{hyd,MD}}$ ), a single solute was hydrated by 2000 TIP3P water molecules, which provided a sufficiently large simulation box to avoid unwanted interactions with the periodic images. While the general settings of the simulations were the same, only 20 ns production runs were conducted. A total of 40 windows were used to obtain  $\Delta G_{\text{hyd,MD}}$ . First the van der Waals interactions were scaled ( $\lambda_{\text{vdw}}$ ) to full strength (from 0 to 1) than the Columbic interactions ( $\lambda_{\text{Col}}$ ) (from 0 to 1 also) to avoid extreme attractions in the electrostatic potential. [316], [320] The scaling went linearly increasing by 0.05 in each step. Free energy was computed using the Bennett Acceptance Ratio (BAR) [321] algorithm as implemented in GROMACS and the free energy difference ( $\Delta G_i$ ) is calculated between each consecutive simulation window.

In order to validate the obtained  $\Delta G_{\text{hyd}}$  values, phenol was used as a test compound, as for the investigated molecules no hydration free energy data was available. The applied methods prove to be in a good agreement with the available experimental values (at  $T = 298.15 \text{ K}$   $\Delta G_{\text{hyd,EXP,1}} = -27.18 \text{ kJ/mol}$  [322],  $\Delta G_{\text{hyd,EXP,2}} = -26.77 \text{ kJ/mol}$  [323]). In this

case the MD based calculation of the hydration free energy was found to be more accurate ( $\Delta G_{\text{hyd,MD}} = -25.58$  kJ/mol) compared to the ab initio based method ( $\Delta G_{\text{hyd,G3MP2B3}} = -22.69$  kJ/mol).

### 3.2.3.2 Free Energy of Penetration

To characterize the energetic nature of the penetration mechanism of the hereby investigated compounds, well-tempered metadynamics simulations were carried out and the density based method was also applied. CV(s) was selected to sample the free energy difference of the solute molecules moving along the membrane normal from the bulk phase to the other side of the membrane. The settings of WT-MD simulations, such as the time length of the addition of Gaussians, their width and height, the bias factor and the position of walls are shown in **Table 4**. Other parameters of the WT-MD were identical to the production runs (see **Chapter 3.2.2.1**), while their length was 1  $\mu\text{s}$  long.

**Table 4** Parameters of the WT-MD simulations for studying the penetration of the derivatives of 1,3-butadiene and CO<sub>2</sub> reaction. In the table  $\omega$  indicates the height and  $\sigma$  indicates the width of the Gaussians and  $t'$  is the time difference between Gaussians are deposited.

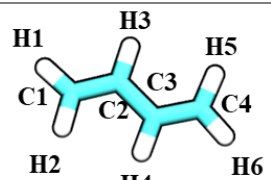
Permeants	N	$\omega$ (kJ/mol)	$\sigma$ (nm)	$t'$ (ns)	Bias factor	Position of the Walls (nm)
EVL	1	1.0	0.35	3	10	3.5
	100	10	0.3	1	25	3.4
LAC2	1	10	0.1	1	15	3.6
	100	10	0.3	1	25	3.8
BDDI	1	10	0.3	1	35	3.8
	100	2.2	0.1	3	15	3.6
AC1	1	1.0	0.1	3	10	3.5
	100	2.2	0.1	3	15	3.15

## 3.3 VAPOR LIQUID EQUILIBRIUM AND SUPERCRITICAL PHASE OF 1,3-BUTADIENE

### 3.3.1 System Preparation

**Table 5** Interaction parameters and the schematic figure of 1,3-butadiene obtained from LigParGen [313]–[315]

Atom name	$\sigma$ (Å)	$\epsilon$ (kJ/mol)	q (e)
C1,C4	3.550	0.317984	-0.2344
C2,C3	3.550	0.317984	-0.1558
H1,H2,H5,H6	2.500	0.125520	0.1280
H3,H4	2.500	0.125520	0.1341



The all-atom optimized potentials for liquid simulations (OPLS-AA) force field parameters with 1.14\*CM1A partial atomic charges for 1,3-butadiene have been generated

using the LigParGen [313]–[315]. The obtained Lennard-Jones parameters ( $\sigma$  and  $\epsilon$ ) and formal charges ( $q$ ) are shown in **Table 5**, further force field parameters are collected in **SFigure 1** of [271]. The initial configurations were created by the GROMACS built-in program inserting a total 3000 butadiene molecules into an initial simulation box (6.5 nm×6.5 nm×10 nm).

A unified radial distribution of the molecules at larger distances cannot be assumed for two-phase and supercritical system due to their large density inhomogeneities. [221] Therefore, for each simulation, the cut-off distance was set to 3.0 nm which was smaller than half the dimension of the liquid phase at each investigated temperature. [218], [270] The electrostatic interactions have been accounted using the SPME method [311], which have been found to be appropriate for VLE simulations. [324] In all of these MD simulations, the heavy-atom-hydrogen distances have been fixed by the means of P-LINCS [252] algorithm as implemented in GROMACS. For both NVT and NPT simulations, 2 fs time step was chosen.

### 3.3.2 Two-phase Molecular Dynamics (2 $\phi$ MD) simulations

To obtain the slab geometry the initial simulation box was expanded along the Z axis to 90 nm. First, the initial configuration was optimized until the maximum force was less than 500 kJ/mol. This was followed by a 1 ns long equilibration run in NVT ensemble using Berendsen thermostat [253], where the coupling constant was set to 1.0 ps. The production runs were 20 ns long, using NVT ensemble, where temperature was controlled using the Nosé-Hoover thermostat [254], [255] with a coupling constant of 1.0 ps. The equations of motion were integrated with 2 fs time steps and structures have been saved to a trajectory file for analysis in every 10 ps. During evaluation only the final 10 ns were analyzed to ensure the equilibrium state achieved for the two-phase (2 $\phi$ ) systems. Simulations were carried out at 16 different temperatures in the range of 278-448 K.

According to the 2 $\phi$ MD methodology [217], [270] suggested by Fern *et al.*, one-phase (1 $\phi$ ) simulations have been conducted both in liquid and vapor phase at each investigated temperature as a self-consistency check to ensure that the correct values for the density are obtained, thus removing all arbitrary choices in phase definition. Gas phase simulations were ran in the NVT ensemble with same settings as the general slab simulations, while NPT ensemble was used for liquid simulations where pressure was kept at 1 bar by using Parrinello-Rahman pressure control [257] with a coupling constant of 1.0 ps during the 10 ns long production run. The initial configurations of the 1 $\phi$  simulations were selected from the final configurations of the slab simulations.

### 3.3.3 Supercritical phase simulations

Above the critical point the two phases disappear thus  $2\phi$ MD is not applicable anymore thus supercritical simulations have been conducted in the NPT ensemble. The pressure and temperature dependence of the supercritical phase structure has been tested by keeping either the temperature ( $T = 430$  K) or pressure ( $P = 53$  bar) constant, then raising the pressure or temperature gradually by 10 bar or 10 K in the range of 410 K-470 K and 43-93 bar, respectively. Other parameters of the simulations are equivalent with the liquid phase simulations.

## 3.4 VALIDATION

### 3.4.1 CHARMM and OPLS-AA lipid force fields

In order to make sure that the hereby used settings with the OPLS-AA and CHARMM36 force fields are correct the obtained data was compared with literature data. All literature data are from  $L_\alpha$  phase membranes, such as the data from simulations. A good agreement was found in the case of all membrane parameters, electron density profiles and deuterium order parameters. The comparison of membrane parameters are found in **Table 6** while EDP-s and  $S_{CD}$ -s are shown in **Figure 19**. Based on these results the hereby used methods with the applied force fields were suitable to investigate structural membrane parameters, as almost all data is within the range of absolute deviation, except in the case of VPL, but the deviation is below 2% even in this case.

**Table 6** Comparison of the values of the obtained membrane parameters with  $L_\alpha$  phase experimental data

Membrane parameter	Experimental data	CHARMM36 (330K)	OPLS-AA (323K)
APL (nm <sup>2</sup> )	$0.629 \pm 0.013$ [59]	$0.618 \pm 0.014$	$0.637 \pm 0.014$
VPL (nm <sup>3</sup> )	1.232 [60]	$1.214 \pm 0.00023$	$1.203 \pm 0.0098$
D <sub>HH</sub> (nm)	3.83 [60]	$3.70 \pm 0.45$	$3.64 \pm 0.34$
K <sub>A</sub> (mN/m)	$231 \pm 20$ [60]	$214.57 \pm 34.8$	$225.31 \pm 6.10$

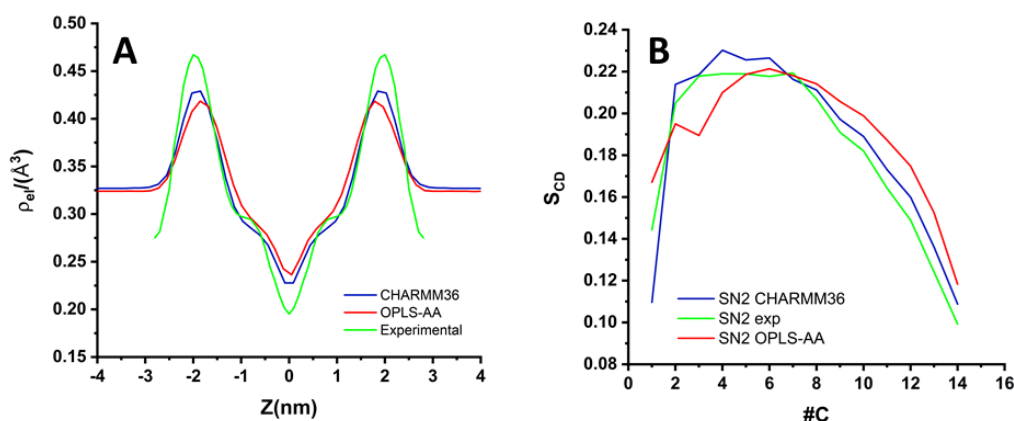


**Figure 19** The comparison of CHARMM36 (blue), OPLS-AA (red) and experimental (green) data of electron density profiles [58] (panel A) and deuterium order parameters [325] (panel B) of DPPC membranes

### 3.4.2 Cut-off dependence of the density of 1,3-butadiene

As the cut-off value for the simulations were increased compared to the default value, the dependence of density on the cut-off during simulations of 1,3-butadiene have been investigated throughout the entire temperature range for both the VPL and the supercritical phase. The effect of the increased cut-off values is negligible on the density of the individual vapor and liquid phases (**Figure 20**) and the computed densities were also consistent with the experimental values [326] shown in **Table 7**.

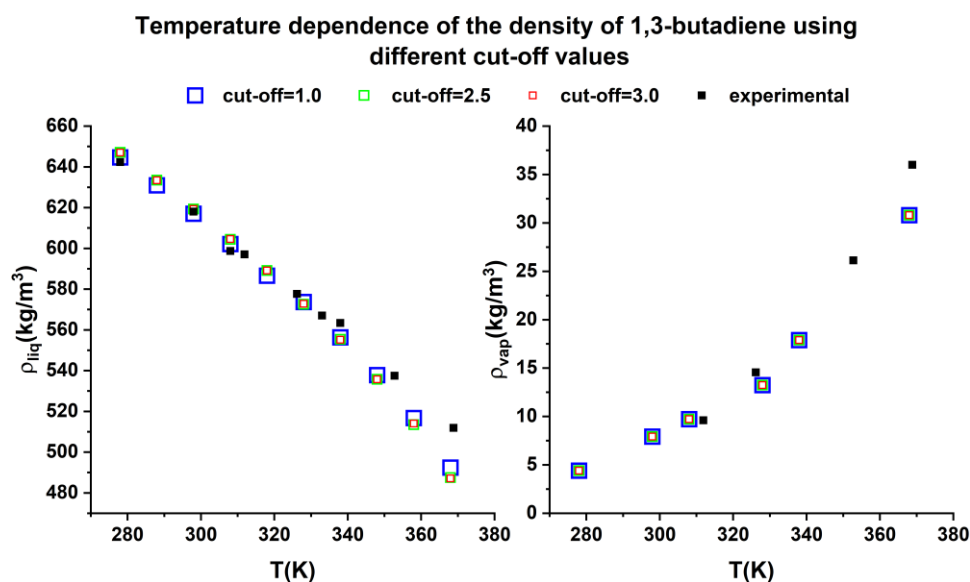


**Figure 20** Temperature dependence of liquid ( $\rho_{liq}$ ) and vapor ( $\rho_{vap}$ ) phase densities of 1,3-butadiene by comparing the effects of different cut-off values in nm. All experimental data have been taken from the Dortmund Databank [326]

**Table 7** Experimental [326] and calculated densities of vapor and liquid densities of 1,3-butadiene at different temperatures below the supercritical temperature.

T (K)	$\rho_{\text{vap,exp}}$ (kg/m <sup>3</sup> )	$\rho_{\text{liq,exp}}$ (kg/m <sup>3</sup> )	$\rho_{\text{vap,2}\phi\text{MD}}$ (kg/m <sup>3</sup> )	$\rho_{\text{liq,2}\phi\text{MD}}$ (kg/m <sup>3</sup> )
278		642.35	3.97±0.02	647.56±0.22
298		618.02	6.74±0.04	615.47±0.8
308		598.731	8.89±0.05	599.37±0.89
311.88	9.61	597.05		
318			10.38±0.54	591.46±0.98
326.19	14.56	577.6		
328			14.77±0.38	576.13±0.98
333		567		
338		563.38	17.3±0.75	559.23±1.15
352.77	26.13	537.46		
368			33.23±0.86	516.45±0.78
368.82	36	511.9		
388			44.44±0.46	469.28±1.06
408			73.57±0.35	

Near the supercritical phase the dependence of densities at different pressures and temperatures on cut-off can be seen on **Figure 21**, where it can be stated that the effect of cut-off only counts at higher pressures and in the region of the phase transition to SCF.

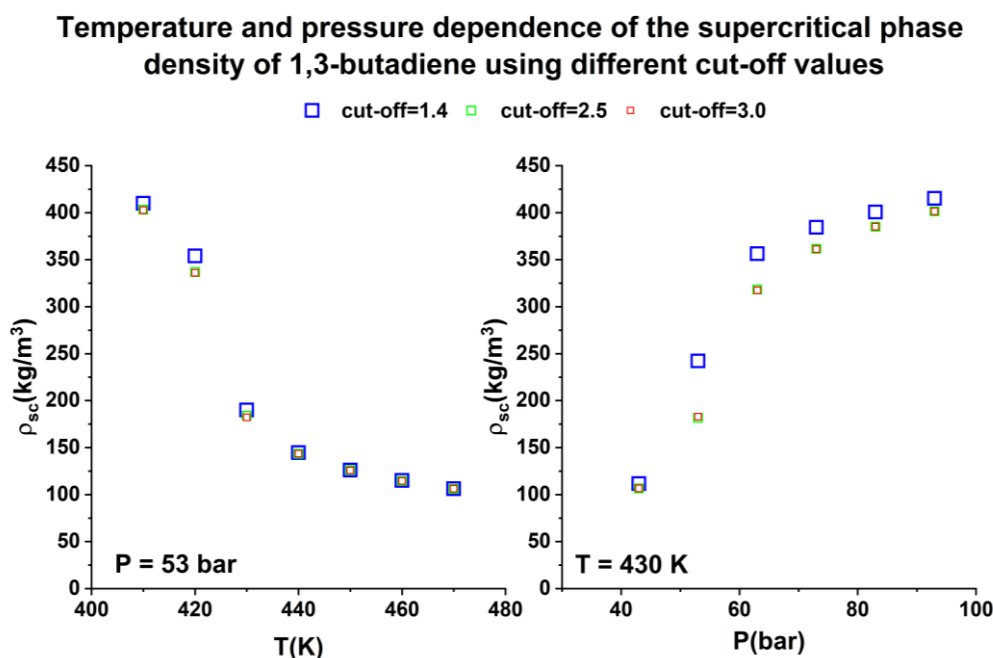


**Figure 21** Temperature dependence of supercritical phase densities of 1,3-butadiene by comparing the effects of different cut-off values. All experimental data have been taken from the Dortmund Databank [326]

## 4 RESULTS AND DISCUSSION

As described in the Introduction, chemicals can alter the function of cells by interacting with and/or permeating inside biological membranes. A possible method for understanding this process is by using Molecular Dynamics simulations, with which several structural parameters of the membrane and the energetics of the permeation process can be analyzed in detail.

### 4.1 TRANSMEMBRANE PENETRATION MECHANISM OF NSO-HET MOLECULES, 1,4-DIOXANE, PHENOL, MORPHOLINE AND OXANE

The goal of this study was to understand the membrane structure altering properties of 1,4-dioxane, oxane, phenol and morpholine (NSO-HET molecules), and also to investigate the energetics of penetration by applying two different methods. For the penetration mechanism two concentrations were used in the case of 1,4-dioxane and phenol, to understand the possible effect of concentration on the mechanism.

#### 4.1.1 Effect of NSO-HET molecules on density profiles

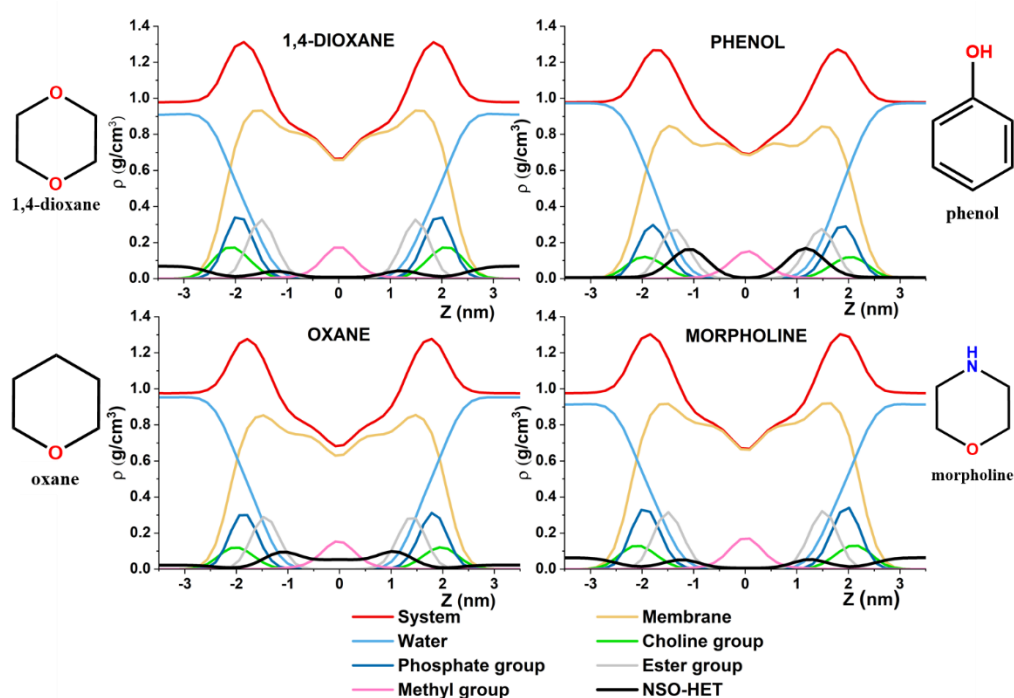


**Figure 22** Mass density distributions obtained from MD simulations of the DPPC composed membrane systems along the membrane normal (Z) in the presence of the different NSO-HETs, 1,4-dioxane, phenol, oxane and morpholine. The overall mass densities are decomposed into subsections to highlight the inner structure of the biomembranes. Red – complete system, Orange – DPPC, light blue – water, green – choline, dark blue – phosphate, gray – ester, pink – terminal methyl-groups, black – NSO-HETs.

The mass density profiles along the membrane normal are shown in **Figure 22** for the studied systems composed of DPPC, water and NSO-HET molecules. Besides the total mass

density, the spatial contributions of the additional cyclic compounds and water molecules as well as that of phosphate, methyl, choline and ester groups of DPPC are presented. Out of the investigated NSO-HETs, phenol has the most visible effect on the density distribution of DPPC membranes as the distribution of the selected atomic groups having larger variance. This phenomena indicates that the membrane becomes less structured and the position of the groups become less delimited in position. Oxane has a similar effect but with smaller visible extent.

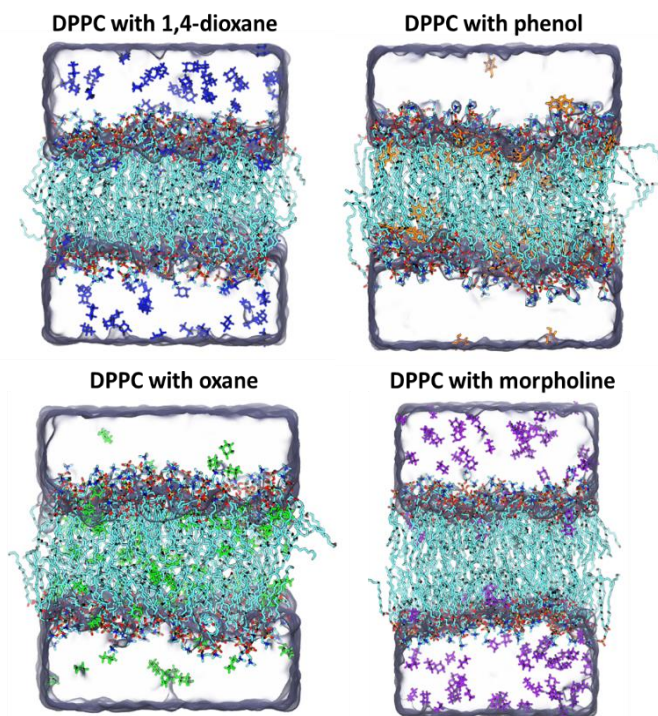


**Figure 23** Snapshots from the MD simulations conducted for DPPC and different NSO-HET molecules, 1,4-dioxane, phenol, oxane and morpholine.

The equilibrium snapshots of the simulated systems are shown in **Figure 23** and the non-symmetrized mass density profiles of solely the NSO-HET molecules are shown in **Figure 24**. While most of 1,4-dioxane and morpholine molecules are found dissolved in the bulk phase, only a small amount ( $\sim 0.02 \text{ g/cm}^3$ ) of oxane molecules are outside the membrane, and only a negligible amount of phenol molecules are in this region - as presumed by their positive  $\log(K_{OW})$  (see **Table 1**). From this the partition coefficient can also be calculated, which shows the average proportion of NSO-HET molecules between the bulk phase and the membrane interior. In the case of morpholine and dioxane almost two times more (52% and 41% respectively) NSO-HETs can be found in the bulk phase. At the same time in the case of oxane and phenol 3.5 and 10 times more NSO-HETs are found in the

membrane interior. In the cases of the latter two cyclic compounds the membrane bilayer is also found to be in a more disturbed and disordered phase.

Around the position of the head groups ( $|Z| \approx 2$  nm, **Figure 22**) the density of all NSO-HETs is minimal. After the permeants penetrate inside the membrane (to the site of the ester-groups) their local concentration grows and reaches a local maximum in the case of 1,4-dioxane and morpholine while a global maximum concentration was achieved here for oxane and phenol. The maximum concentration of oxane is  $0.095 \text{ g/cm}^3$ , while for phenol it is almost the double ( $0.17 \text{ g/cm}^3$ ). In the center of the bilayer the concentration of all NSO-HET molecules is negligible, except for oxane, of which concentration is  $0.057 \text{ g/cm}^3$ . By quantifying this data it can be said that in average in the vicinity of each ten DPPC molecules two morpholine or dioxane, six oxane and seven phenol molecules are found.

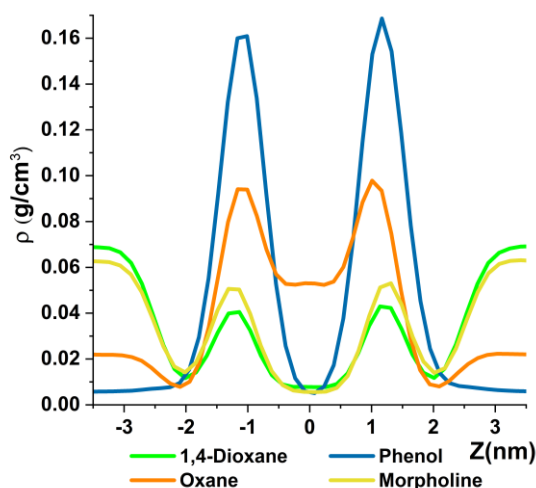


**Figure 24** Non-symmetrized mass density profiles obtained from classical MD simulations of the NSO-HET molecules in the vicinity of DPPC model membranes.

#### 4.1.2 The Effect of NSO-HETs on Structural Membrane Parameters

Structural membrane parameters of the simulated membrane systems are shown in **Figure 25**. All investigated NSO-HETs affect DPPC membranes in a similar way, while the magnitude of change is different. The presence of the pollutant molecules lead to a significant increment in the values of both APL and VPL, while the thickness of the membrane and the orderliness of the lipid tails decrease. Based on the mass density profiles, all NSO-HET molecules have a density peak at the inner site of the ester groups. As the cyclic compound penetrates between the membrane headgroups the membrane expands as shown by the growth of APL and VPL. This bloating leads to a larger lateral outspread of lipid tails in a more disordered conformation with a shorter relative length.

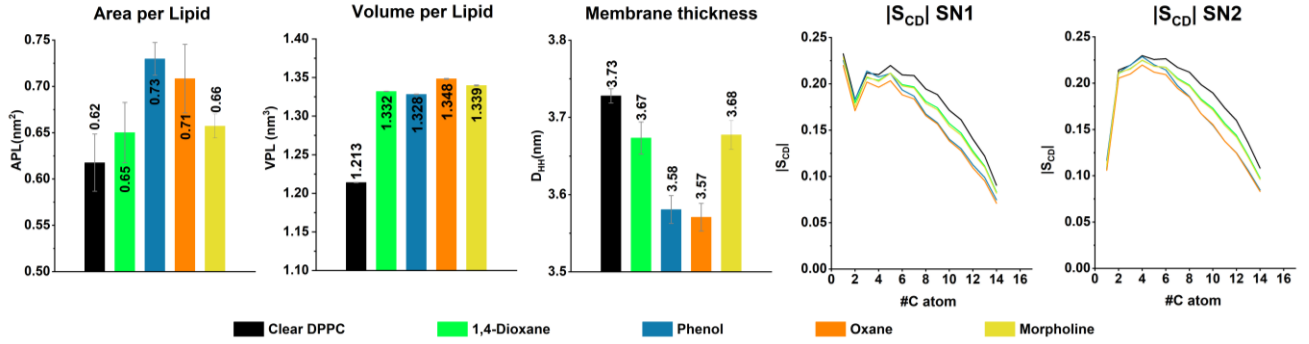


**Figure 25** Area per lipid (APL in nm<sup>2</sup>), Volume per lipid (VPL in nm<sup>3</sup>), Membrane thickness (D<sub>HH</sub> in nm) and Deuterium Order Parameter (S<sub>CD</sub>) of the investigated DPPC membrane – NSO-HET systems obtained from MD simulations. The structural parameters of clear DPPC membranes are shown as reference. Clear DPPC membrane is indicated with black, 1,4-dioxane, phenol, oxane and morpholine are indicated with green, blue, orange and yellow respectively.

1,4-dioxane and morpholine have an almost identical effect on the investigated membrane parameters, while the presence of phenol or oxane causes a more drastic change in most cases. While APL is the largest in the case of phenol, the VPL is the lowest out of the investigated compounds. The membrane thickness is the smallest in the presence of oxane molecules which found with 0.057 g/cm<sup>3</sup> density in the central region of the bilayer. This phenomena is responsible for the VPL being the largest in the case of this NSO-HET. The most disordered lipid chains can be found in the case of oxane and phenol - which are almost identical for the last 7 carbon atoms in the case of both acyl chains – which found in the largest concentration inside the membrane bilayer. Volume per lipid was obtained also as the product of APL and the thickness of a single membrane layer (D<sub>HH</sub>/2), with which the membrane expanding effects of the NSO-HET molecules was confirmed.

Based on the density distribution of the NSO-HET molecules and the obtained membrane thickness the membrane-bulk phase partition coefficient can be calculated by the following equation:

$$P_{mem/bulk} = \frac{\int_{-D_{HH}/2}^{+D_{HH}/2} \rho_{NSO-HET}(Z) dZ / D_{HH}}{(\int_{-Z/2}^{+Z/2} \rho_{NSO-HET}(Z) dZ - \int_{-D_{HH}/2}^{+D_{HH}/2} \rho_{NSO-HET}(Z) dZ) / (Z_{box} - D_{HH})} \quad Eq. 47$$

,where  $\rho_{NSO-HET}(Z)$  is the density of the NSO-HET molecule, D<sub>HH</sub> is the membrane thickness and Z<sub>box</sub> is the length of the z axis of the simulation box. The logarithm of P<sub>mem/bulk</sub> can be then directly compared to the experimental logK<sub>OW</sub> shown in **Table 1**. The obtained values were the following: -0.36, 0.95, 0.56 and -0.26 for 1,4-dioxane, phenol, oxane and morpholine respectively which match the trends of octanol-water partition coefficients.

### 4.1.3 WT-MD based free energy profiles of NSO-HETs

The obtained free energy profiles using WT-MD of phenol, oxane, morpholine and 1,4-dioxane can be seen in **Figure 26**, where similar amount of NSO-HET molecules ( $N = 100$ ) are present in the simulated systems. For the representation, the bulk phase was used as the reference point, as 0 kJ/mol.

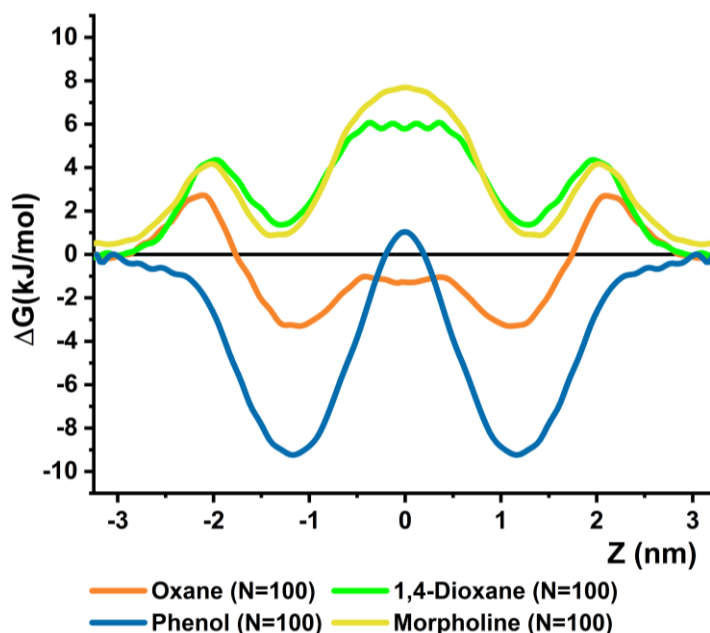


**Figure 26** Free energy profiles obtained by WT-MD of NSO-HETs (phenol, morpholine, oxane and 1,4-dioxane indicated with blue, yellow, orange and green, respectively) penetrating inside DPPC membranes.

To the best of our knowledge, no reported free energy profile had been published for the systems studied in this work, only exception is the case of phenol [327] for which the free energy profile in an aqueous DMPC membrane was obtained using a model extension of semiempirical mean field COSMO-RS approach (COSMOmic). From this calculation, two distinct minima had been identified along the DMPC membrane surface normal: global minimum at 1.2 nm from the membrane center with roughly 14 kJ/mol and a local minimum at 1.8 nm with 10 kJ/mol. Although the latter shallow minimum is not found in our model system, the main minimum is consistent with our membrane model.

Morpholine and 1,4-dioxane have a similar free energy profile, which explains their similar membrane structure altering properties and mass density profiles. The lowest free energy corresponds to the bulk water region ( $|Z| > 3$  nm) which is therefore the thermodynamically preferred state for 1,4-dioxane and morpholine. As these pollutants approach the bilayer surface  $\Delta G$  starts to grow sharply until it reaches the head groups where the free energy profile reaches a relatively small local maximum of  $\Delta G \approx 5.5$  kJ/mol at

$|Z| \approx 2$  nm. At the inner site of the ester groups,  $|Z| \approx 1.2-1.5$  nm, both morpholine and 1,4-dioxane reaches a metastable state, where free energy drops down to 0.9 kJ/mol in the case of morpholine and 1.6 kJ/mol for dioxane. The local density maximum of both NSO-HETs is consistent with this free energy plateau. As the compounds approach the bilayer center the free energy steeply grows until it reaches the global maximum of 6 kJ/mol and 7.7 kJ/mol for dioxane and morpholine, respectively.

On the other hand phenol and oxane behaves significantly different. The bulk water phase and the membrane central region are thermodynamically the least favorable for phenol, which supports the density profile of this NSO-HET. At the inner site of the ester groups, at  $|Z| \approx 1.1 - 1.2$  nm, phenol has its global free energy minimum ( $\Delta G = -9.3$  kJ/mol), which cohere with its high mass density in this position. In the case of oxane the global free energy maximum is found at the headgroups region of the membrane ( $|Z| \approx 2$  nm), where  $\Delta G = 3.3$  kJ/mol. After passing the head groups region the free energy profile of oxane decreases, reaching its global free energy minima ( $\Delta G = -3.3$  kJ/mol) at  $|Z| \approx 1.0-1.2$  nm at the inner site of the ester groups, and even at the center it has a free energy barrier of only -1.3 kJ/mol. This explains why a reasonable amount ( $0.057$  g/cm<sup>3</sup>) of oxane molecules can be found at the bilayer center.

#### **4.1.4 Concentration Dependence of Free Energy of Permeation. 1,4-dioxane and phenol.**

In the case of 1,4-dioxane and phenol the concentration dependence of the free energy of permeation was also investigated. While in the former case metadynamics was used for comparison, and it was validated by using WT-MD, in the latter case solely WT-MD was used.

The obtained free energy profiles of 1,4-dioxane penetration along axis Z are shown in **Figure 27**. In the case of dioxane the diluted system is one order of magnitude smaller compared to the DIOX-DPPC system in the previous sections. As the metadynamics and the WT-MD results agreed within chemical accuracy, further on only the metadynamics results will be discussed in this case. The starting point of the growth of free energy appears to be closer to the bilayer center for the more concentrated system by 0.5 nm while the relative free energy values appear to be somewhat higher for the diluted system ( $\Delta G_{diluted}$ ) than that of the concentrated one ( $\Delta G_{conc}$ ). This means that the penetrating dioxane molecules make the membrane more accessible for additional dioxane molecules. The height and the position of the local free energy barrier at the sight of the head groups shows only a weak concentration dependence:  $\Delta G_{diluted} = 8.3$  kJ/mol at  $|Z| = 2.2$  nm and  $\Delta G_{conc} = 6.5$  kJ/mol at

$|Z| = 1.97$  nm for the concentrated system. As dioxane penetrates inside the membrane the free energy profile reaches a metastable state where  $\Delta G_{conc} = 6.4$  kJ/mol and  $\Delta G_{diluted} = 3.3$  kJ/mol, which corresponds to the site of the ester groups ( $|Z| = 1.6-1.1$  nm). As 1,4-dioxane approaches the bilayer center free energy starts to grow steeply again until it reaches the global free energy maximum in the bilayer center where  $\Delta G_{conc} = 16.7$  kJ/mol and  $\Delta G_{diluted} = 10.4$  kJ/mol.

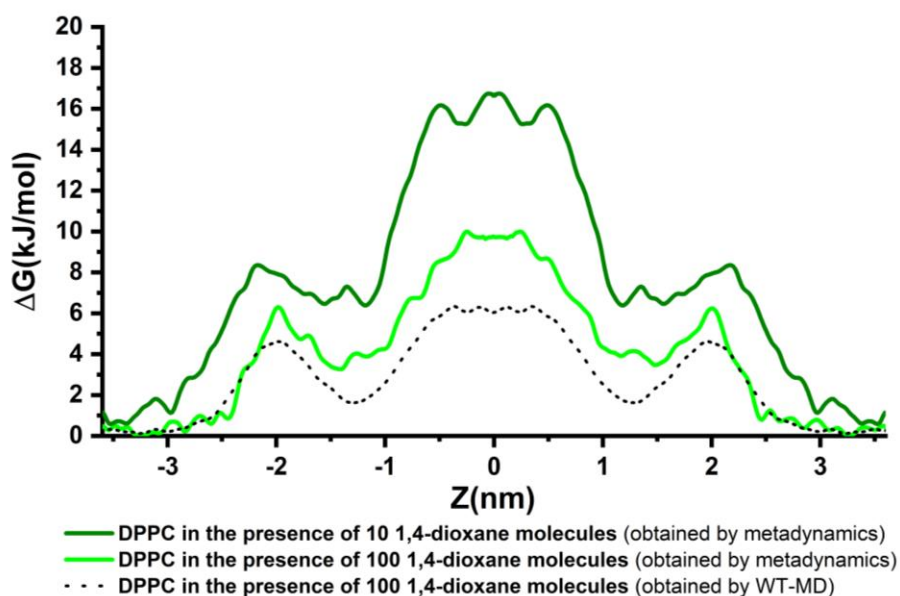


**Figure 27** Free energy profile of 1,4-dioxane penetration into a DPPC bilayer. The light green curve represents the results of the metadynamics simulations for the system having 100 1,4-dioxane molecules in the simulation (the average dioxane concentration is  $0.07510$  g/cm<sup>3</sup>), while dark green is for  $0.007510$  g/cm<sup>3</sup> dioxane concentration. The dashed black curve indicates the results of the WT-MD simulation carried out for the system having 100 1,4-dioxane molecules. The estimated error of  $\Delta G$  is 4 kJ/mol.

Molecules with both hydrophilic and lipophilic groups demonstrate a sinusoidal pattern where the free energy decreases near the interface and increases at the center of the membrane bilayer. This pattern is commonly witnessed among biomolecules such as methanol [328], [329] or acetone [330], which is similar to the obtained results for 1,4-dioxane.

Due to the relatively small height of the free energy barrier, DPPC membranes can be permeable for 1,4-dioxane which effect can be further enhanced by increasing dioxane concentration. This allows us to speculate that the presence of dioxane might also make the membrane more permeable for additional molecules, similar to the effects of alcohol. [331]

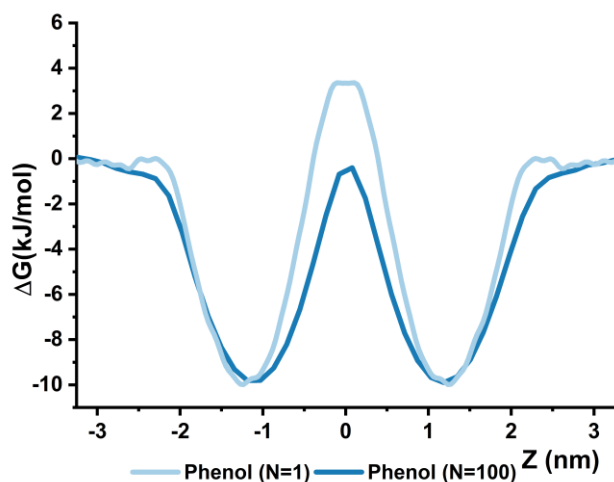


**Figure 28** Free energy profiles obtained by WT-MD of phenol penetrating inside DPPC membranes in two different concentrations ( $c_{N=100} = 0.08020 \text{ g/cm}^3$  and at  $c_{N=1} = 0.0008020 \text{ g/cm}^3$ ) where either 100 or 1 phenol is present in the simulation box indicated with dark and light blue, respectively.

To further test this finding, WT-MD simulations for phenol were carried out in two different concentrations, at  $c_{N=100} = 0.0802 \text{ g/cm}^3$ , concentrated systems and at  $c_{N=1} = 0.000802 \text{ g/cm}^3$ , diluted systems, respectively. As **Figure 28** shows, the obtained free energy profiles reinforce our previous findings, since the trends of both profiles are similar: the only preferred position for phenol molecules are on the inner side of the ester groups at  $|Z| \approx 1.2 \text{ nm}$ , where  $\Delta G = -9.8 \text{ kJ/mol}$ . In the bulk phase the free energy is relatively constant until  $|Z| \approx 2.1 \text{ nm}$  in the diluted systems. On the contrary, at high phenol concentration, between  $|Z| \approx 3.5\text{-}2 \text{ nm}$ , the free energy decreases uniformly from  $0 \text{ kJ/mol}$  to  $-1.9 \text{ kJ/mol}$ . The penetration through the membrane headgroups is barrierless at low phenol concentration. The largest free energy difference between the two free energy profiles is found at the bilayer center, ( $\Delta G_{N=1} = 3.3 \text{ kJ/mol}$  and  $\Delta G_{N=100} = 1.2 \text{ kJ/mol}$ ). While this difference does not exceed the limit of the chemical accuracy, the trend seems to be constant and in line with the results of 1,4-dioxane.

#### 4.1.5 Free energy profile of penetrating water molecules in the presence of NSO-HETs.

In principle, cyclic compounds can also change the membrane properties in such a way that the membrane becomes more permeable to additional molecules, which can result in the alteration of membrane functions. To investigate this scenario, a single water molecule has been pulled into each bilayer in the case of all simulated systems by using WT-MD of which free energy profiles are shown in **Figure 29**. Additive free (pure) DPPC membranes were used as a reference for these simulations which reproduce both the shape of the profile and the height of the free energy barrier in Ref. [107].

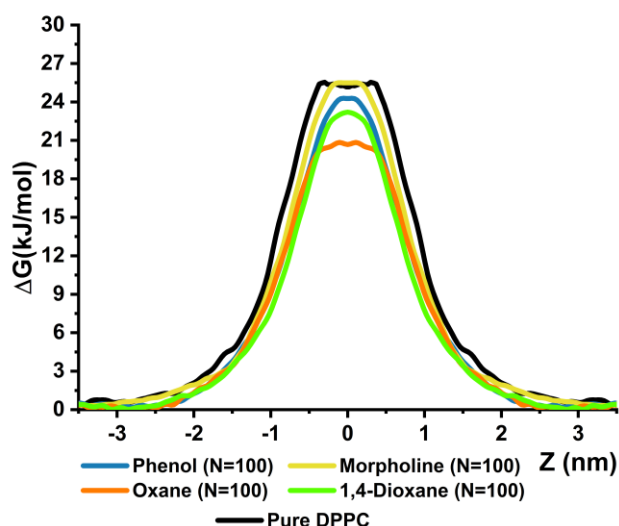


**Figure 29** Free energy profiles obtained by WT-MD of a single water molecule penetrating inside DPPC membranes in either clear environment (black), or in the presence of 100 NSO-HET molecules: phenol (blue), morpholine (yellow) or oxane (orange).

The shapes and tendencies of the free energy profiles of all different systems are similar. After reaching the membrane headgroups between  $|Z| \approx 3.2$ - $2.2$  nm, of which position depends on the thickness of the bilayer, the free energy of water molecules starts to rise steeply until reaching the bilayer center, where one single peak is found. In the case of pure DPPC membranes this peak is at 25.4 kJ/mol. For high concentration of morpholine and phenol, the height of the free energy barrier is within 1 kJ/mol ( $\Delta G = 24.3$ - $25.2$  kJ/mol) compared to the case of the pure DPPC. When 1,4-dioxane is found in the system the difference is slightly higher as the peak is at 23.2 kJ/mol. On the other hand, the free energy barrier for water penetration is significantly lower at high oxane concentration ( $\Delta G = 20.8$  kJ/mol). The presence of NSO-HETs also decreases the width of the water penetration barriers. The smallest width is found in the case of phenol (0.16 nm) and 1,4-dioxane (0.14 nm). For oxane (0.54 nm) and morpholine (0.46 nm) this value is rather similar again while it is 0.73 nm for the pure DPPC system.

As previously described, oxane is the only molecule of which position is thermodynamically favorable inside the membrane bilayer. In terms of the density of water molecules in the bilayer center it means, that almost 5 times more water molecules are present in oxane polluted systems compared to all other NSO-HET systems and more than 6 times more compared to clear DPPC membranes.

#### 4.1.5.1 Classical Molecular Dynamics Based Free Energy Calculations (D2E)

If the membrane penetration is not energetically demanding, and the process is well sampled, classical molecular dynamics simulations can also be used for the computation of

free energy profiles (D2E). This mass density-based approach for the calculation of the free energy profile is computationally much less demanding and the results are obtained directly from classical MD simulations which provide consistent free energy profile with the ones from enhanced techniques. As seen in **Figure 30**, the results of the two methods are nearly identical for each investigated NSO-HET molecules; the largest difference is found in the case of the free energy profile of phenol, where the largest deviation is less than 1 kJ/mol, thus it meets the requirements of chemical accuracy.

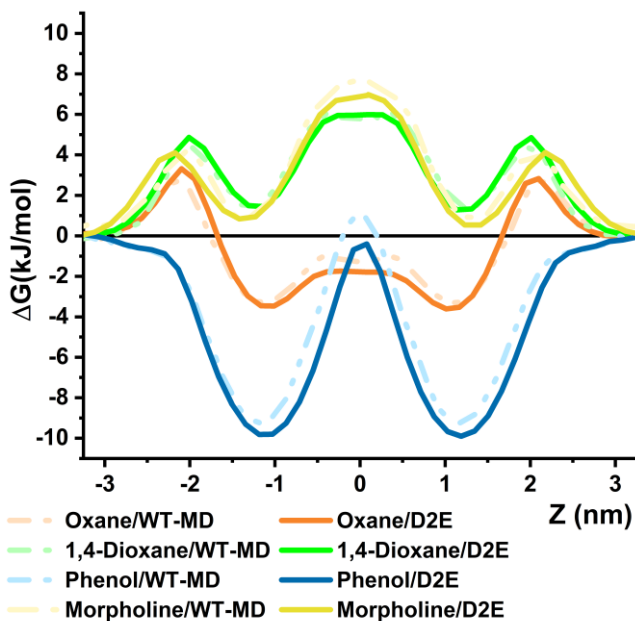


**Figure 30** Comparison of the WT-MD and the MD based free energy calculation (D2E) methods for NSO-HETs (phenol, morpholine, oxane and 1,4-dioxane indicated with blue, yellow, orange, and green, respectively) penetrating inside DPPC membranes. With dashed, pale lines the results of the WT-MD simulations, while with solid lines and colors the results of the MD-based method are shown.

The robustness of the classical MD-based method can be further tested even for the free energy profile of water penetration. As it is seen in **Figure 31** the density-based  $\Delta G$  curves agree well with the results of the WT-MD simulations. The largest differences between the curves are found in the bilayer center in the case of 1,4-dioxane polluted systems, where the largest deviation is around 3 kJ/mol. This can be simply explained by the poorer sampling in the bilayer center, where the concentration of water molecules drop down near zero.

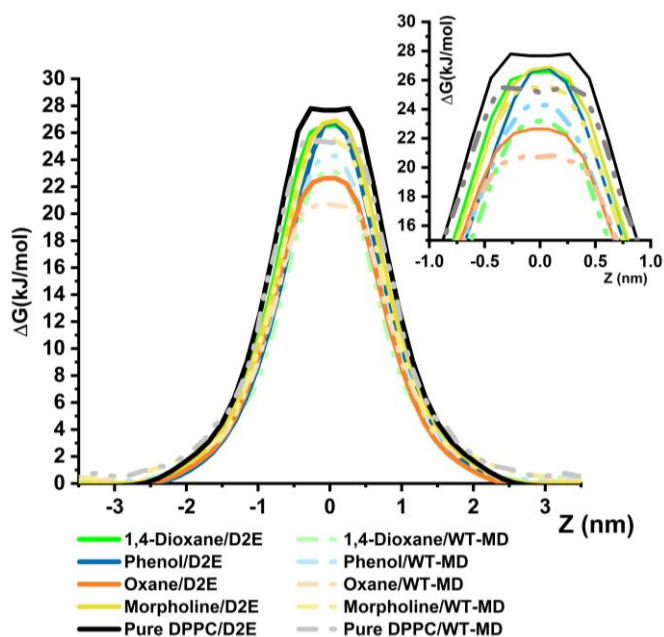


**Figure 31** Comparison of the WT-MD and the classical MD based free energy calculation (D2E) methods for water molecules in the presence of NSO-HETs (phenol, morpholine, oxane, 1,4-dioxane and clear DPPC membranes indicated with blue, yellow, orange, green and black respectively) penetrating inside DPPC membranes. With dashed, pale lines the results of the WT-MD simulations is shown, while with solid lines and colors the results of the MD based method.

The classical MD based approach was also tested whether it works for understanding the concentration dependence of free energy profiles in the case of the two investigated phenol concentrations (**Figure 32**). While in the case of the larger phenol concentration an excellent match is found - the D2E method shows a slightly ( $\sim 1$  kJ/mol) higher free energy barrier in the bilayer center - in the case of the lower concentration the deviation is more significant, and the free energy is lower along the whole profile, by 7-10 kJ/mol. This shows that the sampling of the different regions in the case of a sole phenol molecule is insufficient to represent an equilibrium density distribution.

From these results it is clearly visible, that in some cases the use of enhanced sampling methods is not necessary. If the classical MD simulation is carried out for a sufficiently long time, and the examined molecule is found to be in equilibrium between the different membrane regions than the density profile can provide a quick glance at the free energy of penetration for small, neutral, organic compounds.

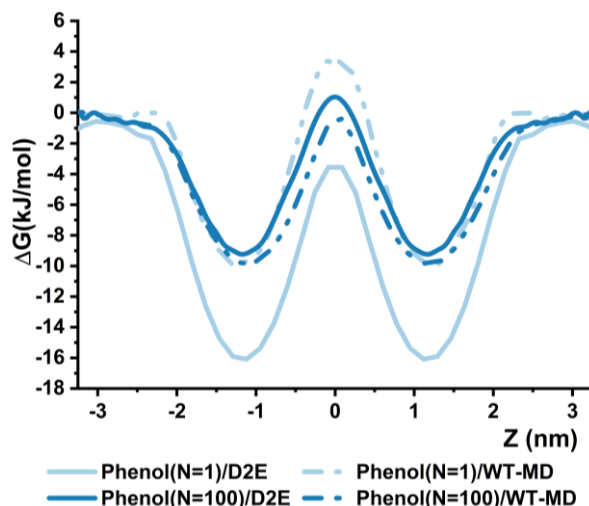


**Figure 32** Comparison of the WT-MD and the MD based free energy calculation (D2E) methods of phenol molecules into DPPC membranes in two different concentrations ( $c_{N=100} = 0.0802 \text{ g/cm}^3$  and at  $c_{N=1} = 0.000802 \text{ g/cm}^3$ , dark blue and light blue respectively). With dashed, pale lines the results of the WT-MD simulations are shown, while with solid lines and colors the results of the D2E method.

However, in the case of non-equilibrium simulations, charged or large molecules, which movement is highly restrained in the vicinity of a cell membrane, or as seen in the case of small concentrations or badly sampled simulations, the classical MD-based approach can lose its accuracy.

#### 4.1.6 Detailed analysis of the effect of 1,4-dioxane on DPPC model membranes

##### 4.1.6.1 Area per Lipid

In the case of 1,4-dioxane further analysis have been carried out. It is worth mentioning that literature APL values are scattered in a large range depending on its indirect measurement and state of the membrane phase. [332] Based on molecular simulations, the average APL can also be derived from different methods. Conventionally, it is calculated from the lateral dimensions of the simulation box divided by the number of lipids in a membrane leaflet, or *via* a Voronoi tessellation (VT) based techniques, as described in **Chapter 2.4.1**.

In the case of 1,4-dioxane both types of APL calculations have been carried out, to compare the results and observe the distribution of this value, which is shown on **Figure 33** and **Figure 34**, respectively.

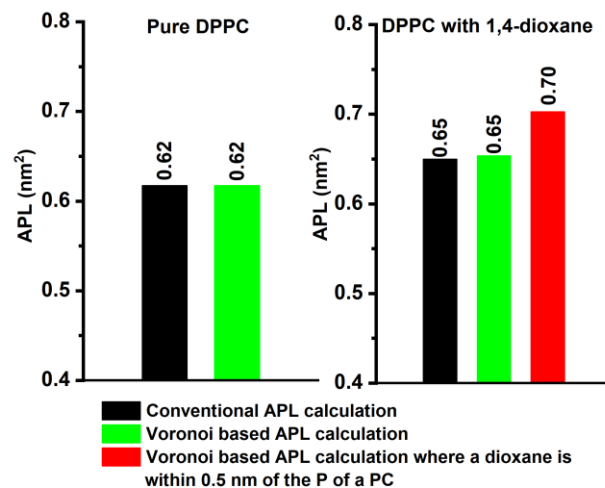


**Figure 33** Average area per lipid (APL) calculated by conventional and Voronoi tessellation-based approaches for DPPC membranes without and with the presence of 1,4-dioxane. Average APL obtained from all phosphorus atoms using conventional (black) and Voronoi tessellation approach (green). APL is also calculated from all phosphorus atoms which have 1,4-dioxane molecules within its 0.5 nm radius (red).

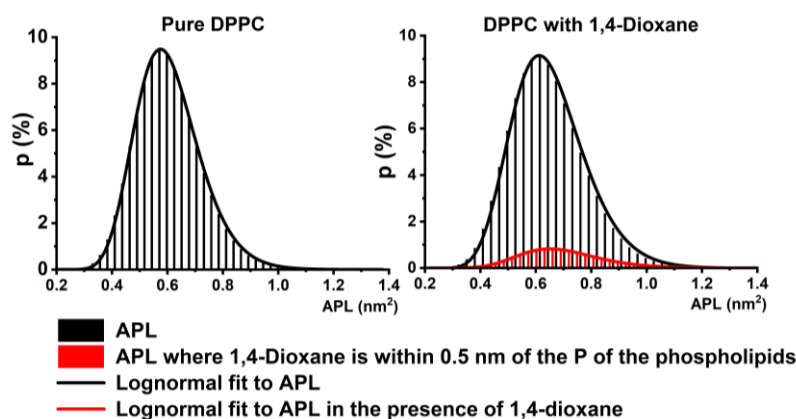


**Figure 34** Probability distributions of area per lipid (APL) obtained by Voronoi tessellation approach. The total APL distribution is shown in black while the local APL distribution of phosphorus atoms which have 1,4-dioxane molecules within its 0.5 nm radius are in red. Lognormal distribution fits are also indicated in the diagrams.

In the case of the pure system, the average APL values obtained from conventional and VT-based approaches match perfectly (first panel of **Figure 33**) and their relative deviation from experiment is only 2% ( $APL_{\text{calc}} = 0.62 \pm 0.14 \text{ nm}^2$ ,  $APL_{\text{exp}} = 0.63 \pm 0.13 \text{ nm}^2$  [59]), basically within its uncertainty.

In the presence of dioxane, the average APL value increased by more than  $0.05 \text{ nm}^2$  for DPPC membranes. To understand the local disturbances caused by 1,4-dioxane molecules, phosphorous atoms which are within 0.5 nm of dioxane molecules are selected from the VT-based APL calculation (see red columns in **Figure 33** and **Figure 34**), where

the probability distributions of the total and local APL values are calculated and shown in **Figure 34**. The average of such local APL values found to be significantly larger than that of the conventional APL (more than 8% growth), namely  $0.70 \text{ nm}^2$  for DPPC membrane which means that the lipid heads are pushed away due to the vicinity of dioxane. It is worth mentioning that the total APL distribution of the pure system is in the range of  $0.30$  and  $1.10 \text{ nm}^2$  while in the presence of the NSO-HET molecule the upper tail of the system reaches over  $1.20 \text{ nm}^2$  (shown in black in **Figure 34**) which can be well described using lognormal distribution. However, assumption of normal distribution and arithmetic mean as expected value results within  $0.02 \text{ nm}^2$  of the expected values of APL obtained from the proper lognormal fit (**Figure 34**) making a reasonable trade-off of APL widely used in the literature. [99], [286], [333] At the same time if the highest probability of APL is calculated (the mode of the APL distribution) the APL is significantly lower:  $0.58 \text{ nm}^2$  for the pure systems and  $0.62 \text{ nm}^2$  in the presence of 1,4-dioxane.

#### **4.1.6.2 Water orientation profiles and the determination of the interfacial regions**

Previous studies proved that based on the orientational order of the water molecules, four different regions can be separated in the membrane interface. [54]–[56] By means of orientational functions, charge densities and water density profiles, we have defined the bulk phase and these four different regions in the interfacial area, which are in line with the Marrink and Berendsen model. [334] Data will only be discussed regarding the negative side of the membrane normal  $Z$ . The definition and calculation of the mentioned orientations and vectors are described in **Chapter 2.4.2**. As the interface normal is fixed to point from the negative side to the positive, and  $\alpha$  can be in the range of  $0^\circ$  and  $180^\circ$ , opposite orientations can be observed on the two sides of the membrane in the case of dipole orientation distribution. If the molecules do not have preferred alignment, then  $\Phi_\alpha(Z)$ ,  $\Phi_\beta(Z)$  and  $\Phi_\gamma(Z)$  are fluctuating around 0. If  $\Phi_\beta(Z)$  is lower than 0, it indicates a more perpendicular, and if  $\Phi_\beta(Z)$  larger than 0, it indicates a more parallel alignment of the normal vector with the membrane surface. For  $\Phi_\gamma(Z)$  the opposite is true, thus if  $\Phi_\gamma(Z)$  is lower than 0, it indicates that the H-H vector can be found in a more parallel alignment with the membrane surface, and if its larger than 0 it is in a more perpendicular alignment with the membrane surface.

**Water orientational density profiles across bilayers**

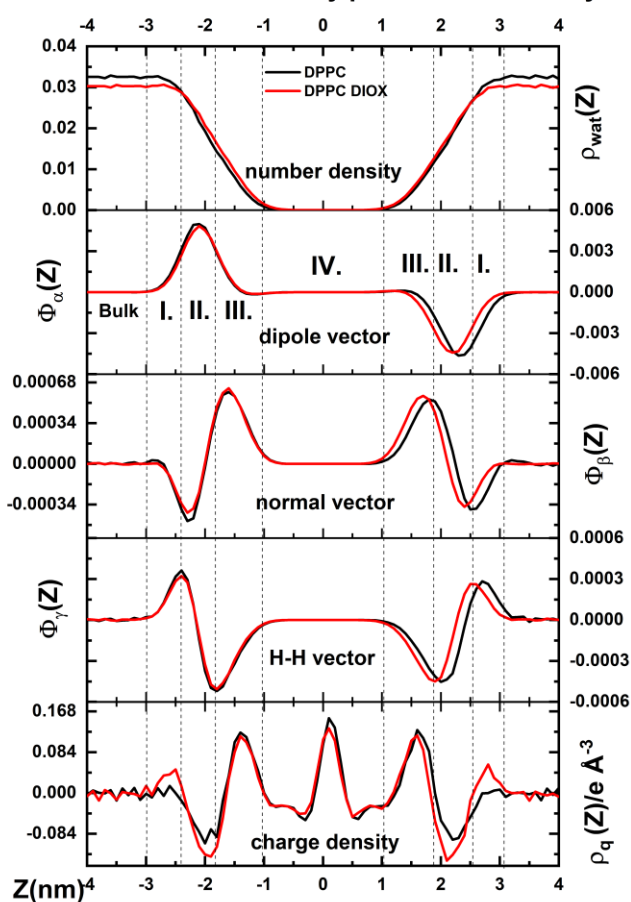


**Figure 35** Number density profiles and orientation functions of water and total charge density profile across the membrane/water interfaces. The  $Z = 0$  corresponds to the center of the membrane. The dashed vertical lines indicate the borders between the regions of the interface. The results for clear DPPC membranes are shown as black solid lines, while red solid lines indicate the membranes in the presence of 1,4-dioxane

The number density, the orientation function of the dipole, normal and H-H vector as well as the charge density profile of water molecules are shown in **Figure 35**. In the bulk phase, all these orientation functions are practically zero which in this case means there is no preferred direction for water molecules. Since the phosphatidylcholine headgroups contain negatively charged phosphate and positively charged tetramethylammonium groups, they determine mainly the orientation of the dipole moments of water molecules as they preferentially turn towards the negatively charged groups. Dipole, normal and H-H vectors are all sensitive to the presence of charged headgroups, therefore their orientation functions can be used for determining the border of the bulk phase (**Figure 35**) thus defining the outer border of Region I. Since the orientation function of H-H vector,  $\Phi_\gamma(Z)$ , is the most responsive to the structural changes, the borders of the Region II are defined by its stationary points, which coincidence with the inflexion points of the orientation function of the dipole

vector  $\Phi_\alpha(Z)$ . Finally, the border between Region III and IV can be given by the coordinate where  $\Phi_\alpha(Z)$  becomes zero again.

In the first interfacial region (noted as Region I), water density started to decrease slowly as seen in the top panel of **Figure 35**.  $\Phi_\beta(Z)$  almost reached a minimum here, while  $\Phi_\alpha(Z)$  showed quick growth, and  $\Phi_\gamma(Z)$  reached a maximum, which was chosen as a border of this region. These changes manifested as the plane of water molecules are more likely to be found in a perpendicular orientation relative to the bilayer. The increase of  $\Phi_\alpha(Z)$  indicates that the dipole moments of water molecules start to point towards the phosphate groups. For the dioxane containing systems, Region I is more positively charged while the clear system showed no charge accumulation here.

In the second region,  $\Phi_\alpha(Z)$  reached a maximum, the orientation function of the normal vector linearly increased while  $\Phi_\gamma(Z)$  decreased as getting closer to the middle of the membrane. This region is negatively charged for each system while this effect is more pronounced for the dioxane containing systems resulting a more polarized outer layer for these membranes. Here, the dipole moment vectors enclose around  $\sim 0^\circ$  with the surface normal, which means that the dipoles are pointing towards the membrane surface.

In the third region, water density vanished slowly and the decrease of  $\Phi_\alpha(Z)$ , as well as the increase of  $\Phi_\gamma(Z)$  to zero, indicate that water molecules are slowly losing their orientation preference. Before the vanish of the orientation preference occurring at the inner part of Region III, the presence of the peak of  $\Phi_\beta(Z)$  indicates that water molecules are taking a more planar alignment due to the presence of the ester groups.

In the central region (Region IV) no preferred orientations for water molecules can be seen based on the orientation profiles most probably due to the low statistical sampling of water molecules.

#### 4.1.6.2.1 1,4-dioxane orientational profiles along the membrane normal

Similar to water, the orientation preference of 1,4-dioxane had been quantitatively described by orientation functions of the O-O ( $\Phi_\alpha(Z)$ ) and normal vector ( $\Phi_\beta(Z)$ ) as a function of the distance from the center of mass of the membrane (**Figure 36**). When  $\Phi_\beta$  is lower than 0, it indicates perpendicular, if larger, parallel alignment of the normal vector of the pollutant molecule with the membrane surface. Orientation function of the O-O vector is centrosymmetric having minima at the border of Region I and II and at about  $Z = -5 \text{ \AA}$  (in Region IV) as well as maximum at  $Z = -15 \text{ \AA}$  (in Region III), while the orientation function of the normal vector is symmetric with a minimum at around  $|Z| = 8 \text{ \AA}$ .

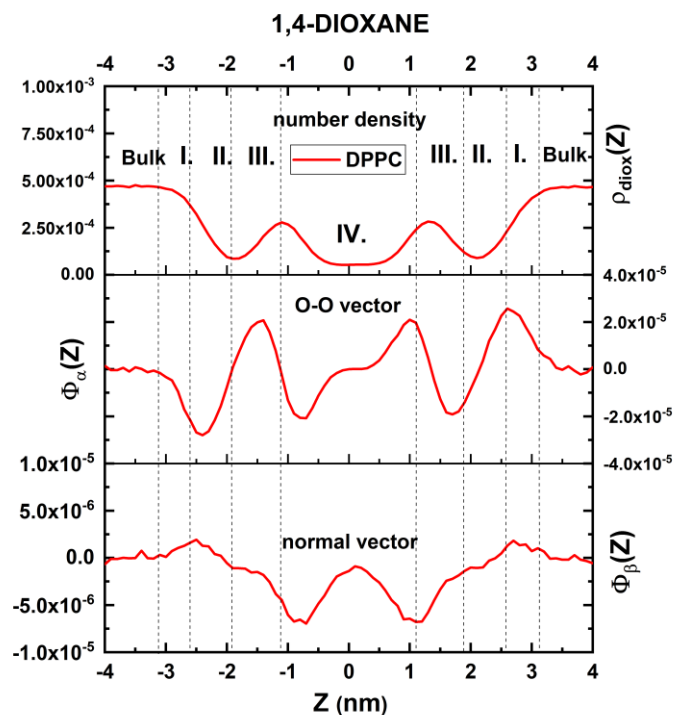


**Figure 36** Orientational profiles of dioxane molecules across the membrane/water interface. The density of dioxane molecules is shown as a reference. The dashed vertical lines indicate the borders between the different regions.

A structural manifestation of these profiles is that random orientations are preferred in the bulk phase, then the molecular planes are in a planar position with the bilayer surface in the first two interfacial regions. The turning of the O-O vector throughout Region III and IV indicates, that while 1,4-dioxanes approach the membrane, the molecules turn around their  $y$  axis, then turn back into a planar position. This turning can also be observed from the direct examination of the trajectories. In the inner side of the ester groups of the bilayer, 1,4-dioxanes can be found more likely in a parallel position with the membrane interface. Between the two types of membranes, no significant differences can be inspected.

#### 4.1.6.2.2 Orientation maps of water and 1,4-dioxane molecules in the membrane interfacial regions

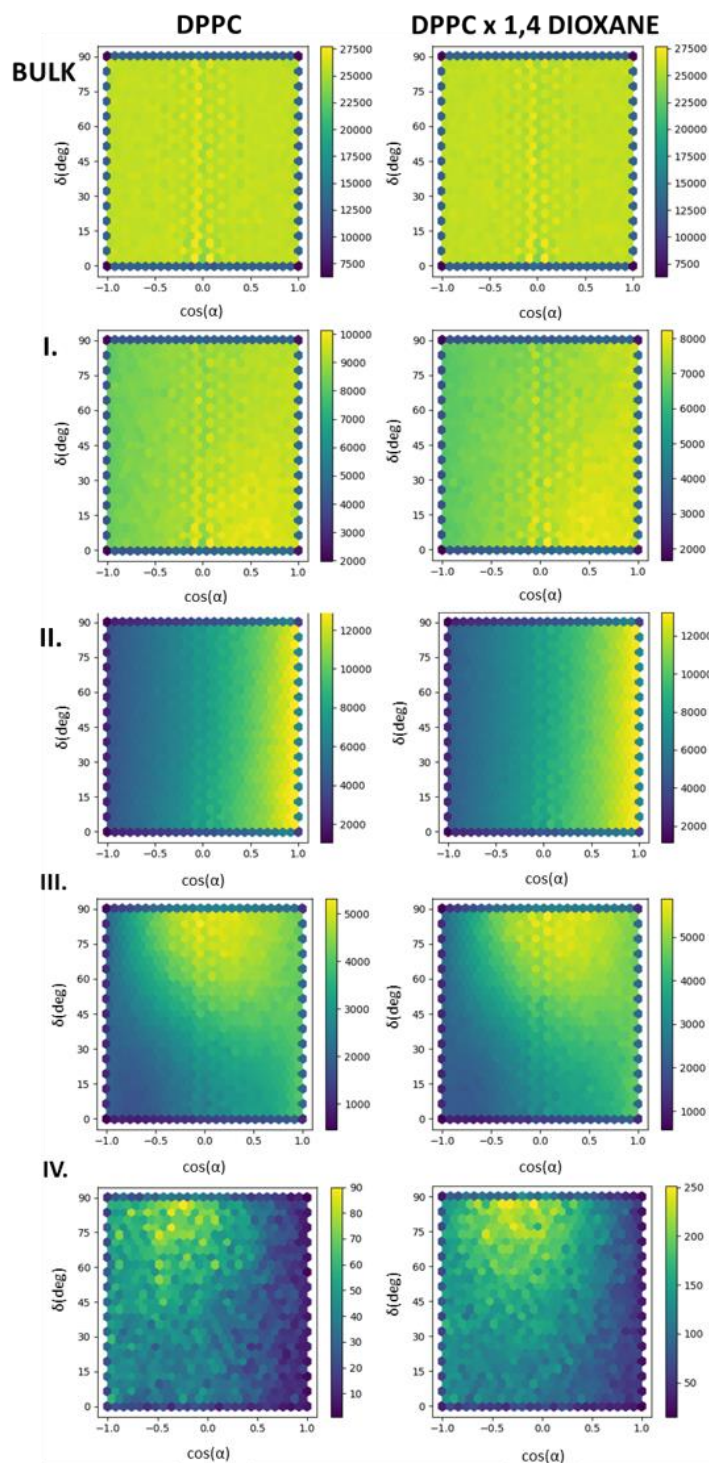


**Figure 37** Orientation distribution maps of water molecules in the DPPC membrane/water interface. While  $\cos(\alpha)$  can be varied from -1 to 1,  $\delta$  is from  $0^\circ$  to  $90^\circ$  due to the symmetry of the water molecule. The color bars indicate the number of water molecules appearing in each region over 500 ns total simulation.

The two independent vectors ( $\alpha$  and  $\delta$ ) of water and 1,4-dioxane molecules can be represented as maps which gives us a clearer view of their orientation preference in the

different regions of the membrane/water interface. In the bulk phase (**Figure 37**), no preferred orientation can be found. In the first region a slight orientation preference can be seen as the water molecules are more likely to be found in the  $0 \leq \cos(\alpha) \leq 1$  region, while  $\delta$  has no effect on the orientations, which means that the dipole moment vectors are starting to point towards the negatively charged headgroups of lipids, while the orientation of the plane of water molecules has no preference. This reference is more pronounced in the second region, but here the dipole orientations ( $0.5 \leq \cos(\alpha) \leq 1$ ) obviously show that the water molecules are in a perpendicular position with the membrane surface still without any  $\delta$  preference.

In the third membrane region, the peak orientation is where the likeliness of perpendicular orientation of the water plane ( $60^\circ \leq \delta \leq 90^\circ$ ) is the highest, while the dipole moment vector is parallel with the bilayer surface ( $-0.5 \leq \cos(\alpha) \leq 0.5$ ). In the central region (Region IV) a distinct peak can be observed in the orientation of water molecules at  $60^\circ \leq \delta \leq 90^\circ$  and  $0.0 \leq \cos(\alpha) \leq -1$ , which indicates a quite similar orientation as in the fourth region, but the dipole vector turns around as the molecules approach the middle of the bilayer.

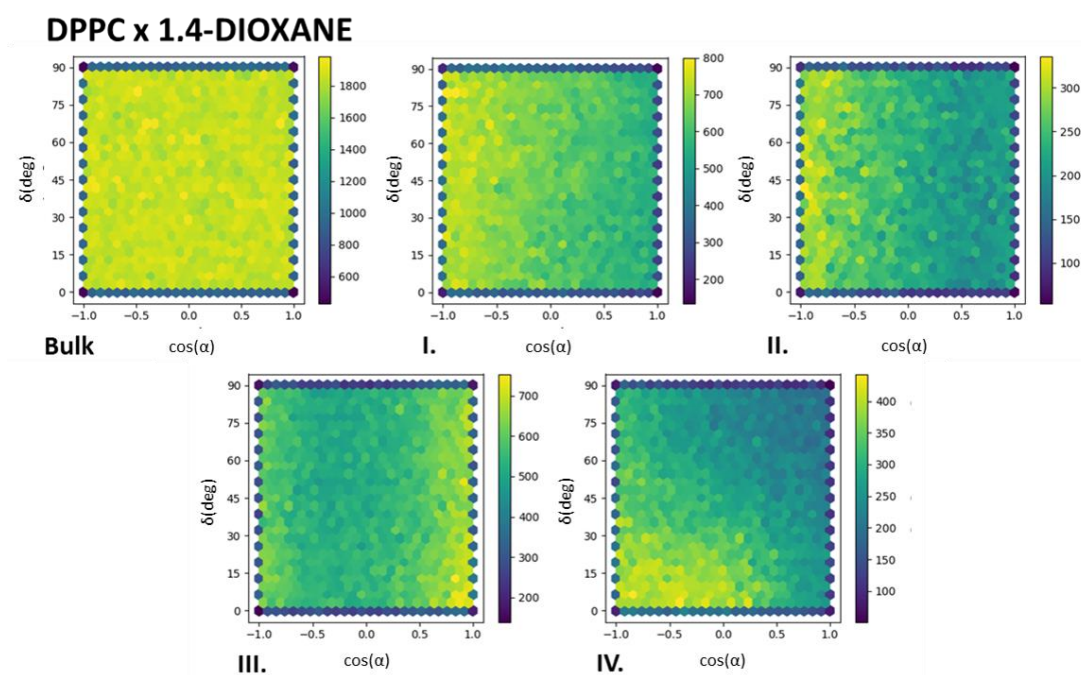


**Figure 38** Orientation distribution maps of 1,4-dioxane molecules in the different regions of the DPPC membrane/water interface. While  $\cos(\alpha)$  can be varied from -1 to 1,  $\delta$  is from  $0^\circ$  to  $90^\circ$  due to the symmetry of the dioxane molecule. The color bars indicate the number of dioxane molecules appearing in each region over 500 ns total simulation.

As **Figure 38** shows, dioxane molecules have random orientations in the bulk phase. In Region I and II, as it was also perceived from the orientation function profiles (see the

middle panel of **Figure 38**), the O-O vectors of the cyclic molecules are parallel with the bilayer surface, but have no preference according to  $\delta$ . Similar is observed in Region III, but after the spin of the dioxane around its axis  $y$ . In the central region (Region IV), the preferred orientation of dioxane molecules is within  $0^\circ \leq \delta \leq 30^\circ$  and  $0 \leq \cos(\alpha) \leq -1.0$ , which means that the O-O vector is enclosing  $90^\circ$ - $45^\circ$  with the bilayer normal, while its normal vector is pointing towards the bilayer inner surface, which means a close to planar position of the pollutant molecule with the bilayer surface.

#### 4.1.7 Summary and Conclusions

The membrane structure and function altering effects of cyclic compounds is an extensively studied topic. In this work the structural effects and the energetics of the penetration processes of four NSO-HET molecules - phenol, oxane, 1,4-dioxane and morpholine - were studied into DPPC membranes. NSO-HET molecules are present in several industrial processes. The presence of heteroatoms makes these compounds more water soluble and mobile compared to their homocyclic analogues, leading to a lasting and easily spreading contamination in industrial sites and also an enhanced risk of contaminated drinking water resources.

It has been found that aside from oxane molecules no other NSO-HETs have a thermodynamically preferred position inside the membrane. As a result, when inspecting the changes in the membrane structural parameters, aside from the APL, all other parameters change the most drastically in the presence of oxane pollution. When pulling the water molecules inside the membrane, it has been found, that oxane affects the free energy of its penetration, by about 4 kJ/mol which results in 5 times more water molecules in the bilayer center compared to the other simulations.

To test the effect of concentration on the thermodynamic process of penetration, simulations with two different phenol concentrations were carried out. When pulling phenol molecules inside the membrane bilayer it has been found that in the presence of higher concentration the main free energy barrier is 3 kJ/mol lower compared to where only one phenol is present. When pulling water molecules in the bilayer, while the height is not changing significantly, the width of the free energy barrier is getting narrower as the concentration of the NSO-HET molecules grow.

The classical molecular dynamics based free energy calculations for the penetration were proved to be accurate within the limits of the chemical accuracy, where the concentration of the cyclic compounds enabled a detailed sampling of the configuration space.

In the case of 1,4-dioxane four regions of the membrane/water interface were distinguished by the orientational functions based on the orientational preference of the local vectors (dipole, H-H and normal vector) bound to the water molecules, which are equivalent to the membrane regions proposed by Marrink and Berendsen. In the interfacial regions (Region I, II, III and IV) starting from about 30 Å from the center of the bilayer, not only water but also dioxane molecules can be found in highly ordered states which have been analyzed via orientational maps. From these maps it can also be understood clearly that dioxane is hydrated throughout its dissolution, as water density also increased in the membrane interior.

## **4.2 EFFECTS OF THE DERIVATIVES OF THE CO<sub>2</sub> AND 1,3-BUTADIENE REACTION ON BIOMEMBRANES**

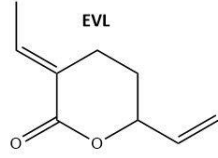
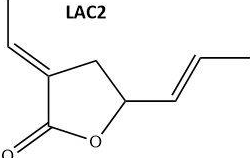
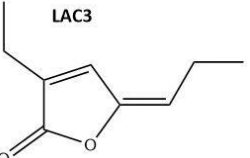
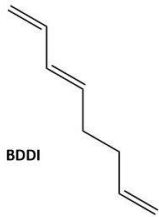
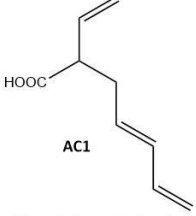
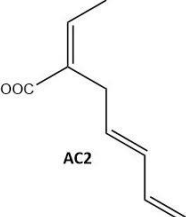
For a greener chemical industry several new potential synthesis routes and products are introduced in every year, however their environmental and health effects are yet to be understood. One of these routes is the telomerisation of CO<sub>2</sub> with 1,3-butadiene. The effects of the derivatives of this chemical reaction is investigated on DPPC model biomembranes. The first step to prevent severe contamination in the environment is to pre-evaluate the possible effects of the appearing chemicals. In the investigated reaction six products have been found experimentally, but the characterization of these product is lacking. The goal of this study was to predict properties of these organic compounds, and to evaluate their possible effect on membrane structure and free energy of penetration.

### **4.2.1 Predicted properties of the studied organic molecules**

As no previous information was found in the case of the products of the mentioned reaction, their densities and hydration free energies (**Table 8**) have been defined.

The densities were obtained by using a Voronoi-tessellation based density calculation method, as described in **Chapter 2.3.1**. The butadiene dimer has the lowest density ( $\rho_{\text{BDDI}} = 752.13 \text{ kg/m}^3$ ), as it is the only compound for which dissolution in water is thermodynamically unfavorable. The lactones have the highest density, which is slightly above the density of water (from  $1004.07 \text{ kg/m}^3$  to  $1042.19 \text{ kg/m}^3$ ) while the organic acids have slightly lower densities ( $\rho_{\text{AC1}} = 980.11 \text{ kg/m}^3$  and  $\rho_{\text{AC2}} = 994.52 \text{ kg/m}^3$ ). Since the acids have a free carboxyl group, their dissolution in water is the most thermodynamically favorable, followed by EVL, LAC2, and LAC3. All lactones have two hydrogen bond acceptors, which facilitates their dissolution in water.

**Table 8** Hydration Free Energies of the investigated species at 323 K; AD means absolute deviation between G3MP2B3 and MD data. The uncertainty of the ab initio based method is between 10.5-17.5 kJ/mol [265]

Species	density in kg/m <sup>3</sup>	$\Delta G_{\text{hyd}}$ in kJ/mol		
		MD	G3MP2B3 SMD	AD
 EVL	1042.19	-22.77±0.05	-29.28	6.51
 LAC2	1031.25	-18.94±0.05	-24.96	6.02
 LAC3	1004.07	-15.81±0.03	-18.18	2.37
 BDDI	752.13	6.54±0.06	2.03	4.51
 AC1	980.11	-29.41±0.24	-31.21	1.8
 AC2	994.52	-32.95±0.52	-36.55	3.6

#### 4.2.2 Structural changes of DPPC membranes induced by the studied molecules

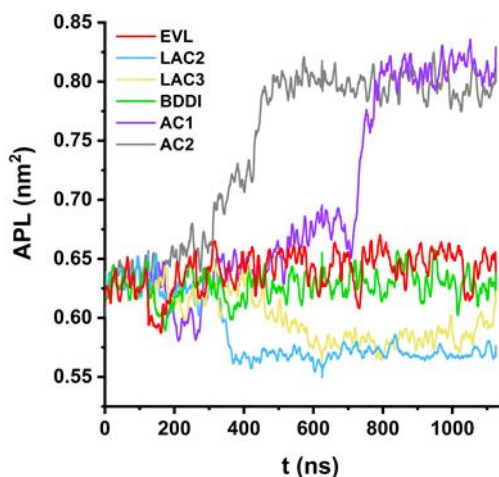


**Figure 39** Evolution of APL of the different membrane systems over the simulation time. APL values were obtained in every 10 ps. The data series were smoothed by using 50% percentiles of the data of every 7.5 ns

The change of APL over the 1100 ns trajectories is shown in **Figure 39**. In this figure, two plateaus are observable for each profile, where the value of APL fluctuates around a constant value. During the first 150 ns of the trajectory, before the permeation of the molecules starts, a “pre-permeation” state was observed, which can be considered as a thermodynamic metastable state. Even though the different systems reach the second plateau over different time intervals, equilibrium was achieved after 800 ns in each case. This final phase can be considered as a thermodynamically stable, “post-permeation” state. The structural differences in the two states are also visible in **Figure 40**.

While EVL only has a slight effect on the APL, LAC2 and LAC3 decrease this value significantly. In the case of LAC2 the change happens after 400 ns of the trajectory, while for LAC3 the change lasts until about 600 ns. On the contrary, AC1 and AC2 gravely raise the average value of APL. The change occurs the last in the case of AC1, after around 800 ns of simulation time.

Based on these results two different states of the system can be distinguished, the “pre-permeation” state, (see snapshots entitled as 100 ns in **Figure 40**) and the equilibrium state, after the permeation of the molecules which was sampled for about the last 200 ns and then analyzed in details. As two significantly different states of the same systems were identified along the trajectories, they can be used to better understand the dynamical evolution of the membrane permeation. The transition period between the two states were excluded from the evaluation. For this reason, the membrane parameters at the beginning (from now on referred to as 100 ns) and at the end (from now on referred to as 1100 ns) were

also compared, where the parameters were obtained from the average over the specified time ranges.

The snapshots of the equilibrated membranes are shown on **Figure 40**. As shown on this figure, the solutes in all systems formed aggregates in the bulk phase, as a large droplet, which occurred within the first 100 ns. Excluding the organic acids, no penetration of the additional molecules was observed after the first 100 ns, which is also visible on the mass density profiles of the solutes (**Figure 42**) The membrane structures seem to be mostly intact, even though in the case of EVL and LAC2 the membrane is found to be in a somewhat swollen state. However, all solutes have induced changes in the membrane properties (**Figure 43**) as seen in the increase of APL and VPL and the decreasing membrane thickness. As SCD values show in (**Figure 44**) the orderliness of the SN1 lipid tails increased in all cases, but for SN2 only the presence of EVL increased the order of the lipid tails.

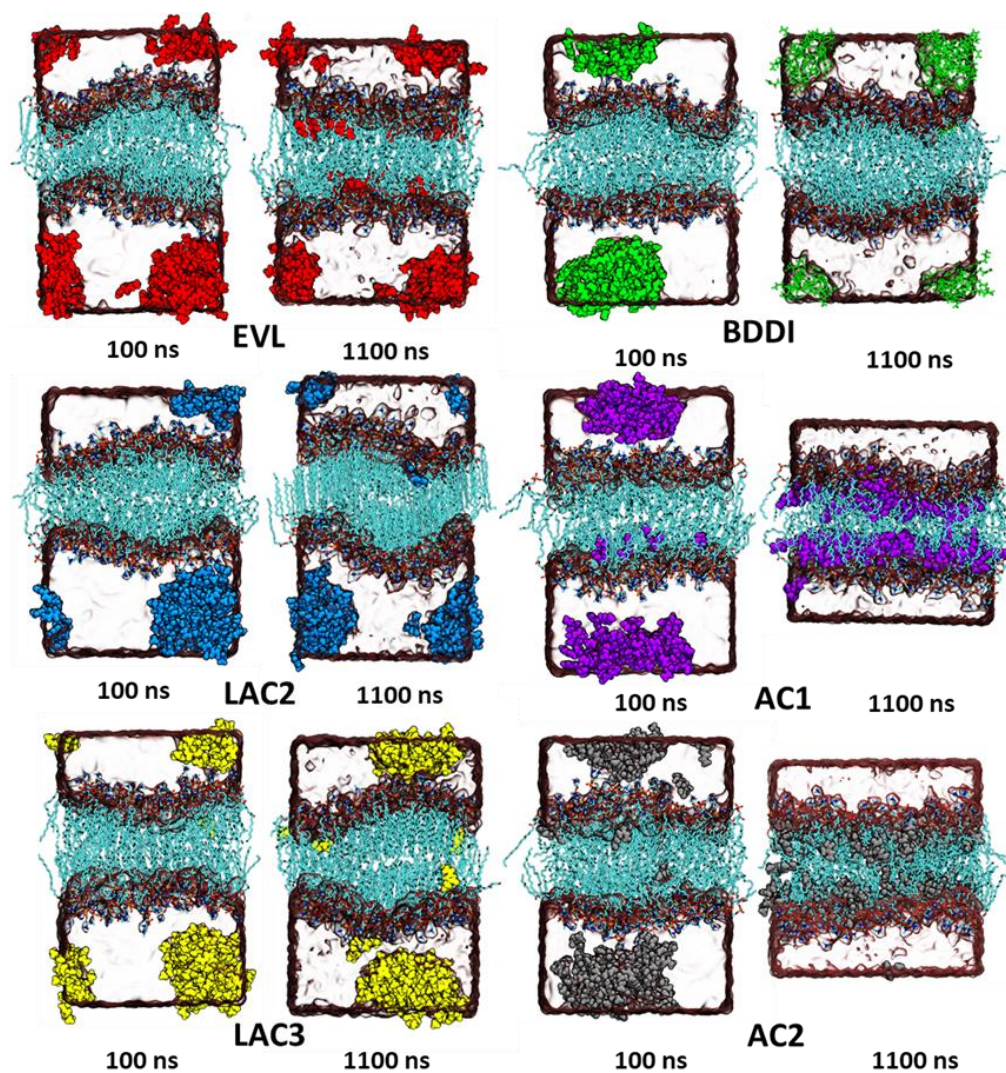


**Figure 40** Snapshots of the simulated systems, after 100 ns and 1100 ns of simulation time.

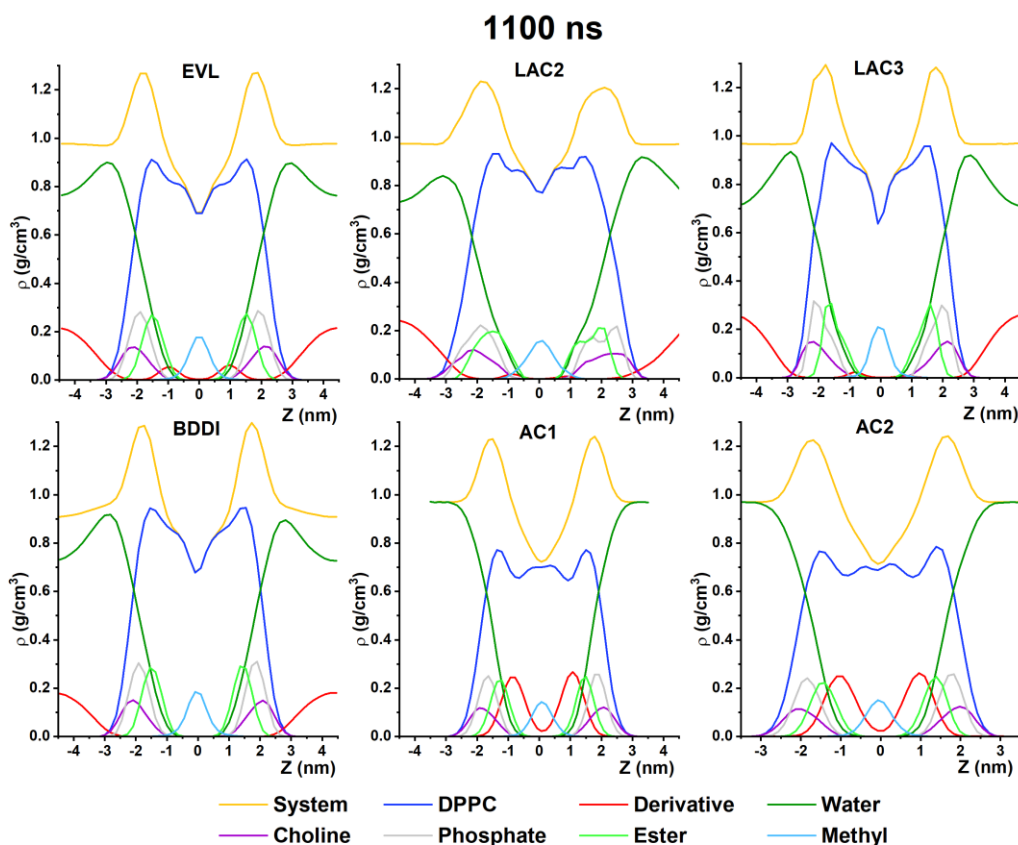


**Figure 41** Mass density profiles of DPPC membranes in the presence of the products of the CO<sub>2</sub> and 1,3-butadiene reaction, EVL, LAC2, LAC3, BDDi, AC1 and AC2 in respective order, based on the average density distribution over 1100 ns simulation. Aside from the densities of the pollutants (red), the membrane (blue) and water molecules (green), subgroups of the DPPC molecules have been selected, namely the choline- (purple), phosphate- (grey), ester- (light green) and methyl-groups (cyan).

Average mass densities of the second investigated state are shown in **Figure 41**, the density profiles of the additives are shown on **Figure 42**, while the snapshots of the final coordinates are shown in **Figure 40**. Over the 1100 ns trajectories - excluding BDDI - a certain amount of the investigated molecules is found inside the membranes. Therefore, the presence of BDDI has almost no effect on the membrane structural parameters. Even though the VPL and  $D_{HH}$  decreases slightly ( $VPL_{BDDI,1100ns} = 1.090 \text{ nm}^3$ ,  $D_{HH,BDDI,1100ns} = 3.452 \text{ nm}$ ) compared to those observed in the initial DPPC membranes ( $VPL_{DPPC} = 1.214 \text{ nm}^3$ ,  $D_{HH,DPPC} = 3.728 \text{ nm}$ ), the membrane structure still appears intact.

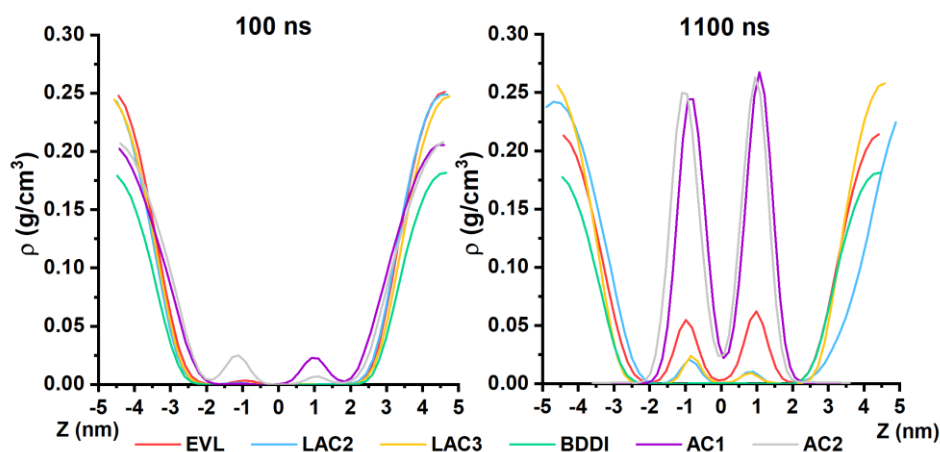


**Figure 42** Mass density profiles of the solutes along the membrane normal of DPPC membranes. The left panel shows the average mass densities computed from 100 ns long production runs, while the data on right panel is computed from 1100 ns simulation.

In the cases of AC1 and AC2, almost all molecules are found inside the membrane bilayer, which is also visible in the density distributions of the compounds as shown in **Figure 42**, (center and right of the bottom). The penetration of the compounds induces critical changes in the membrane structure; as the acyl chains transform into a less ordered conformation, the APL and VPL increase significantly, while the membrane thickness decreases. This process shows resemblance to the previously investigated cases of 1,4-dioxane, oxane, phenol and morpholine in **Chapter 4.1**.

In the case of EVL, the membrane structure undergoes slight structural changes. Since only a small amount of the compound enters the bilayer over the whole trajectory, the APL only increases slightly ( $APL_{EVL,1100} = 0.65 \text{ nm}^2$ ) – compared to that at both the 100 ns state ( $APL_{EVL,100} = 0.62 \text{ nm}^2$ ) and in that observed in the pure DPPC membranes. At the same time VPL and  $D_{HH}$  increases slightly compared to the 100 ns states, while the lipid chains become more ordered. However, the presence of LAC2 and LAC3 visibly disturb the membrane structures. As seen in **Figure 41**, the distribution of the ester- and phosphate-groups becomes irregular, while the order of the lipid tails increases significantly, especially in the case of LAC2. Based on these, the opposite process takes place, as in the case of the acidic components (AC1 and AC2); as the lipid order increases their relative length increases, which increases the membrane thickness, while the APL and VPL decrease.

As the structure of membranes drastically change, it is possible that the presence of EVL and LAC2 induces a phase transition from the  $L_\alpha$  phase to the ripple phase ( $P_\beta$ ), as it was previously observed in involving other compounds. [335]–[338] However, the

simulations were not designed to investigate phase changes, therefore, this parameter is beyond the scope of this study.

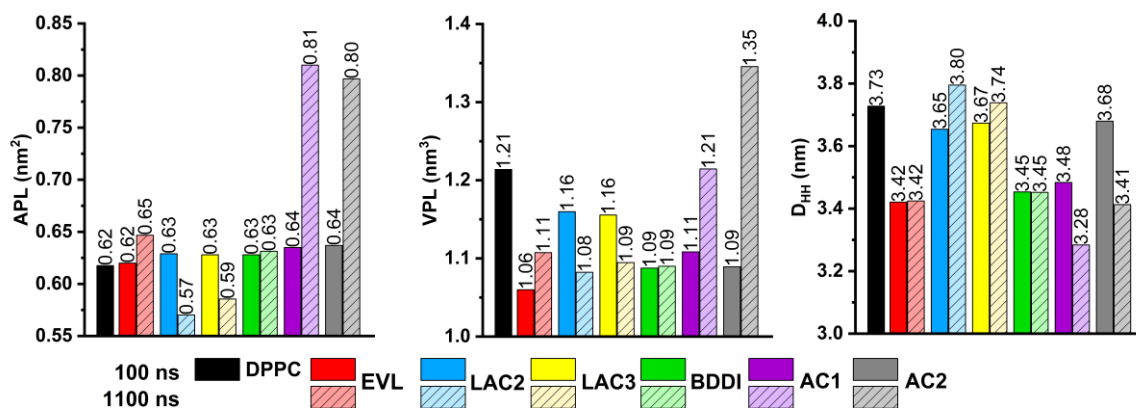


**Figure 43** Membrane properties of DPPC membranes in the presence of the products of the 1,3-butadiene, CO<sub>2</sub> reaction. Solid colors indicate results of 100 ns simulations coming from parallel runs, while striped columns represent one time 1100 ns long simulations.

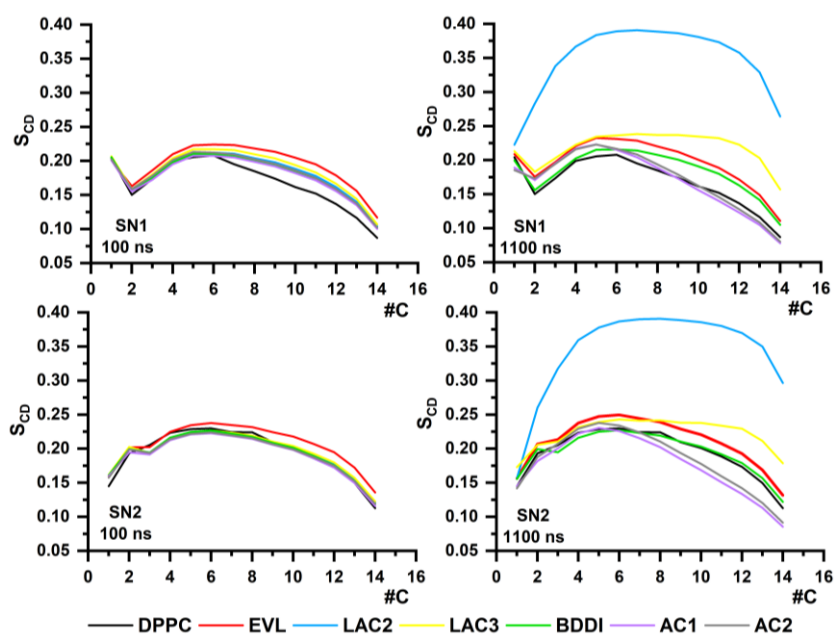


**Figure 44** Deuterium order parameters after 100 ns and 1100 ns simulation.

By using **Eq. 47** the membrane-bulk phase partition coefficients of the compounds were calculated. In this study the obtained  $\log P_{\text{mem/bulk}}$  results are compared with the predicted  $\log K_{\text{ow}}$  data in **Table 9**, since there is no measured value available. In this case even the trends of these partition coefficients does not match. In this case even the trends of these partition coefficients do not match. This can suggest that the hereby obtained results are more appropriate for the estimation of passive membrane permeation, which is an improvement over the predicted values.

**Table 9** Comparison of the calculated  $\log P_{\text{mem/bulk}}$  and estimated  $\log K_{\text{OW}}$  values of the derivatives of the 1,3-butadiene-CO<sub>2</sub> reaction

Name	EVL		LAC2		LAC3		BDDI		AC1		AC2
$\log K_{\text{OW}}$	1.601 [196]	2.456 [195]	1.710 [196]	2.398 [195]	1.990 [196]	2.554 [195]	3.180 [196]	3.050 [195]	1.960 [196]	2.273 [195]	2.427 [195]
$\log P_{\text{mem/bulk}}$	-0.45		-1.28		-1.23		-2.56		1.20		1.50

### 4.2.3 Free energy profiles of the studied organic compounds

Free energy profiles of the compounds were obtained by both WT-MD and the density-based approach for the more concentrated systems. As the behavior and structure of LAC2 and LAC3, and AC1 and AC2 was found to be so similar, only AC1 and EVL was investigated along with EVL and BDDI by using WT-MD. Both the WT-MD and D2E-based results were averaged for the two sides of the bilayer, resulting in symmetric free energy profiles.

The density-based approach is proven to be an accurate method again, as the shape of the profiles are alike, and in almost all cases (except for LAC2) the profiles are within the limits of chemical accuracy. In the case of LAC2 a larger difference is observable at the bilayer interior ( $|Z| = 2-1.5$  nm), as the density-based free energy profile is significantly lower (5.34 kJ/mol), than the WT-MD based one. This can be explained by the small number of penetration events that occurred in the classical MD simulations; if the simulations were further extended to enable more penetrations to be observed, the profile would presumably be closer to the one obtained by WT-MD.

Out of the investigated molecules only the organic acids were able to penetrate the membrane in larger amounts. As shown on the free energy profile of AC1 in **Figure 45**, their most preferred position is within 1 nm of the bilayer center, while the bulk phase and the bilayer center are less preferred. Out of the lactones, the main product of the butadiene + CO<sub>2</sub> reaction, EVL had the highest density in the bilayer interior ( $\langle \rho_{LAC1} \rangle = 74.57 \text{ kg/m}^3$ ,  $\langle \rho_{LAC2} \rangle = 15.70 \text{ kg/m}^3$ ). This is also supported by their free energy profiles, as LAC2 has a higher free energy barrier when penetrating the headgroup region by ~15 kJ/mol and at the bilayer center by almost 10 kJ/mol.

BDDI was basically unable to penetrate the bilayer in the higher concentration systems ( $C_{\text{BDDI}} = 115.67 \text{ g/dm}^3$ ), which is explained by a 31.26 kJ/mol free energy barrier in the region of the phospholipid headgroups. It is also less preferred for the compound to be located at the bilayer center compared to the bulk phase, where the droplet of the further

BDDI molecules are located. In this case no barrier to reaching the bilayer center is observed due to the hydroapaticity of this molecule.

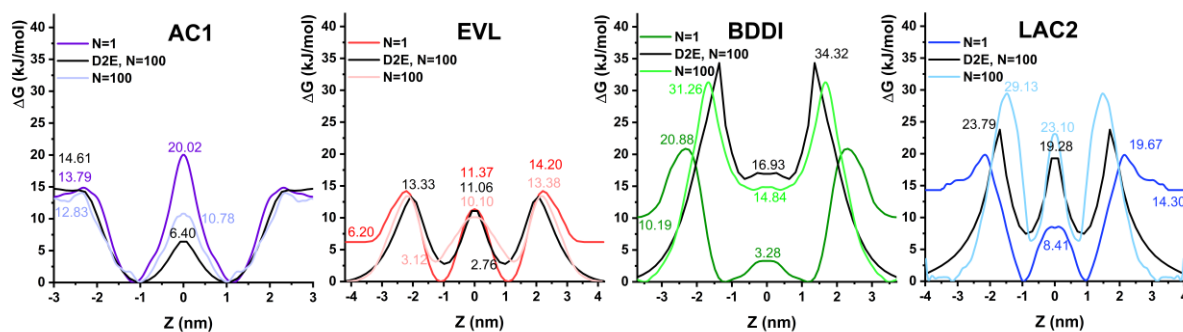


**Figure 45** Free energy profiles of the investigated compounds obtained by WT-MD in two concentrations (N=1, where one compound and N=100 where 100 molecules of the same species are present in the vicinity of the membrane system) and the density based method (D2E), which is obtained from the classical MD simulations.

In the case of all investigated molecules a concentration dependence of the penetration is observable. As AC1 has the lowest water solubility, its relative free energy does not change by the concentration, but the permeability barrier of the bilayer center is 10 kJ/mol lower in the case of the highly concentrated system. In all the other cases a droplet was formed in the bulk phase for the simulations at a higher concentration (N = 100). This makes the bulk phase the preferred position of the molecules even if in the diluted cases a hydroapatic behavior is shown. This phenomenon is most apparent in the cases of the butadiene dimer (BDDI) and LAC2, as at both the site of the headgroups and at the bilayer center the free energy barrier decreases by over 10 kJ/mol. The smallest concentration dependence of the free energy profile is found in the case of EVL, where aside from the bulk phase no relevant difference is seen. The further biological effects and metabolism of EVL is necessary to be investigated due to the low energy barrier for passive penetration of EVL through biomembranes before its intensive use.

By inspecting the free energy profiles of the diluted systems, two different behaviors of the molecules are observable: in the case of AC1, the permeation of the molecules into the bilayer is barrier-free, while in the other cases a free energy barrier inhibits the dissolution of the molecules into the bilayer. The barrier-free free energy profile is also observed in the cases of aspirin, diclofenac, ibuprofen [339] and melatonin [340] , and all data was obtained by using WT-MD. While the mentioned molecules contain rings that may be more structurally similar to the lactones, aspirin, diclofenac and ibuprofen are also carboxylic acids, which induces a similarly shaped free energy of permeation profile as the hereby investigated acids. In the case of melatonin most likely the dimensions and the

placement of its functional groups lead to the similar shape of the profiles. The barrier inhibited profiles resemble the free energy graphs of butyl nicotinate, 2-butoxyethanol or diethylcarbamazine, all of which were obtained by COSMOmic15 on DMPC membranes. [341]

#### **4.2.4 Summary and Conclusions**

In this work the interactions between different products of the reaction of CO<sub>2</sub> and 1,3-butadiene on model biomembranes comprised of DPPC molecules were investigated by using OPLS-AA force field. MD simulations in the presence of 100 molecules of the same species were carried out for 1100 ns. Over this time interval two different states of the systems were found, one for the first 100 ns, and a second for the final 200 ns.

For all the investigated compounds their pure liquid densities and hydration free energies have been determined for the first time. It was found, that the butadiene dimer has the lowest density and highest hydration free energy.

In the concentrated systems, aside from BDDI, all compounds can penetrate biomembranes, out of which the two acids prefer the membrane interior to the bulk phase. All the other compounds formed droplets in the bulk phase. Even though BDDI does not penetrate the bilayer, all of the investigated compounds disturbed the membrane structure. The largest disturbance occurs in the presence of LAC2, where the membrane structure resembled the ripple phase of the second stable membrane conformation.

By using WT-MD the free energy of permeation profiles of four of the compounds were calculated, and it was found that LAC2 and BDDI have the highest permeation barriers, with the only difference being that the butadiene dimer can move freely within the central region of the bilayer. In all the investigated cases the penetration profiles show concentration dependence, especially where droplet formation took place, which makes the bulk phase a preferred position for the permeants. In general, it can be said, that at higher concentrations the free energy barriers are lower than in the case of the diluted systems. The density-based (D2E) free energy calculations were within chemical accuracy of those determined with the WT-MD simulations, except in the case of LAC2. In the case of LAC2 the limit of chemical accuracy was surpassed by about 1 kJ/mol, leading to a total of 5.34 kJ/mol difference between the two profiles. All of this suggests that D2E is a usable method for a quick estimation of the permeation profiles.

### 4.3 CONCLUSIONS OF MEMBRANE PERMEATION STUDIES

On **Figure 46** the free energy profiles and the  $\log P_{\text{mem/bulk}}$  values of all the investigated compounds, where  $N_{\text{compound}}=100$ , are shown. When inspecting the free energy of permeation profiles, three different types occur based on the amount of free energy barriers during the permeation process. In the cases of AC1 and PHE only one free energy barrier is found in the bilayer center, which restrains the free movement of the additives. At the same time these molecules permeate inside the bilayer spontaneously. In the cases of BDDI and oxane two permeation limiting barriers are found in the position of the headgroups, while these molecules diffuse freely in the bilayer center. Three free energy barriers are found in the cases of EVL, 1,4-dioxane, morpholine and LAC2, which are located both at the position of the headgroups and in the bilayer center.

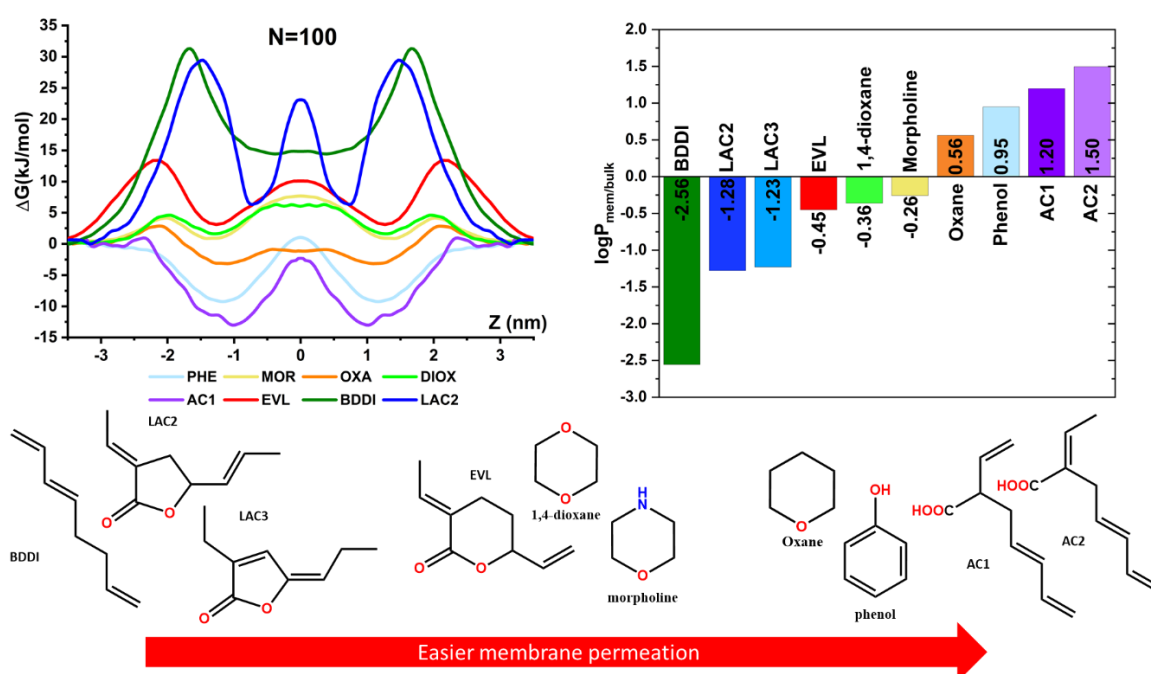


**Figure 46** Comparison of free energy profiles and  $\log P_{\text{mem/bulk}}$  values of the investigated molecules, where  $N_{\text{compound}}=100$ . Based on these data a permeation order of the molecules is set, which is indicated by the 2D graph models of the compounds.

Based on the free energy profiles and the partition coefficients three different types of molecules can be separated from the investigated species, with which a permeation order can be set up. BDDI, LAC2 and LAC3 have the lowest  $\log P_{\text{mem/bulk}}$  values (under -1) and the highest barriers of permeation. Even though LAC2 and 3 have similar functional groups as EVL, a probable explanation for this phenomena can be the longer alkene chain on the cyclic base of the molecules which prevents the compounds from penetrating the phospholipid headgroups. The butadiene dimer is the only investigated species without any electron acceptors or donors, which prevents it to form any favorable interactions with the

phospholipid headgroups, but for the same reasons it is the only molecule which does not have a free energy barrier in the bilayer center.

The partition coefficients of the second group have an intermediate value, but it's still below 0. This group consists of EVL, 1,4-dioxane and morpholine. In the cases of these molecules two electron acceptors are found, which helps to establish secondary bonds with the headgroups, making the first permeation barrier lower. At the same time in the bilayer center these functional groups prevent the molecules from establishing strong interactions with the lipid tails, creating a second permeation barrier in the bilayer center. While the partition coefficient of dioxane and EVL are very close, the difference between their free energy profiles is remarkable, which can be caused by the significant size difference of the two molecules. This can serve as an explanation for the relevantly longer simulation time needed for reaching an equilibrium structure during the simulation of EVL.

In the final group those molecules are found which have a positive partition coefficient, such as oxane, phenol, AC1 and AC2, which means that the membrane permeation of these compounds is spontaneous. A sole permeation barrier is found in these cases in the bilayer center, where the penetration is blocked due to the various functional groups of the solutes.

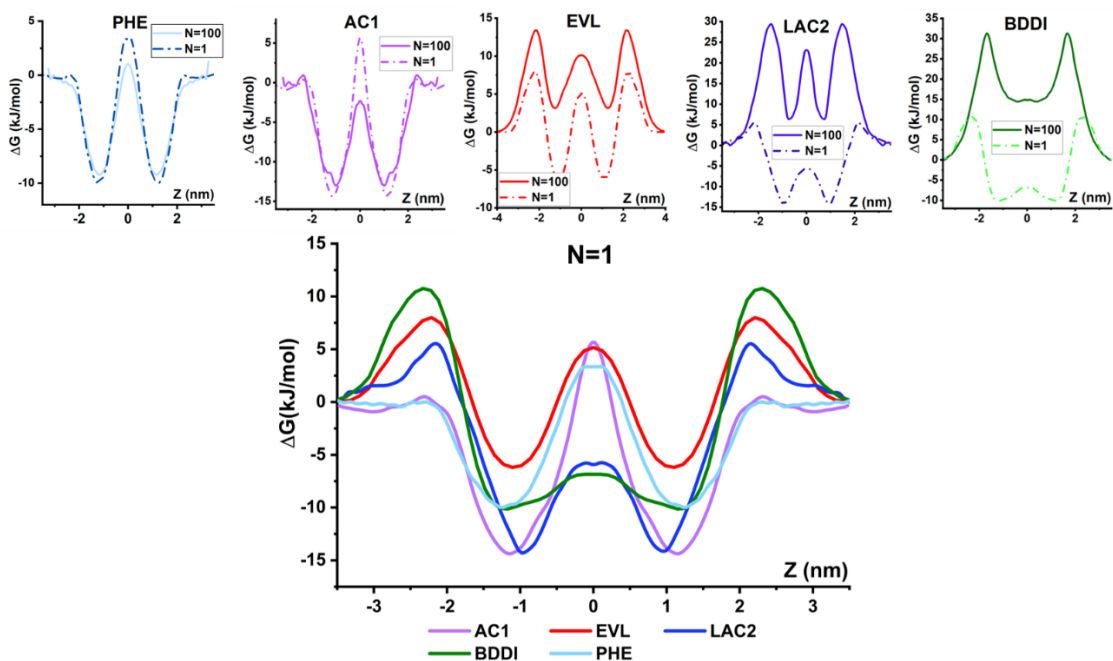


**Figure 47** Comparison of the free energy profiles where  $N_{\text{compound}} = 1$ . On the upper panels the comparison of  $N_{\text{compound}} = 1$  and  $N_{\text{compound}} = 100$  is shown.

As described in the previous chapters, several molecules form droplets in the bulk phase when the concentration is high due to their limited solubility, which makes the bulk phase the thermodynamically preferred state in these cases, and extra energy is required to exit this favorable supramolecular configuration. To remove this factor, the membrane permeation of

the compounds in an infinite dilution ( $N_{\text{compound}} = 1$ ) was also investigated in five cases as shown in **Figure 47**. At the same time the membrane-bulk partition coefficient in these cases cannot be calculated accurately due to the low amount of membrane permeation events and the D2E method is not usable.

The smallest change in the free energy profiles are found in the cases, where the membrane permeation was found to be a spontaneous event at higher concentrations (AC1 and phenol), as these molecules are soluble in water in the used concentration. At the same time the number of favorable interactions between the species and the bilayer did not change. More relevant differences are visible in the cases of BDDI, EVL and LAC2. All of these molecules formed droplets at higher concentration, which shows that their water solubility is limited. In these cases the permeation barrier into the bilayer is significantly reduced, and the thermodynamically favorable location becomes the inner site of the headgroups, where the ester groups of phospholipids are found, where they can form secondary interactions.

Based on Mullins's theory the volume fraction ( $V/V_{\text{compound}}$ ) of the 10 compounds at the higher investigated concentrations were calculated in order to be able to select the possible narcotics by using the following equation,

$$V/V_{\text{compound}} = \frac{\sum_{-D_{HH}/2}^{+D_{HH}/2} N_{\text{compound}} V_{\text{compound}}}{V_{\text{membrane}}} \quad \text{Eq. 48}$$

where  $N_{\text{compound}}$  is the number of compounds in a small segment of the simulation box obtained from their number density along the membrane normal by using the gmx density module of GROMACS [79],  $V_{\text{compound}}$  is the estimated volume of a given molecule calculated from the molar mass and the density of a species, and  $V_{\text{membrane}}$  is the membrane volume obtained by the multiplication of the membrane thickness and the lateral dimensions of the simulation box.

The obtained volume fractions of all the compounds are collected in **Figure 48**, and the limit for narcotics from Mullins's volume fraction theory is indicated. Based on our findings aside from BDDI all molecules have potential to disturb the membrane functions via narcosis. While the same groups exist just as in the case of the membrane permeation, the order of the molecules are swapped. BDDI is the only molecules which do not act as a narcotic in these model systems at the investigated concentrations, due to its high free energy barrier of permeation and a low  $\log P_{\text{mem/bulk}}$  value. BDDI is followed by LAC2 and LAC3, which have the lowest narcotic potential out of the In the second group the order of molecules are swapped, as EVL occupies the largest volume fraction of the membrane due to its size.

The compounds in the final group occupy over 0.1 volume fraction of the membrane, out of which AC1 and AC2 occupy almost half of the volume of the bilayer.

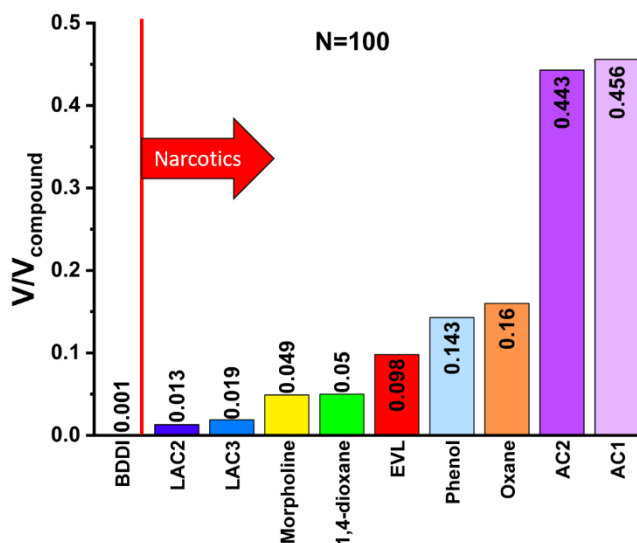


**Figure 48** Volume fraction of the investigated compounds where N=100 additives are present in the simulation box.

Based on all these findings it is important to note that all of the investigated parameters are highly dependent of the concentration of the solute molecules in the vicinity of the membrane system. By using infinite dilution aside from the free energy profiles other parameters cannot be computed due to the lack of permeation events. At the same time at a given concentration the potential narcotic molecules can be selected based on Mullins's volume fraction theory, and a permeation order of the molecules can be set. In this work it was shown that these molecules can permeate inside biomembranes, and extensive investigation is needed to understand their cellular activity before their extensive use in industrial processes.

## 4.4 VAPOR LIQUID EQUILIBRIUM AND SUPERCRITICAL PHASE OF 1,3-BUTADIENE

In industrial production reaction optimization can help to reduce the amount of unnecessary chemicals, which also can be supported by using MD simulations. The goal of this study was to optimize a simulation protocol for investigating the VLE and supercritical phase of an industrially relevant compound, 1,3-butadiene, and to map molecular details which could be of further help in industrial processes.

### 4.4.1 VLE and critical parameters of 1,3-butadiene

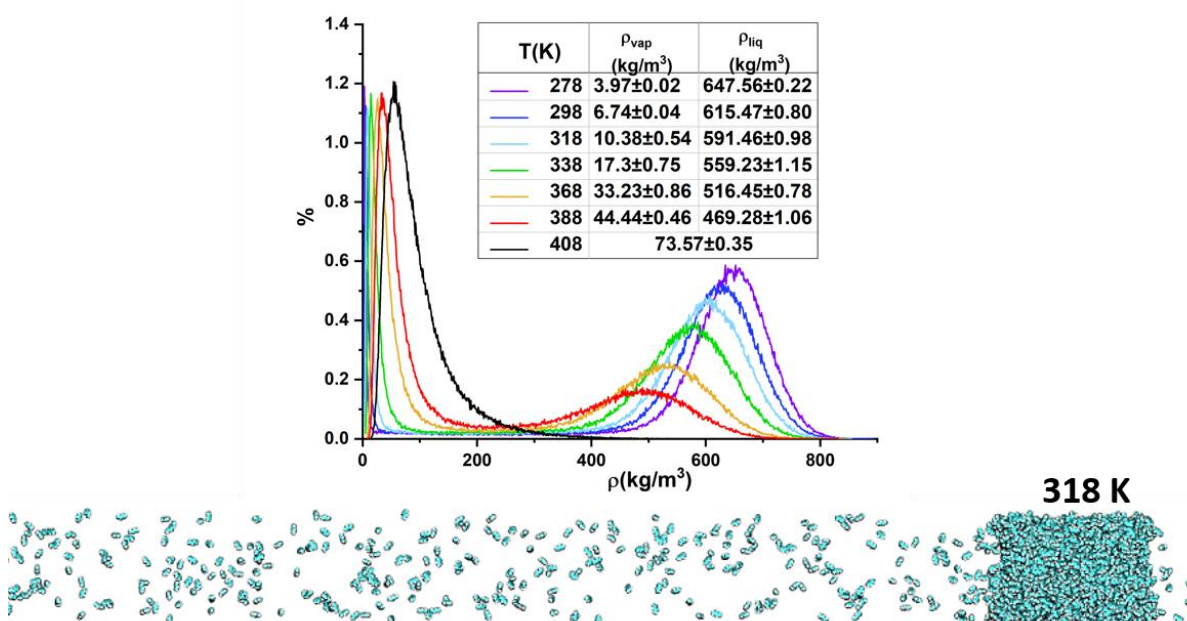


**Figure 49** Density distributions and average densities of liquid and vapor phases calculated by normal and lognormal fits respectively obtained from 2 $\phi$ MD simulations between 278 and 408 K, and a snapshot from the equilibrated VLE of 1,3-butadiene at 318 K.

The Voronoi Tessellation based density distributions of the (2 $\phi$ ) slab simulations are shown in **Figure 49**. The density analysis of each temperature from simulations has been carried out for the last 10 ns of the equilibrated trajectories. From the obtained density distributions the average gas phase and liquid phase densities have been obtained by fitting a lognormal and normal function respectively (**Figure 49**). At lower temperatures the distribution of both liquid and vapor phase densities can be found in a narrow density region, well separated from each other, where the majority of the molecules are in liquid phase. As temperature rises the two density regions become wider, the peaks get closer to each other, and in the SCF region the two phases merge together providing a unified density distribution at 408 K.

#### 4.4.2 Density based calculation of the critical temperature and density

The average liquid densities ( $\rho_l$ ) and vapor densities ( $\rho_v$ ) are depicted as a function of temperature in **Figure 50**. As seen from this vapor-liquid equilibrium (VLE) curve, the results obtained from the 2 $\phi$  simulations are in agreement with the experimental values [326] at every temperature within 5 kg/m<sup>3</sup>.

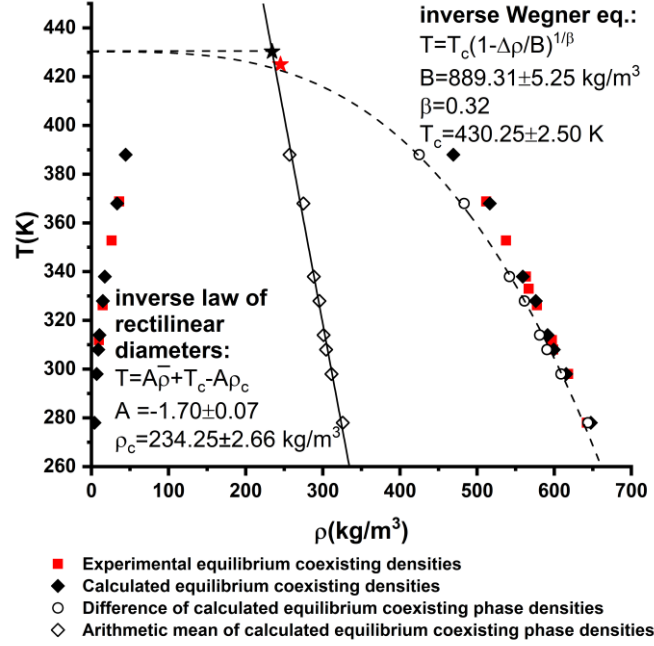


**Figure 50** Equilibrium coexisting densities obtained from 2 $\phi$ MD and experiment, shown with black diamonds and red squares, respectively. The difference and arithmetic mean of the calculated values are also indicated with open diamonds and circles respectively, while the fitted functions (inverse of the law of rectilinear diameters and Wegner equation for representation purposes) are shown with solid and dashed lines (which is further projected to the critical point). The experimental ( $T_{c,\text{exp}} = 425 \text{ K}$  and  $\rho_{c,\text{exp}} = 245 \text{ kg/m}^3$ ) and the calculated ( $T_{c,p} = 430.25 \pm 2.50 \text{ K}$  and  $\rho_{c,p} = 234.25 \pm 2.66 \text{ kg/m}^3$ ) critical points are shown with red and black stars. All experimental data have been taken from the Dortmund Databank [326]

The critical temperature and density of 1,3-butadiene were determined by fitting the subcritical vapor and liquid densities to the first term of the Wegner expansion [218], [342]–[345],

$$\rho_{liq} - \rho_{vap} = B \left(1 - \frac{T}{T_c}\right)^\beta \quad \text{Eq. 49}$$

and to the law of rectilinear diameters [346], [218], [344]:

$$\frac{1}{2}(\rho_{liq} + \rho_{vap}) = \rho_c + A(T_c - T) \quad \text{Eq. 50}$$

In **Equations 48** and **49**,  $\rho_{liq}$  and  $\rho_{vap}$  stand for the densities of the liquid and vapor phases respectively, while  $\rho_c$  and  $T_c$  are the critical pressure and temperature, respectively.  $A$  and  $B$  are adjustable parameters of the equations, while  $\beta$  is the critical exponent for the order

parameter of  $\rho_{liq} - \rho_{vap}$ . The value of the critical exponent is experimentally reported between 0.315 and 0.34 in general [347]. In this study we have used  $\beta = 0.32$ , which have been used in previous simulation studies to obtain the VLE curve. [218], [348] The fitted curves and values of the parameters of **Eq. 49** and **50** are shown on **Figure 50**, where the inverse of the functions had to be used for representative purposes, which made no difference in the obtained critical properties. All fittings have been iterated using OriginPro 2018 [349] applying orthogonal distance regression [350] algorithm.

The critical pressure was determined by fitting the Clausius-Clapeyron equation (**Eq. 51**) to the  $P_0$  vs.  $T$  data, and extrapolated to  $T_c$ .

$$P_0 = e^{\frac{H_v}{RT} + c} \text{ bar} \quad \text{Eq. 51}$$

where  $H_v$  is the heat of vaporization. At the VLE the pressure of the system is that of the saturated vapor obtained from 2 $\phi$ MD simulations. [344] The experimental [326] and calculated vapor pressure data and its Clausius-Clapeyron fit – with the obtained and experimental critical point – are shown on **Figure 51**, where a good agreement can be seen between the two data sets.

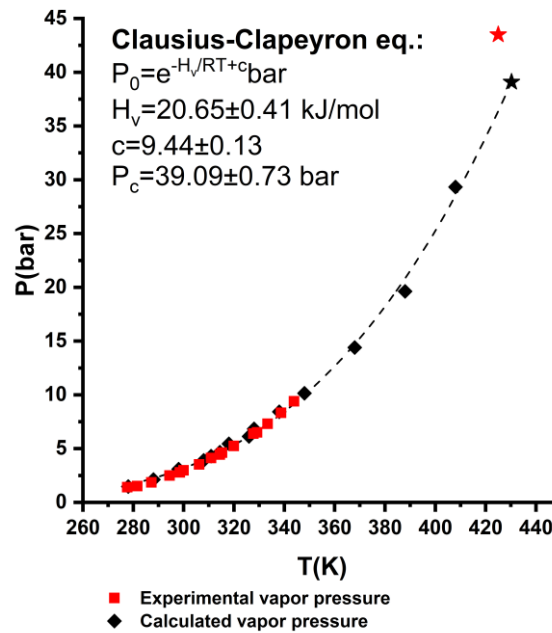


**Figure 51** Vapor densities obtained from 2 $\phi$ MD and experiment, shown with black diamonds and red squares, respectively. The Clausius-Clapeyron fit, the critical parameters derived from calculated densities ( $T_{c,p} = 430.25 \pm 2.50 \text{ K}$  and  $P_{c,p} = 39.09 \pm 0.73 \text{ bar}$ ) and experiment ( $T_{c,exp} = 425 \text{ K}$  and  $P_{c,exp} = 43.2 \text{ bar}$  [351]) are also shown by black and red stars, respectively. All experimental data have been taken from the Dortmund Databank [326]

The obtained critical properties are found to be in good agreement with experimental values. The deviation of  $T_c$  is 1.5% ( $T_{c,p} = 430.25 \pm 2.50 \text{ K}$  vs.  $T_{c,exp} = 425 \text{ K}$  [351]),  $\rho_c$  is

4.5% ( $\rho_{c,calc} = 234.25 \pm 2.66 \text{ kg/m}^3$  vs.  $\rho_{c,exp} = 245 \text{ kg/m}^3$ ), and  $P_c$  is 10% ( $P_{c,p} = 39.09 \pm 0.73 \text{ bar}$  vs.  $P_{c,exp} = 43.2 \text{ bar}$  [351]), and the heat of vaporization is 4% ( $H_{v,calc} = 20.65 \pm 0.41 \text{ kJ/mol}$  vs.  $H_{v,exp} = 21.47 \text{ kJ/mol}$  [351]) from the experimental values. This data indicates that the hereby used model and methods can capture the important properties of 1,3-butadiene from the VLE to the critical point.

#### 4.4.3 Critical parameters based on thermochemical properties

Alternatively, the critical temperature can be also obtained by calculating the surface tension ( $\gamma$ ) from the VLE to the critical point, as surface tension drops to zero as coexisting phases – thus surfaces – disappear. By extrapolating a linear fit of  $\gamma(T)$  to the point where  $\gamma = 0 \text{ mN/m}$ ,  $T_c$  can be predicted. [344] Surface tension have been calculated as implemented in GROMACS [79], from the difference between normal and lateral pressure

$$\gamma(t) = \frac{L_z}{n} \left\{ P_z(t) - \frac{P_x(t) + P_y(t)}{2} \right\} \quad \text{Eq. 52}$$

where  $L_z$  is the length of the simulation box in  $Z$  direction,  $n$  is the number of surfaces ( $n = 2$  in this case as two liquid-vapor interfaces appear in each simulation boxes), and  $P_x$ ,  $P_y$  and  $P_z$  are the pressure components along  $X$ ,  $Y$  and  $Z$  directions. The calculated surface tension values are in good agreement with the available data from experiments, as  $\gamma_{298K,exp} = 12.49 \text{ mN/m}$  [352] and  $\gamma_{298K,calc} = 14.25 \pm 1.30 \text{ mN/m}$ , which means an approximately 14% deviation. This surface tension value and its deviation from the experiment is small compared to other organic molecules such as methylamine (42.4 mN/m with 3 mN/m deviation reported in Ref. [353]) and formamide (58.2 mN/m underestimated by 9.2 mN/m in Ref. [354]). For a one component system temperature dependence of the surface tension can be describe by a linear term (**Eq. 46**), in which the slope of the function represents the surface excess entropy ( $S_\gamma$ ) and the intercept the surface excess enthalpy ( $H_\gamma$ ), which are independent of the temperature. [355]

$$\gamma(T) = H_\gamma - TS_\gamma \quad \text{Eq. 53}$$

The obtained surface tension values of 1,3-butadiene from the slab simulations between 278-408 K are shown on **Figure 52**, along with the extrapolated linear fit and the 95% confidence intervals of the data. The obtained values of  $\gamma$  are getting noisy at higher temperatures and the obtained  $T_c$  ( $T_{c,\gamma} = 409.56 \pm 3.76 \text{ K}$ ) is way below the previously obtained critical temperature from the Wegner-equation ( $T_{c,p} = 430.25 \pm 2.50 \text{ K}$ ) and also from the experimental values ( $T_{c,exp} = 425 \text{ K}$ ).

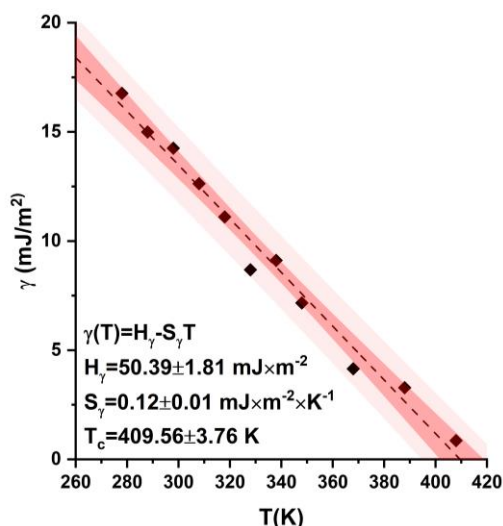


**Figure 52** Slope of surface-tension on the temperature of 1,3-butadiene in the subcritical region. The linear fit and the 95% confidence interval of the fit are also shown. By the extrapolation of the linear fit to  $\gamma = 0$  mN/m  $T_{c,\gamma}$  was predicted to be  $409.56 \pm 3.76$  K.

Linear temperature dependence of the potential energy of the entire system can be also used for the determination of the critical temperature ( $T_{c,Epot}$ ), although the state of the system needs to be assigned (system belongs either VLE or SC). If this classification is made, then the intersection of the two lines will determine the  $T_{c,Epot}$  value as shown in **Figure 53**. In this case, the obtained  $T_{c,Epot}$  coincided with the experimental value (425.0 K).

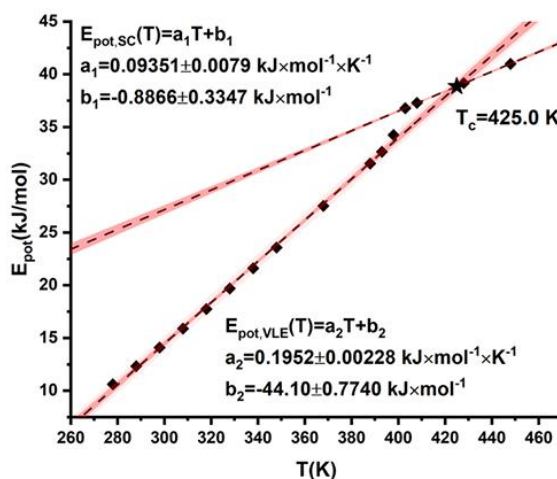


**Figure 53** The dependence of potential energy of 1,3-butadiene on temperature. All data has been obtained from  $2\phi$  simulations. Two linear fits have been added to the diagram at the break points of the data set, representing the regions where the vapor and liquid phases are clearly distinguishable, and after the two phases merge together. At the intersection of the lines the critical temperature can be obtained ( $T_c = 425.0$  K)

#### 4.4.4 Partitioning of molecules

As **Figure 49** shown, when the temperature of the system rises, the liquid phase gets less dense, the Voronoi vertices of the molecules become larger, and  $r_{max,liq}$  also grows. At the same time more molecules evaporate to the vapor phase and liquid-like droplets appear,

which can be seen as a group of ‘phase transferring’ molecules (**Figure 54**). The distribution of 1,3-butadiene molecules between the different phases and the  $r_{max,liq}$  values in different temperatures are found in **Table 10**.

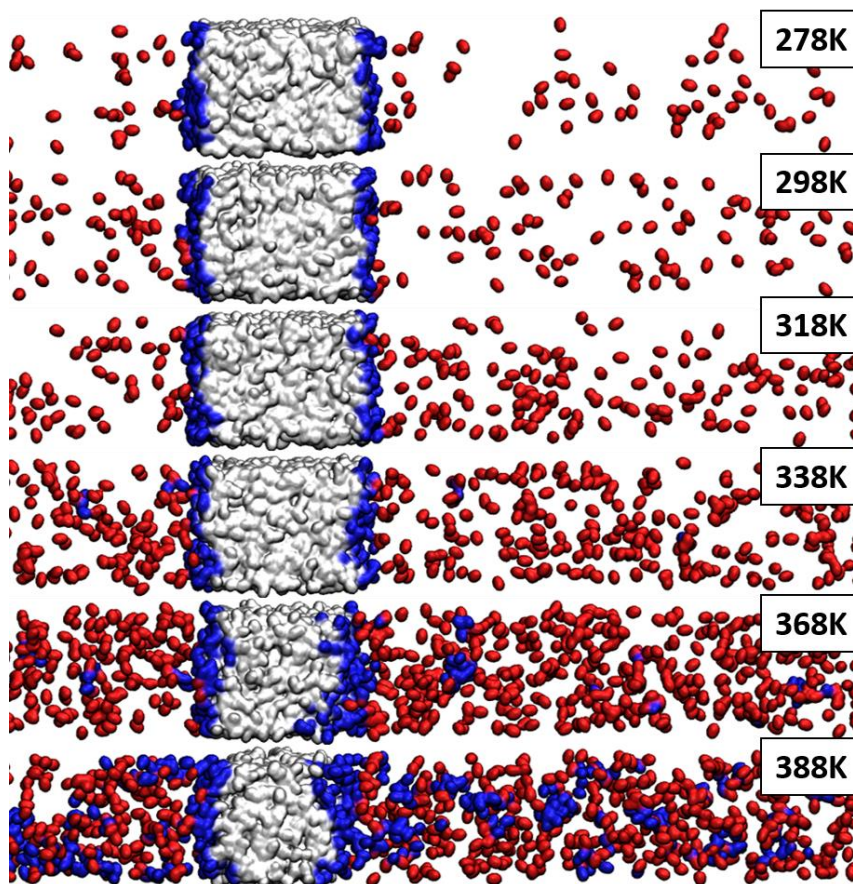


**Figure 54** The selection of liquid, vapor and “phase transferring” molecules from 278 K-388 K. White indicates liquid, red indicates vapor and blue indicates ‘phase transferring’ molecules. The value of  $\alpha$  was 10%.

**Table 10** The distribution of 1,3-butadiene molecules between the different phases and the obtained  $r_{max,liq}$  values at the investigated temperatures. The derived specific molar surface area ( $A_\gamma$ ) and molar surface excess enthalpy ( $H_{m,\gamma}$ ), entropy ( $S_{m,\gamma}$ ) and Gibbs free energy ( $G_{m,\gamma}$ ) are also given.

T (K)	$r_{max,liq}$ (Å)	vapor phase molecules (%)	liquid phase molecules (%)	‘phase transferring’ molecules (%)	$A_\gamma$ (nm <sup>2</sup> /molecule)	$H_{m,\gamma}$ (kJ/mol)	$S_{m,\gamma}$ (J/molK)	$G_{m,\gamma}$ (kJ/mol)
278	6.29	4.90	88.23	6.83	0.21	12.5	29.8	4.2
298	6.22	9.10	84.07	6.83	0.21	12.5	29.8	3.6
318	6.50	15.17	77.90	6.93	0.20	12.3	29.4	3.0
338	7.00	22.53	69.63	7.83				
368	8.42	33.17	55.63	11.20				
388	9.13	41.30	37.90	20.80				

By selecting the ‘phase transferring’ molecules at each temperature, it is clearly observable from **Figure 54** that at lower temperatures, from 278 K-318 K, these molecules are identical to the surface molecules, thus the molar surface area ( $A_\gamma$ ) of the 1,3-butadiene molecules can be calculated in the following way:

$$A_\gamma = \frac{2 \times L_x \times L_y}{\langle N_\gamma \rangle} \quad \text{Eq. 54}$$

where  $L_x$  and  $L_y$  are the  $x$  and  $y$  dimensions of the simulation box, and  $\langle N_\gamma \rangle$  is the average number of ‘phase transferring’ molecules. As seen from **Table 10**, the molar surface excess enthalpy ( $H_{m,\gamma}$ ) and entropy ( $S_{m,\gamma}$ ) can be calculated from the surface excess thermochemical properties by means of  $A_\gamma$  values:

$$H_{m,\gamma} = H_\gamma \times A_\gamma \quad \text{Eq. 55}$$

$$S_{m,\gamma} = S_\gamma \times A_\gamma \quad \text{Eq. 56}$$

As shown in **Table 10**, the calculated molar surface excess enthalpy and entropy are constant in the range of 278 K to 318 K: the value of  $H_{m,\gamma}$  is 12.5 kJ/mol while  $S_{m,\gamma}$  is 29.8 J/molK. As seen on **Figure 54**, above 318 K in the vapor phase small liquid-like droplets of 1,3-butadiene molecules appear which are considered to be ‘phase transferring’, which phenomena make it meaningless to calculate thermochemical surface properties by this method.  $G_{m,\gamma}$  has also been calculated for the lower temperatures, and it was found to be linearly decreasing as temperature rises.

#### 4.4.5 Temperature and pressure dependence of the specific surface area of 1,3-butadiene

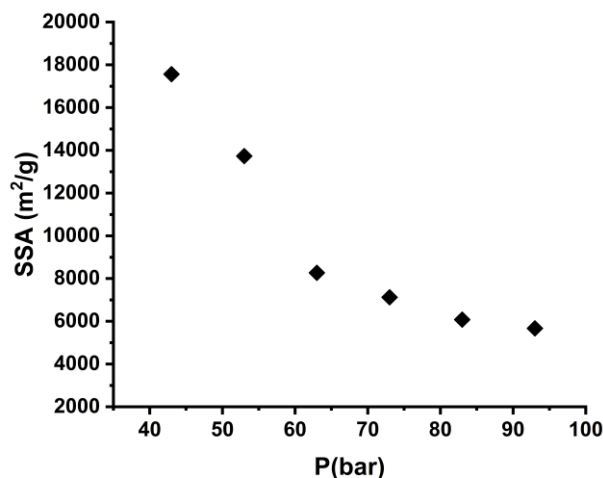


**Figure 55** Pressure dependence of Specific Surface Area (SSA) of 1,3-butadiene in supercritical conditions.

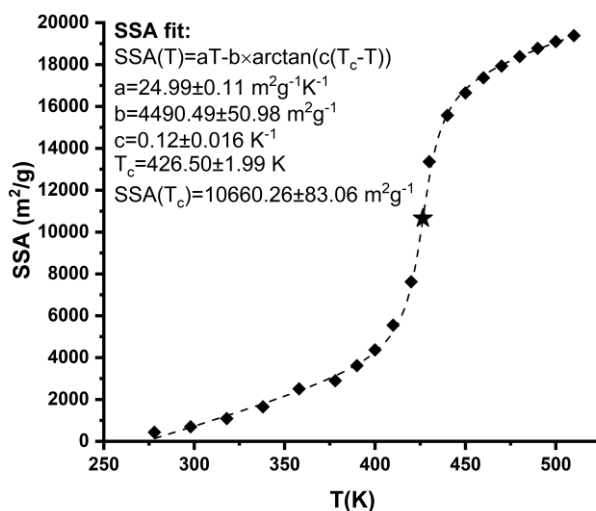


**Figure 56** Temperature dependence of Specific Surface Area (SSA) of 1,3-butadiene in sub- and supercritical conditions, from 278-510 K. The values of SSA are obtained from NPT liquid and supercritical simulations. The SSA values are indicated with black diamonds, and the supercritical point is indicated with a black star.

Although, no macroscopic surface can be defined at the supercritical condition, instantaneous formation of cavities in supercritical fluids can be identified and their surfaces act as a dynamic internal surface of the system at the molecular scale. The size of the (external and internal) molecular surface of the system can be estimated via solvent-accessible surface area (SASA) calculation. Average solvent-accessible surface area (SASA) over the NPT trajectory was calculated and converted into Specific Surface Area (SSA) by dividing it by the number of molecules in the simulation system and by the molar mass of

1,3-butadiene. In SASA calculation the molecular surface was determined with a probe radius of 1.4 Å using the Eisenhaber algorithm. [356] By raising the pressure, the individual molecules get closer to each other and form a liquid-like structure and the SSA becomes lower (**Figure 55**). On the contrary, the molecules get further away from each other by increasing temperature, forming a vapor-like structure and the SSA becomes higher (**Figure 56**). On the temperature dependence of the SSA the following empiric equation can be fitted:

$$SSA(T) = aT - b \times \arctan(c(T_c - T)) \quad Eq. 57$$

where  $a$ ,  $b$  and  $c$  are fitting parameters, and  $T_{c,SSA}$  (426.50 K) can be obtained - found at the steepest part of the function - which shows within 1% of deviation from the experimental value of  $T_c$ . The theoretical limit of the total molecular surface of the system can be obtained by assuming that none of the 1,3-butadiene molecules have any contact with the others which results in the value of SSA as large as 24944 m<sup>2</sup>/g for 1,3-butadiene system. At the critical point, the  $SSA_{T_c}$  is 10660.26 m<sup>2</sup>/g which is 42.74% of the maximum value, while it goes up to 77.71% at 510 K ( $SSA_{510K} = 19383.53$  m<sup>2</sup>/g).

#### 4.4.6 Summary and Conclusions

In this work the OPLS-AA force field parameters of 1,3-butadiene with 1.14\*CM1A partial atomic charges obtained from the LigParGen [313]–[315] webserver have been tested in a wide range of temperatures (278-510 K) and pressures (43-93 bar). In the subcritical region the methodology of 2φMD have been followed, which produced excellent agreement with experimental results in density, pressure, surface tension and potential energy values.

**Table 11** Comparison of the critical properties of 1,3-butadiene obtained by different methods

Method	$T_c$ (K)	$P_c$ (bar)
experimental [326]	425	43.2
$\rho$ based	430.25	39.16
$\gamma$ based	409.56	29.26
$E_{pot}$ based	425.00	36.47
SSA based	426.50	37.22

Throughout this work several different methods have been introduced to calculate critical temperature (**Table 11**), from which with the help of Clausius-Clapeyron equation the critical pressure and the heat of vaporization was calculated as shown in **Figure 51**. The calculated value of  $H_v$  shows excellent match with experimentally available data. While based on the potential energy ( $E_{pot}$ )  $T_{c,exp}$  can be reproduced perfectly,  $P_c$  is underestimated by 18.5% compared to the experimental value. The surface tension ( $\gamma$ ) based prediction of  $T_c$  and  $P_c$  proven to be the most inaccurate even if the calculated surface tension values were

found to be in good agreement with experiments. The SSA based calculation of the critical temperature seems to be also a good option for calculating the critical temperature as it matches the experimental value with 99% accuracy, but again, the critical pressure is 16.05% away from the experimental value. In the case of 1,3-butadiene the density based calculations of the parameters seemed to be the best alternative, as experimental  $T_c$  and  $P_c$  were reproduced within 1.1% and 9.6% error, respectively. Out of these results it is clearly visible that the higher sampling range and the right choice of force field can improve the quality of the calculated critical data, but the uncertainty of the fitting parameters can divert the obtained data significantly.

The methodology, force field and set up introduced in this study combined with the TraPPE model for CO<sub>2</sub> [224], [348] can be used in the future for the investigation of the VLE of the binary mixture of CO<sub>2</sub> and 1,3-butadiene, in order to better understand the formation of EVL.

## 5 SUMMARY

The chemical industry produces a grave amount of substances annually, out of which a non-negligible portion is released into the environment, leading to ascendant environmental stress. At the same time the health and environmental effects of most chemicals is yet to be understood. For the support of environmental and toxicological sciences, the effect and structure of chemically inert industrial compounds can be characterized by using the tools of computational chemistry.

Throughout my work the passive membrane permeation of 10 industrially relevant compounds – 1,4-dioxane, morpholine, oxane, phenol, 3-ethylidene-6-vinyltetrahydro-2H-pyran-2-one (EVL), octa-1,3,7-triene (BDDI), 2-vinylhepta-4,6-dienoic acid (AC1), 2-ethylhepta-4,6-dienoic acid (AC2), 3-ethylidene-2-methylene-5-(prop-1-en-1-yl)-dihydrofuran (LAC2) and 3-ethyl-5-propylidene-furan-2-on (LAC3) – have been investigated by the means of molecular dynamics (MD), and their membrane structure altering capability was described in detail. In all of the investigated cases it was found that the compounds can permeate inside model, DPPC composed biological membranes, and promote changes in the bilayer structure. In the cases of EVL, BDDI, LAC2 and LAC3 droplet formation in the bulk phase was inspected.

In the case of 8 compounds the free energy of membrane permeation profile was obtained by using enhanced sampling methods – Metadynamics and Well-Tempered Metadynamics – and also a density based method. It was found that the density based free energy calculation matches the results of the tried methods within the limits of chemical accuracy – except in the case of LAC2 - while it can be significantly faster. Three different types of free energy profiles were found in the case of the investigated compounds based on the number of free energy barriers: one free energy barrier was found in the cases of phenol and AC1; two barriers in the cases of BDDI and oxane; and three barriers for EVL, LAC2, 1,4-dioxane and morpholine.

The membrane/bulk phase partition coefficient and membrane volume fraction was calculated for all the molecules. Based on these parameters and the free energy profiles a permeation order of the molecules can be established. In this order three different types of molecules were separated from each other: molecules which don't permeate into the membrane due to their high free energy barriers and low partition coefficient (BDDI, LAC2 and LAC3); molecules which are able to permeate the bilayer, have moderate permeation barriers and slightly negative partition coefficients (EVL, 1,4-dioxane and morpholine); and

molecules which can spontaneously diffuse into the bilayer without a free energy barrier, and have positive partition coefficients (phenol, oxane, AC1 and AC2). Based on the volume fraction theory aside from BDDI, all molecules act as a narcotic in the set simulation environment.

In the case of six compounds – 1,4-dioxane, phenol, 3-ethylidene-6-vinyltetrahydro-2H-pyran-2-one, octa-1,3,7-triene, 2-vinylhepta-4,6-dienoic acid and 3-ethylidene-2-methylene-5-(prop-1-en-1-yl)-dihydrofuran – the concentration dependence of the permeation profile was investigated. In the case of compounds with limited water solubility, the free energy barrier at the membrane headgroups significantly decrease at a lower concentration, and their thermodynamically most favored position becomes the inner site of the headgroups, where the ester groups of the phospholipids are found. In contrast where no aggregate or droplet formation is observed, the free energy barriers increase in infinite dilution.

In the cases of 1,4-dioxane, morpholine, phenol and oxane the presence of the additives on the permeation of water molecules was also analyzed by using WT-MD. It was found, that the membrane structure altering mechanism of the compounds in question make the free energy of permeation barrier for water molecules significantly lower, which also shows in the rising amount of water molecules in the bilayer center. In the case of oxane – which only has two permeation barriers - it means that 5 times more water molecules are found in the central region compared to additive free model DPPC membranes.

The vapor-liquid equilibria and supercritical phase of 1,3-butadiene was described at various temperatures (273-510 K) and pressures (43-93 bar) by using two-phase MD. To be able to accurately predict the vapor and liquid densities of 1,3-butadiene from the slab simulations and to select the phase transferring molecules, I have elaborated a new method, where with a single parameter, the molecules of different phases can be separated based on the sphericity of their Voronoi polygons. By using this method, the vapor and liquid densities of the VLE-curve and supercritical point were reproduced within 10 % compared to experimental values. Additionally several methods have been tried for obtaining the supercritical point of 1,3-butadiene, out of which the density based method prove to be the most accurate. By pairing the used methods and model with an appropriate CO<sub>2</sub> force field, their two-component system could be investigated in detail at different compositions and environment, in order to understand the reaction, and fine-tune it towards higher EVL selectivity.

## 6 ÖSSZEFOGLALÓ

A vegyipar minden évben jelentős mennyiségű kemikáliát állít elő. Ennek nem elhanyagolható része kerül a környezetbe kezeletlenül, ami egyre növekvő környezeti stresszhez vezet, hiszen a legtöbb vegyi anyag egészségügyi és környezeti hatásait még nem ismerjük. A környezeti- és toxikológiai tudományok támogatása érdekében az inert ipari vegyületek hatását és szerkezetét a számítási kémia eszközeivel jól jellemezhetjük.

Munkám során 10 iparilag releváns vegyület - 1,4-dioxán, morfolin, oxán, fenol, 3-etilidén-6-viniltetrahidro-2H-pirán-2-on (EVL), okta-1,3,7-trién (BDDI), 2-vinilhepta-4,6-dienoosav (AC1), 2-etilhepta-4, 6-diensav (AC2), 3-etilidén-2-metilén-5-(prop-1-en-1-il)-dihidrofurán (LAC2) és 3-etil-5-propilidén-furán-2-on (LAC3) - passzív membránpermeációját vizsgáltam a molekuladinamika (MD) módszertanával és részletesen leírtam ezen vegyületek membránszerkezet-változtató képességét. Valamennyi esetben megállapítható, hogy a vegyületek képesek a modell, DPPC foszfolipidekből álló biológiai membránok belsejébe hatolni, ami által a kettősréteg szerkezete megváltozik. Az EVL, BDDI, LAC2 és LAC3 esetében cseppképződés tapasztalható a vizes fázisban.

8 vegyület esetében a membránpermeáció szabad energia profilját fokozott mintavételi eljárások – 'Metadinamika' és 'Well-Tempered Metadinamika' -, valamint egy sűrűség alapú módszer felhasználásával kaptam meg. Megállapítható, hogy a sűrűség alapú szabadenergia-számítás a kémiai pontosság határain belül - a LAC2 kivételével - megegyezik a további módszerek eredményeivel, miközben jelentősen gyorsabb. A vizsgált vegyületek esetében a szabadenergia-gátak száma alapján három különböző típusú szabadenergia-profilot találtunk: a fenol és az AC1 esetében egy, a BDDI és az oxán esetében kettő, az EVL, az LAC2, az 1,4-dioxán és a morfolin esetében pedig három szabadenergia-gát található.

A membrán/víz megoszlási hányadost és a vegyület membránon belüli térfogatarányát minden molekula esetén kiszámítottam. Ezen paraméterek és a szabadenergia-profilok alapján egy permeációs sorrendet állíthatunk fel. Három különböző típusú anyagot különíthetünk el egymástól: azok a molekulák, amelyek magas szabadenergia-gátjuk és alacsony megoszlási együtthatójuk miatt nem képesek beoldódni a membránba (BDDI, LAC2 és LAC3); azok a molekulák, amelyek képesek áthatolni a kettősrétegen, közepes permeációs gátakkal és enyhén negatív megoszlási együtthatóval rendelkeznek (EVL, 1,4-dioxán és morfolin); illetve azok a molekulák, amelyek spontán diffundálnak a kettősrétegbe energiagát nélkül, melyek megoszlási együtthatója pozitív (fenol, oxán, AC1 és AC2). A

térfogatarány-elmélet alapján a BDDI-n kívül minden molekula narkotikus viselkedést mutat az alkalmazott szimulációs környezetben.

Hat vegyület - 1,4-dioxán, fenol, 3-etilidén-6-viniltetrahidro-2H-pirán-2-on, okta-1,3,7-trién, 2-vinilhepta-4,6-diensav és 3-etilidén-2-metilén-5-(prop-1-en-1-il)-dihidrofuran - esetében megvizsgáltam a beoldódási profil koncentrációfüggését. A korlátozott vízdékonyságú vegyületek esetében a szabadenergia-gát a membránfejcsoportoknál alacsonyabb koncentráció esetén jelentős mértékben csökken, így a termodinamikailag legkedvezőbb pozíciójuk a fejcsoportok belső oldala lesz, ahol a foszfolipidek észtercsoportjai találhatóak. Ezzel szemben azon molekulák esetében, ahol nem figyelhető meg aggregátum- vagy cseppképződés, a szabadenergia-gátak végtelen hígítás esetén jelentősen megnövekednek.

Az 1,4-dioxán, a morfolin, a fenol és az oxán esetében az adalékanyagok vízmolekulák permeációjára gyakorolt hatását is elemeztem WT-MD segítségével. Megállapítható, hogy a szóban forgó vegyületek membránszerkezetet módosító mechanizmusa jelentősen csökkenti a vízmolekulák permeációs gátjának szabadenergiáját, ami a vízmolekulák membránon belül található mennyiségében is megmutatkozik: Az oxán esetében - amelynek csak két permeációs gátja van - ez azt jelenti, hogy a központi régióban ötször több vízmolekula található, mint az adalékmentes DPPC membrán modellben.

Az 1,3-butadién gőz-folyadék egyensúlyi (VLE) állapotát és szuperkritikus fázisát különböző hőmérsékleteken (273-510 K) és nyomáson (43-93 bar) kétfázisú MD segítségével vizsgáltam. Annak érdekében, hogy a kétfázisú szimulációk alapján az 1,3-butadién gőz- és folyadéksűrűségét pontosan megállapíthassam, és a fázist váltó molekulákat kiválaszthassam, egy új módszert dolgoztam ki, ahol egyetlen paraméter segítségével a különböző fázisok molekulái a hozzájuk tartozó Voronoi-poligonok gömbszerűsége alapján elkülöníthetővé válnak. A módszert felhasználva a VLE-görbe és a szuperkritikus pont kísérleti értékei 10 %-on belül reprodukálhatóak voltak 1,3-butadién esetén. Emellett több módszert is teszteltem az 1,3-butadién szuperkritikus pontjának meghatározására, amelyek közül a sűrűségeen alapuló módszer bizonyult a legpontosabbnak. Ha az alkalmazott módszereket és butadién modellt megfelelő CO<sub>2</sub> erőterrel párosítjuk a jövőben, a két komponensű rendszerük részletesen vizsgálható lesz különböző összetételek és környezeti paraméterek mellett. Ezáltal lehetővé válik a reakció megértése és a reakció finomhangolása a nagyobb EVL-szelektivitás érdekében.

## 7 NEW SCIENTIFIC RESULTS – THESES

### 1. The free energy of membrane permeation profile of the investigated compounds can be classified into three groups.

The membrane permeation of eight industrially relevant compounds (1,4-dioxane, phenol, oxane, morpholine, 3-ethylidene-6-vinyltetrahydro-2H-pyran-2-one (EVL), octa-1,3,7-triene (BDDI), 2-vinylhepta-4,6-dienoic acid (AC1), 3-ethylidene-2-methylene-5-(prop-1-en-1-yl)-dihydrofuran (LAC2)) into DPPC composed bilayers were investigated via Well-Tempered Metadynamics. In each cases 100 additives were inserted into the simulation box. Based on the profiles three different types can be specified: with one free energy barrier - in the cases of AC1 and phenol - which is found in the bilayer center; with two free energy barriers - in the cases of oxane and BDDI – which is found at the headgroups region; and with three free energy barriers, in the cases of EVL, 1,4-dioxane, morpholine and LAC2, where the barriers are found at the headgroups region and in the bilayer center.

### 2. The free energy of membrane permeation profile of the investigated compounds show concentration dependence.

The concentration dependence of the membrane permeation of six industrially relevant compounds (1,4-dioxane, phenol, 3-ethylidene-6-vinyltetrahydro-2H-pyran-2-one (EVL), octa-1,3,7-triene (BDDI), 2-vinylhepta-4,6-dienoic acid (AC1), 3-ethylidene-2-methylene-5-(prop-1-en-1-yl)-dihydrofuran (LAC2)) into DPPC composed bilayers were investigated by using Metadynamics and Well-Tempered Metadynamics. In all the cases it was found that the permeation profiles are affected by the permeant concentration. When – due to the limited solubility of the permeant – a liquid droplet is formed in the bulk phase, the free energy barrier increases at a higher concentration; at the same time in the cases of highly soluble and miscible compounds the free energy barrier in the bilayer center decreases at higher concentration.

### 3. The presence of additives can affect the free energy of membrane permeation profile of water molecules.

In the cases of 1,4-dioxane, phenol, oxane and morpholine the free energy of membrane permeation of water molecules into DPPC composed model membranes was calculated by using Well-Tempered Metadynamics. It was found that water molecules have a lower permeation barrier when the membrane structure is altered due to the presence of additives. Parallel to the lower free energy barrier, a significantly higher amount of water molecules was found inside the bilayer, which in the presence of oxane – which have a

thermodynamically favored position in the bilayer center – exceeded 5 times the amount of molecules compared to the additive free DPPC membranes.

**4. Density based free energy of membrane permeation calculations can be a reasonable alternative to enhanced sampling methods.**

The membrane permeation of eight industrially relevant compounds (1,4-dioxane, phenol, oxane, morpholine, 3-ethylidene-6-vinyltetrahydro-2H-pyran-2-one (EVL), octa-1,3,7-triene (BDDI), 2-vinylhepta-4,6-dienoic acid (AC1), 3-ethylidene-2-methylene-5-(prop-1-en-1-yl)-dihydrofuran (LAC2)) into DPPC composed bilayers were investigated via Well-Tempered Metadynamics and a density based approach (D2E). In this method the free energy profile is obtained based on the density distribution of the investigated compounds in the simulation box along the membrane normal. In almost all cases the permeation profile obtained by WT-MD and D2E were within the limits of chemical accuracy, except in the case of LAC2, where the maximum deviation was 5.4 kJ/mol. Based on these results the application of density based free energy of permeation calculations could be a reasonable alternative – or first guess – in the cases of small, neutral molecules.

**5. Based on the free energy profiles and membrane/bulk partition coefficients, a permeation order of the molecules can be established.**

The membrane/bulk phase partition coefficient and membrane volume fraction was calculated for 1,4-dioxane, phenol, oxane, morpholine, 3-ethylidene-6-vinyltetrahydro-2H-pyran-2-one (EVL), octa-1,3,7-triene (BDDI), 2-vinylhepta-4,6-dienoic acid (AC1), 2-ethylidenehepta-4,6-dienoic acid (AC2), 3-ethylidene-2-methylene-5-(prop-1-en-1-yl)-dihydrofuran (LAC2), 3-ethyl-5-propylidene-furan-2-one (LAC3) from classical molecular dynamics simulations. Based on these parameters and the free energy profiles, a permeation order of the molecules can be established. In this order three different types of molecules were separated from each other: molecules which don't permeate into the membrane due to their high free energy barriers and low partition coefficient (BDDI, LAC2 and LAC3); molecules which are able to permeate the bilayer, have moderate permeation barriers and slightly negative partition coefficients (EVL, 1,4-dioxane and morpholine); and molecules which can spontaneously diffuse into the bilayer without a free energy barrier, and have positive partition coefficients (phenol, oxane, AC1 and AC2). Based on Mullins's volume fraction theory aside from BDDI, all molecules act as a narcotic in the used simulation environment.

**6. Vapor, Liquid and Phase transferring molecules were separated from each other based on sphericity in the case of 1,3-butadiene in the Vapor-Liquid**

**Equilibria. By using this method experimentally available densities in the VLE and the supercritical point was reproduced within 10% of deviation.**

I have developed a new method for classifying molecules in the vapor-liquid equilibria, which is able to specify the phase changing molecules. The method is based on the sphericity of the Voronoi polygons generated for each molecule in a slab simulation. The method was applied in the case of 1,3-butadiene, in the temperature range of 278-408 K, and the experimentally available densities were reproduced within 5 kg/m<sup>3</sup>. On the computed dataset the law of rectilinear diameters and the Wegner equation was applied and the supercritical temperature and density were obtained within 10% of deviation.

**7. The temperature dependence of Specific Surface Area in the Vapor-Liquid Equilibria can be used to obtain the supercritical temperature.**

The temperature dependence of Specific Surface Area (SSA) in the Vapor-Liquid Equilibria was investigated in the case of 1,3-butadiene, and it was found that an empirical equation can be fitted on this diagram:

$$SSA(T) = aT - b \times \arctan(c(T_c - T))$$

From this  $T_{c,SSA} = 426.50$  K was obtained, which is within 1% of deviation from the experimental value of the supercritical temperature. At the same time the theoretical limit of the total molecular surface of the system can be obtained by assuming that none of the 1,3-butadiene molecules have any contact with the others; which results in the value of SSA as large as 24944 m<sup>2</sup>/g for 1,3-butadiene. At the critical point, the  $SSA_{T_c}$  is 10660.26 m<sup>2</sup>/g which is 42.74% of the maximum value, while it goes up to 77.71% at 510 K ( $SSA_{510K} = 19383.53$  m<sup>2</sup>/g).

## 8 REFERENCES

- [1] Z. Wang, G. W. Walker, D. C. G. Muir, and K. Nagatani-Yoshida, "Toward a Global Understanding of Chemical Pollution: A First Comprehensive Analysis of National and Regional Chemical Inventories," *Environ. Sci. Technol.*, vol. 54, no. 5, pp. 2575–2584, 2020.
- [2] R. A. Sheldon, "The E Factor: Fifteen years on," *Green Chem.*, vol. 9, no. 12, pp. 1273–1283, Nov. 2007.
- [3] J. Rockström *et al.*, "Planetary Boundaries: Exploring the Safe Operating Space for Humanity," *Ecol. Soc.*, vol. 14, no. 2, p. 32, 2009.
- [4] M. L. Diamond *et al.*, "Exploring the planetary boundary for chemical pollution," *Environ. Int.*, vol. 78, pp. 8–15, 2015.
- [5] J. Meijer *et al.*, "An annotation database for chemicals of emerging concern in exposome research," *Environ. Int.*, vol. 152, no. July, 2021.
- [6] V. Dulio and J. Slobodnik, "NORMAN—network of reference laboratories, research centres and related organisations for monitoring of emerging substances," *Environ. Sci. Pollut. Res.*, vol. 16, no. S1, pp. 132–135, Aug. 2009.
- [7] V. Dulio *et al.*, "Emerging pollutants in the EU: 10 years of NORMAN in support of environmental policies and regulations," *Environ. Sci. Eur.*, vol. 30, no. 5, 2018.
- [8] H. J. M. Verhaar, E. U. Ramos, and J. L. M. Hermens, "Classifying environmental pollutants. 2: Separation of class 1 (baseline toxicity) and class 2 ('polar narcosis') type compounds based on chemical descriptors," *J. Chemom.*, vol. 10, no. 2, pp. 149–162, 1996.
- [9] M. Penman, M. Banton, S. Erler, N. Moore, and K. Semmler, "Olefins and chemical regulation in Europe: REACH," *Chem. Biol. Interact.*, vol. 241, no. December 2006, pp. 59–65, 2015.
- [10] B. Versonnen *et al.*, "Analysis of the ecotoxicity data submitted within the framework of the REACH Regulation. Part 4. Experimental terrestrial toxicity assays," *Sci. Total Environ.*, vol. 475, pp. 123–131, 2014.
- [11] C. Rovida *et al.*, "Toxicity testing in the 21st century beyond environmental chemicals.," *ALTEX*, vol. 32, no. 3, pp. 171–81, 2015.
- [12] S. Seethapathy, T. Górecki, and X. Li, "Passive sampling in environmental analysis," *J. Chromatogr. A*, vol. 1184, no. 1–2, pp. 234–253, 2008.
- [13] X. Zhang *et al.*, "Discrimination of excess toxicity from narcotic effect: Comparison of toxicity of class-based organic chemicals to daphnia magna and tetrahymena pyriformis," *Chemosphere*, vol. 93, no. 2, pp. 397–407, 2013.
- [14] H. J. M. Verhaar, C. J. van Leeuwen, and J. L. M. Hemens, "Classifying Environmental-Pollutants 1. Structure-Activity-Relationships for Prediction of Aquatic Toxicity," *Chemosphere*, vol. 25, no. 4, pp. 471–491, 1992.
- [15] J. J. Li *et al.*, "Development of thresholds of excess toxicity for environmental species and their application to identification of modes of acute toxic action," *Sci. Total Environ.*, vol. 616–617, pp. 491–499, 2018.
- [16] T. Öberg, "A QSAR for baseline toxicity: Validation, domain of application, and prediction," *Chem. Res. Toxicol.*, vol. 17, no. 12, pp. 1630–1637, 2004.
- [17] D. Mackay, J. A. Arnot, E. P. Petkova, and K. B. Wallace, "The physicochemical basis of QSARs for baseline toxicity," *SAR QSAR Environ. Res.*, vol. 20, no. 3–4, pp. 393–414, 2009.
- [18] G. D. Veith, D. J. Call, and L. T. Brooke, "Structure-Toxicity Relationships for the Fathead Minnow, *Pimephales promelas*: Narcotic Industrial Chemicals," *Can. J. Fish. Aquat. Sci.*, vol. 40, pp. 743–748, 1983.
- [19] M. Nendza, M. Müller, and A. Wenzel, "Discriminating toxicant classes by mode of action: 4. Baseline and excess toxicity," *SAR QSAR Environ. Res.*, vol. 25, no. 5, pp. 393–405, 2014.
- [20] B. I. Escher *et al.*, "Baseline Toxicity (Narcosis) of Organic Chemicals Determined by In

- Vitro Membrane Potential Measurements in Energy-Transducing Membranes,” *Environ. Sci. Technol.*, vol. 36, no. 9, pp. 1971–1979, 2002.
- [21] C. E. Overton, *Studien über die Narkose: zugleich ein Beitrag zur allgemeinen Pharmakologie*. G. Fischer, 1901.
- [22] H. Meyer, “The theory of alcohol narcosis [Zur Theorie der Alkoholnarkose] Arch,” *Exp. Pathol. Pharmacol.*, vol. 42, pp. 109–118, 1899.
- [23] H. Könemann, “Quantitative structure-activity relationships in fish toxicity studies Part 1: Relationship for 50 industrial pollutants,” *Toxicology*, vol. 19, no. 3, pp. 209–221, 1981.
- [24] M. T. D. Cronin, “(Q)SARs to predict environmental toxicities: current status and future needs,” *Environ. Sci. Process. Impacts*, vol. 19, no. 3, pp. 213–220, 2017.
- [25] S. T. J. Droge, “Membrane–Water Partition Coefficients to Aid Risk Assessment of Perfluoroalkyl Anions and Alkyl Sulfates,” *Environ. Sci. Technol.*, vol. 53, no. 2, pp. 760–770, Jan. 2019.
- [26] J. L. Mullins, “Some physical mechanisms in narcosis,” *Chem. Rev.*, vol. 54, no. 2, pp. 289–323, 1954.
- [27] B. M. George and J. J. Pandit, “General anaesthetics as ‘awakening agents’? Re-appraising the evidence for suggested ‘pressure reversal’ of anaesthesia,” *Clin. Exp. Pharmacol. Physiol.*, vol. 48, no. 11, pp. 1454–1468, Nov. 2021.
- [28] A. P. Van Wezel and A. Opperhuizen, “Narcosis Due To Environmental Pollutants in Aquatic Organisms: Residue-Based Toxicity, Mechanisms, and Membrane Burdens,” *Crit. Rev. Toxicol.*, vol. 25, no. 3, pp. 255–279, 1995.
- [29] D. Van Der Spoel, S. Manzetti, H. Zhang, and A. Klamt, “Prediction of Partition Coefficients of Environmental Toxins Using Computational Chemistry Methods,” *ACS Omega*, vol. 4, no. 9, pp. 13772–13781, 2019.
- [30] P. Yamin, R. Isele-Holder, and K. Leonhard, “Predicting Octanol/Water Partition Coefficients of Alcohol Ethoxylate Surfactants Using a Combination of Molecular Dynamics and the Conductor-like Screening Model for Realistic Solvents,” *Ind. Eng. Chem. Res.*, vol. 55, no. 16, pp. 4782–4789, Apr. 2016.
- [31] A. Krämer *et al.*, “Membrane permeability of small molecules from unbiased molecular dynamics simulations,” *J. Chem. Phys.*, vol. 153, no. 12, p. 124107, 2020.
- [32] R. M. Venable, A. Krämer, and R. W. Pastor, “Molecular Dynamics Simulations of Membrane Permeability,” *Chem. Rev.*, vol. 119, no. 9, pp. 5954–5997, 2019.
- [33] P. Cullis and B. D. Kruijff, “Lipid Polymorphism and the Roles of Lipids in Membranes,” *Biochim. Biophys. Acta*, vol. 559, pp. 399–420, 1979.
- [34] T. Kobayashi and A. K. Menon, “Transbilayer lipid asymmetry,” *Curr. Biol.*, vol. 28, no. 8, pp. R386–R391, Apr. 2018.
- [35] C. Sohlenkamp and O. Geiger, “Bacterial membrane lipids: Diversity in structures and pathways,” *FEMS Microbiol. Rev.*, vol. 40, no. 1, pp. 133–159, 2015.
- [36] S. J. Singer and G. L. Nicolson, “The fluid mosaic model of the structure of cell membranes,” *Science*, vol. 175, pp. 720–731, 1972.
- [37] G. Van Meer and A. I. P. M. De Kroon, “Lipid map of the mammalian cell,” *J. Cell Sci.*, vol. 124, no. 1, pp. 5–8, 2011.
- [38] N. Wu, K. Palczewski, and D. J. Müller, “Vertebrate Membrane Proteins: Structure, Function, and Insights from Biophysical Approaches,” *Pharmacol. Rev.*, vol. 60, no. 1, pp. 43–78, 2008.
- [39] J. B. Parsons and C. O. Rock, “Progress in Lipid Research Bacterial lipids: Metabolism and membrane homeostasis,” *Prog. Lipid Res.*, vol. 52, no. 3, pp. 249–276, 2013.
- [40] T. Kaneda, “Iso- and anteiso-fatty acids in bacteria: biosynthesis, function, and taxonomic significance,” *Microbiol. Rev.*, vol. 55, no. 2, pp. 288–302, 1991.
- [41] D. Poger, B. Caron, and A. E. Mark, “Effect of Methyl-Branched Fatty Acids on the Structure

- of Lipid Bilayers,” *J. Phys. Chem. B*, vol. 118, no. 48, pp. 13838–13848, 2014.
- [42] J. M. Berg, J. L. Tymoczko, and L. Stryer, *Biochemistry, 5th edition*, 5th editio. New York: NCBI, 2002.
- [43] G. van Meer, D. R. Voelker, and G. W. Feigenson, “Membrane lipids: where they are and how they behave,” *Nat Rev Mol Cell Biol*, vol. 9, no. 2, pp. 112–124, 2008.
- [44] H. Noguchi, “Structure formation of lipid membranes : membrane self-assembly and vesicle opening-up to octopus-like micelles,” *AIP Conf. Proc.*, vol. 566, no. 1518, 2013.
- [45] F. Martelli, H.-Y. Ko, C. C. Borallo, and G. Franzese, “Structural properties of water confined by phospholipid membranes,” *Front. Phys.*, vol. 13, no. 1, p. 136801, 2018.
- [46] K. Gawrisch, D. Ruston, J. Zimmerberg, V. A. Parsegian, R. P. Rand, and N. Fuller, “Membrane dipole potentials, hydration forces, and the ordering of water at membrane surfaces,” *Biophys. J.*, vol. 61, no. 5, pp. 1213–1223, 1992.
- [47] J.-X. Cheng, S. Pautot, D. A. Weitz, and X. S. Xie, “Ordering of water molecules between phospholipid bilayers visualized by coherent anti-Stokes Raman scattering microscopy.,” *Proc. Natl. Acad. Sci. U. S. A.*, vol. 100, no. 17, pp. 9826–9830, 2003.
- [48] T. Fukuma, M. J. Higgins, and S. P. Jarvis, “Direct imaging of individual intrinsic hydration layers on lipid bilayers at Ångstrom resolution,” *Biophys. J.*, vol. 92, no. 10, pp. 3603–3609, 2007.
- [49] G. A. Yeghiazaryan, A. H. Poghosyan, and A. A. Shahinyan, “The water molecules orientation around the dipalmitoylphosphatidylcholine head group: A molecular dynamics study,” *Physica A*, vol. 362, pp. 197–203, 2006.
- [50] K. Inoue, P. C. Singh, S. Nihonyanagi, S. Yamaguchi, and T. Tahara, “Cooperative Hydrogen-Bond Dynamics at a Zwitterionic Lipid/Water Interface Revealed by 2D HD-VSFG Spectroscopy,” *J. Phys. Chem. Lett.*, vol. 8, pp. 5160–5165, 2017.
- [51] P. M. Kasson, E. Lindahl, and V. S. Pande, “Water ordering at membrane interfaces controls fusion dynamics,” *J. Am. Chem. Soc.*, vol. 133, no. 11, pp. 3812–3815, 2011.
- [52] L. Perera, U. Essmann, and M. L. Berkowitz, “Role of Water in the Hydration Force Acting between Lipid Bilayers,” *Langmuir*, vol. 12, no. 11, pp. 2625–2629, 1996.
- [53] M. J. Higgins, M. Polcik, T. Fukuma, J. E. Sader, Y. Nakayama, and S. P. Jarvis, “Structured water layers adjacent to biological membranes,” *Biophys. J.*, vol. 91, no. 7, pp. 2532–2542, 2006.
- [54] P. Jedlovszky, A. Vincze, and G. Horvai, “New insight into the orientational order of water molecules at the water/1,2-dichloroethane interface: A Monte Carlo simulation study,” *J. Chem. Phys.*, vol. 117, no. 5, pp. 2271–2280, 2002.
- [55] P. Jedlovszky and M. Mezei, “Orientational Order of the Water Molecules Across a Fully Hydrated DMPC Bilayer: A Monte Carlo Simulation Study,” *J. Phys. Chem. B*, vol. 105, no. 17, pp. 3614–3623, 2001.
- [56] M. Szóri, M. Roeselová, and P. Jedlovszky, “Surface hydrophilicity-dependent water adsorption on mixed self-assembled monolayers of C7-CH<sub>3</sub> and C7-COOH residues. A grand canonical monte carlo simulation study,” *J. Phys. Chem. C*, vol. 115, no. 39, pp. 19165–19177, 2011.
- [57] C. G. Mayne *et al.*, “The cellular membrane as a mediator for small molecule interaction with membrane proteins,” *Biochim. Biophys. Acta - Biomembr.*, vol. 1858, no. 10, pp. 2290–2304, 2016.
- [58] J. F. Nagle, R. Zhang, S. Tristram-Nagle, W. Sun, H. I. Petrache, and R. M. Suter, “X-ray structure determination of fully hydrated L $\alpha$  phase dipalmitoylphosphatidylcholine bilayers.,” *Biophys. J.*, vol. 70, no. 3, pp. 1419–1431, Mar. 1996.
- [59] J. F. Nagle, “Area/lipid of bilayers from NMR,” *Biophys. J.*, vol. 64, no. 5, pp. 1476–1481, 1993.
- [60] J. F. Nagle and S. Tristram-Nagle, “Structure of lipid bilayers,” *Biochim Biophys Acta.*, vol.

- 1469, no. 3, pp. 159–195, 2000.
- [61] J. B. Klauda, N. V. Eldho, K. Gawrisch, B. R. Brooks, and R. W. Pastor, “Collective and noncollective models of NMR relaxation in lipid vesicles and multilayers,” *J. Phys. Chem. B*, vol. 112, no. 19, pp. 5924–5929, 2008.
- [62] J. B. Klauda, M. F. Roberts, A. G. Redfield, B. R. Brooks, and R. W. Pastor, “Rotation of Lipids in Membranes: Molecular Dynamics Simulation, <sup>31</sup>P Spin-Lattice Relaxation, and Rigid-Body Dynamics,” *Biophys. J.*, vol. 94, no. 8, pp. 3074–3083, 2008.
- [63] T. Ishiyama, D. Terada, and A. Morita, “Hydrogen-Bonding Structure at Zwitterionic Lipid/Water Interface,” *J. Phys. Chem. Lett.*, vol. 7, no. 2, pp. 216–220, 2016.
- [64] J. Ando *et al.*, “Sphingomyelin distribution in lipid rafts of artificial monolayer membranes visualized by Raman microscopy,” *Proc. Natl. Acad. Sci.*, vol. 112, no. 15, pp. 4558–4563, 2015.
- [65] J. B. Klauda, N. Kučerka, B. R. Brooks, R. W. Pastor, and J. F. Nagle, “Simulation-based methods for interpreting x-ray data from lipid bilayers,” *Biophys. J.*, vol. 90, no. 8, pp. 2796–2807, 2006.
- [66] K. N. Timmis, T. J. McGenity, J. R. van der Meer, and V. de Lorenzo, Eds., *Handbook of Hydrocarbon and Lipid Microbiology*. Springer-Verlag Berlin Heidelberg, 2010.
- [67] E. Egberts, S. J. Marrink, and H. J. Berendsen, “Molecular dynamics simulation of a phospholipid membrane,” *Eur. Biophys. J.*, vol. 22, pp. 423–436, 1994.
- [68] H. Helmut, S. Michael, and S. Klaus, “Molecular Dynamics Simulation of a Bilayer of 200 Lipids in the Gel and in the Liquid-Crystal Phases,” *J. Chem. Phys.*, vol. 97, pp. 8343–8360, 1993.
- [69] E. Egberts and H. J. C. Berendsen, “Molecular dynamics simulation of a smectic liquid crystal with atomic detail,” *J. Chem. Phys.*, vol. 89, no. 6, pp. 3718–3732, 1988.
- [70] M. L. Berkowitz and K. Raghavan, “Computer Simulation of a Water/Membrane Interface,” *Langmuir*, vol. 7, no. 6, pp. 1042–1044, 1991.
- [71] U. Essmann and M. L. Berkowitz, “Dynamical properties of phospholipid bilayers from computer simulation,” *Biophys. J.*, vol. 76, no. 4, pp. 2081–2089, 1999.
- [72] J. B. Klauda *et al.*, “Update of the CHARMM All-Atom Additive Force Field for Lipids: Validation on Six Lipid Types,” *J. Phys. Chem. B*, vol. 114, no. 23, pp. 7830–7843, Jun. 2010.
- [73] S. Feller and A. MacKerell, “An improved empirical potential energy function for molecular simulations of phospholipids,” *J. Phys. Chem. B*, pp. 7510–7515, 2000.
- [74] A. M. Smondyrev and M. L. Berkowitz, “Molecular dynamics study of Sn-1 and Sn-2 chain conformations in dipalmitoylphosphatidylcholine membranes,” *J. Chem. Phys.*, vol. 110, no. 8, pp. 3981–3985, 1999.
- [75] R. W. Benz, F. Castro-Román, D. J. Tobias, and S. H. White, “Experimental validation of molecular dynamics simulations of lipid bilayers: A new approach,” *Biophys. J.*, vol. 88, no. 2, pp. 805–817, 2005.
- [76] E. Lindahl and O. Edholm, “Mesoscopic Undulations and Thickness Fluctuations in Lipid Bilayers from Molecular Dynamics Simulations,” *Biophys. J.*, vol. 79, no. 1, pp. 426–433, 2000.
- [77] S. E. Feller and R. W. Pastor, “Constant surface tension simulations of lipid bilayers: The sensitivity of surface areas and compressibilities,” *J. Chem. Phys.*, vol. 111, no. 3, pp. 1281–1287, 1999.
- [78] C. J. Dickson *et al.*, “Lipid14: The Amber Lipid Force Field,” *J. Chem. Theory Comput.*, vol. 10, no. 2, pp. 865–879, 2014.
- [79] M. J. Abraham *et al.*, “Gromacs: High performance molecular simulations through multi-level parallelism from laptops to supercomputers,” *SoftwareX*, vol. 1–2, pp. 19–25, 2015.
- [80] Y. Zhang, V. Lukacova, V. Bartus, and S. Balaz, “Structural Determinants of Binding of Aromates to Extracellular Matrix: A Multi-Species Multi-Mode CoMFA Study,” *Chem. Res.*

- Toxicol.*, vol. 20, no. 1, pp. 11–19, 2007.
- [81] C. Hanneschlaeger, A. Horner, and P. Pohl, “Intrinsic Membrane Permeability to Small Molecules,” *Chem. Rev.*, vol. 119, no. 9, pp. 5922–5953, 2019.
- [82] M. Orsi, W. E. Sanderson, and J. W. Essex, “Permeability of small molecules through a lipid bilayer: A multiscale simulation study,” *J. Phys. Chem. B*, vol. 113, no. 35, pp. 12019–12029, 2009.
- [83] D. Bemporad, J. W. Essex, and C. Luttmann, “Permeation of Small Molecules Through a Lipid Bilayer: A Computer Simulation Study,” *J. Phys. Chem. B*, vol. 108, no. 15, pp. 4875–4884, 2004.
- [84] M. Palanciová, K. Berka, and M. Otyepka, “Convergence of Free Energy Profile of Coumarin in Lipid Bilayer,” *J. Chem. Theory Comput.*, vol. 8, no. 4, pp. 1200–1211, 2012.
- [85] S.-J. Marrink and H. J. C. Berendsen, “Simulation of water transport through a lipid membrane,” *J. Phys. Chem.*, vol. 98, no. 15, pp. 4155–4168, 1994.
- [86] A. Missner and P. Pohl, “110 years of the Meyer-Overton rule: Predicting membrane permeability of gases and other small compounds,” *ChemPhysChem*, vol. 10, no. 9–10, pp. 1405–1414, 2009.
- [87] C. Martinotti, L. Ruiz-Perez, E. Deplazes, and R. L. Mancera, “Molecular dynamics simulation of the interaction of small molecules with biological membranes,” *ChemPhysChem*, vol. 21, no. 14, pp. 1486–1514, 2020.
- [88] J. Seelig, “Thermodynamics of lipid – peptide interactions,” *Biochim. Biophys. Acta*, vol. 1666, pp. 40–50, 2004.
- [89] G. H. Goetz, M. Shalaeva, G. Caron, G. Ermondi, and L. Philippe, “Relationship between passive permeability and molecular polarity using block relevance analysis,” *Mol. Pharm.*, vol. 14, no. 2, pp. 386–393, 2017.
- [90] C. A. Lipinski, F. Lombardo, B. W. Dominy, and P. J. Feeney, “Experimental and computational approaches to estimate solubility and permeability in drug discovery and development settings,” *Adv. Drug Deliv. Rev.*, vol. 23, no. 1–3, pp. 3–25, Jan. 1997.
- [91] C. M. Chagas, S. Moss, and L. Alisaraie, “Drug metabolites and their effects on the development of adverse reactions: Revisiting Lipinski’s Rule of Five,” *Int. J. Pharm.*, vol. 549, no. 1–2, pp. 133–149, 2018.
- [92] C. A. Lipinski, “Drug-like properties and the causes of poor solubility and poor permeability,” *J. Pharmacol. Toxicol. Methods*, vol. 44, no. 1, pp. 235–249, 2000.
- [93] C. Peetla, A. Stine, and V. Labhsetwar, “Biophysical interactions with model lipid membranes: applications in drug discovery and drug delivery,” *Mol. Pharm.*, vol. 6, no. 5, pp. 1264–1276, 2009.
- [94] T. Oka, M. Hasan, M. Z. Islam, M. Moniruzzaman, and M. Yamazaki, “Low-pH-Induced Lamellar to Bicontinuous Primitive Cubic Phase Transition in Dioleoylphosphatidylserine/Monoolein Membranes,” *Langmuir*, vol. 33, no. 43, pp. 12487–12496, Oct. 2017.
- [95] H. Heerklotz, “The microcalorimetry of lipid membranes,” *J. Phys. Condens. Matter*, vol. 16, no. 15, pp. R441–R467, Apr. 2004.
- [96] T. Devanand, S. Krishnaswamy, and · Satyavani Vemparala, “Interdigitation of Lipids Induced by Membrane-Active Proteins,” *J. Membr. Biol.*, vol. 252, no. 3, pp. 331–342, 2019.
- [97] L. Löbbecke and G. Cevc, “Effects of short-chain alcohols on the phase behavior and interdigitation of phosphatidylcholine bilayer membranes,” *BBA - Biomembr.*, vol. 1237, no. 1, pp. 59–69, 1995.
- [98] A. L. Parrill and K. B. Lipkowitz, *Reviews in Computational Chemistry 28*. New Jersey: John Wiley & Sons, 2015.
- [99] S. Moradi and M. Shahlaei, “Shedding light on the structural properties of lipid bilayers using molecular dynamics simulation: a review study,” *RSC Adv.*, vol. 9, pp. 4644–4658, 2019.

- [100] P. Larsson, L. C. Alskär, and C. A. S. Bergström, “Molecular Structuring and Phase Transition of Lipid-Based Formulations upon Water Dispersion: A Coarse-Grained Molecular Dynamics Simulation Approach,” *Mol. Pharm.*, vol. 14, no. 12, pp. 4145–4153, 2017.
- [101] R. Gupta and B. Rai, “Molecular Dynamics Simulation Study of Skin Lipids: Effects of the Molar Ratio of Individual Components over a Wide Temperature Range,” *J. Phys. Chem. B*, vol. 119, no. 35, pp. 11643–11655, 2015.
- [102] T. Schindler, D. Kröner, and M. O. Steinhauser, “On the dynamics of molecular self-assembly and the structural analysis of bilayer membranes using coarse-grained molecular dynamics simulations,” *Biochim. Biophys. Acta - Biomembr.*, vol. 1858, no. 9, pp. 1955–1963, 2016.
- [103] Å. A. Skjerveik *et al.*, “Simulation of lipid bilayer self-assembly using all-atom lipid force fields,” *Phys. Chem. Chem. Phys.*, vol. 18, no. 15, pp. 10573–10584, 2016.
- [104] R. Friedman, “Membrane–Ion Interactions,” *J. Membr. Biol.*, vol. 251, no. 3, pp. 453–460, 2018.
- [105] A. Nowroozi and M. Shahlaei, “A coupling of homology modeling with multiple molecular dynamics simulation for identifying representative conformation of GPCR structures: a case study on human bombesin receptor subtype-3,” *J. Biomol. Struct. Dyn.*, vol. 35, no. 2, pp. 250–272, 2017.
- [106] K. R. Pothula, C. J. F. Solano, and U. Kleinekathöfer, “Simulations of outer membrane channels and their permeability,” *Biochim. Biophys. Acta - Biomembr.*, vol. 1858, no. 7, pp. 1760–1771, 2016.
- [107] N. Pokhrel and L. Maibaum, “Free Energy Calculations of Membrane Permeation: Challenges Due to Strong Headgroup-Solute Interactions,” *J. Chem. Theory Comput.*, vol. 14, p. 1762–1771, 2018.
- [108] G. Hantal, B. Fábrián, M. Sega, B. Jójárt, and P. Jedlovszky, “Effect of general anesthetics on the properties of lipid membranes of various compositions,” *Biochim. Biophys. Acta - Biomembr.*, vol. 1861, no. 3, pp. 594–609, 2019.
- [109] M. Lundborg, C. L. Wennberg, A. Narangifard, E. Lindahl, and L. Norlén, “Predicting drug permeability through skin using molecular dynamics simulation,” *J. Control. Release*, vol. 283, no. April, pp. 269–279, 2018.
- [110] C. T. Lee *et al.*, “Simulation-Based Approaches for Determining Membrane Permeability of Small Compounds,” *J. Chem. Inf. Model.*, vol. 56, no. 4, pp. 721–733, 2016.
- [111] B. Fabian, M. Darvas, S. Picaud, M. Sega, and P. Jedlovszky, “The effect of anaesthetics on the properties of a lipid membrane in the biologically relevant phase: a computer simulation study,” *Phys. Chem. Chem. Phys.*, vol. 17, no. 22, pp. 14750–14760, 2015.
- [112] P. Jedlovszky and M. Mezei, “Calculation of the Free Energy Profile of H<sub>2</sub>O, O<sub>2</sub>, CO, CO<sub>2</sub>, NO, and CHCl<sub>3</sub> in a Lipid Bilayer with a Cavity Insertion Variant of the Widom Method,” *J. Am. Chem. Soc.*, vol. 122, no. 5, pp. 5125–5131, 2000.
- [113] P. V. Klimovich, M. R. Shirts, and D. L. Mobley, “Guidelines for the analysis of free energy calculations,” *J. Comput. Aided Mol. Des.*, vol. 29, no. 5, pp. 397–411, 2015.
- [114] N. Hansen and W. F. Van Gunsteren, “Practical Aspects of Free-Energy Calculations: A Review,” *J. Chem. Theory Comput.*, vol. 10, no. 7, pp. 2632–2647, 2014.
- [115] D. Meral, D. Provasi, and M. Filizola, “An efficient strategy to estimate thermodynamics and kinetics of G protein-coupled receptor activation using metadynamics and maximum caliber,” *J. Chem. Phys.*, vol. 149, no. 22, p. 224101, 2018.
- [116] G. Torrie and J. Valleau, “Nonphysical Sampling Distributions in Monte Carlo Free-Energy Estimation: Umbrella Sampling,” *J. Comput. Phys.*, vol. 23, pp. 187–199, 1977.
- [117] B. M. Dickson, T. Lelie, G. Stoltz, P. Fleurat-lessard, and N. Supe, “Free Energy Calculations : An Efficient Adaptive Biasing Potential Method,” *J. Phys. Chem. B*, vol. 114, pp. 5823–5830, 2010.
- [118] J. G. Kirkwood, “Statistical Mechanics of Fluid Mixtures,” *J. Chem. Phys.*, vol. 3, pp. 300–

- 313, 1935.
- [119] J. Vymetal and J. Vondrásek, "Metadynamics As a Tool for Mapping the Conformational and Free-Energy Space of Peptides - The Alanine Dipeptide Case Study," *J. Phys. Chem. B*, vol. 114, no. 16, pp. 5632–5642, 2010.
- [120] A. Laio and M. Parrinello, "Escaping free-energy minima," *PNAS*, vol. 99, no. 20, pp. 12562–12566, 2002.
- [121] A. Barducci, G. Bussi, and M. Parrinello, "Well-Tempered Metadynamics: A Smoothly Converging and Tunable Free-Energy Method," *Phys. Rev. Lett.*, vol. 100, no. 2, p. 020603, 2008.
- [122] M. Orsi and J. W. Essex, "Permeability of drugs and hormones through a lipid bilayer: insights from dual-resolution molecular dynamics," *Soft Matter*, vol. 6, no. 16, pp. 3797–3808, 2010.
- [123] M. Brinkmann *et al.*, "Ecotoxicity of Nitrogen, Sulfur, or Oxygen Heterocycles and Short-Chained Alkyl Phenols Commonly Detected in Contaminated Groundwater," *Environ. Toxicol. Chem.*, vol. 38, no. 6, pp. 1343–1355, 2019.
- [124] J. Blotevogel, A.-K. Reineke, J. Hollender, and T. Held, "Identifikation NSO-heterocyclischer Prioritäts-substanzen zur Erkundung und Überwachung Teeröl-kontaminierter Standorte," *Grundwasser*, vol. 13, no. 3, pp. 147–157, Sep. 2008.
- [125] D. Zamfirescu and P. Grathwohl, "Occurrence and attenuation of specific organic compounds in the groundwater plume at a former gasworks site," *J. Contam. Hydrol.*, vol. 53, no. 3–4, pp. 407–427, 2001.
- [126] E. P. Kuhn and J. M. Suflita, "Microbial degradation of nitrogen, oxygen and sulfur heterocyclic compounds under anaerobic conditions: Studies with aquifer samples," *Environ. Toxicol. Chem.*, vol. 8, no. 12, pp. 1149–1158, 1989.
- [127] J. Sikkema, J. A. de Bont, and B. Poolman, "Interactions of cyclic hydrocarbons with biological membranes.," *J. Biol. Chem.*, vol. 269, no. 11, pp. 8022–8028, Mar. 1994.
- [128] J. Sikkema, J. A. de Bont, and B. Poolman, "Mechanisms of membrane toxicity of hydrocarbons.," *Microbiol. Rev.*, vol. 59, no. 2, pp. 201–22, Jun. 1995.
- [129] M. J. De Smet, K. Jaap, and B. Witholt, "The effect of toluene on the structure and permeability of the outer and cytoplasmic membranes of escherichia coli," *Biochim. Biophys. Acta - Biomembr.*, vol. 506, no. 1, pp. 64–80, 1978.
- [130] S. Uribe, P. Rangel, G. Espinola, and G. Aguirre, "Effects of cyclohexane, an industrial solvent, on the yeast *Saccharomyces cerevisiae* and on isolated yeast mitochondria," *Appl. Environ. Microbiol.*, vol. 56, no. 7, pp. 2114–2119, 1990.
- [131] S. Uribe, J. Ramirez, and A. Pena, "Effects of  $\beta$ -pinene on yeast membrane functions," *J. Bacteriol.*, vol. 161, no. 3, pp. 1195–1200, 1985.
- [132] A. Raz and A. Livne, "Differential effects of lipids on the osmotic fragility of erythrocytes," *BBA - Biomembr.*, vol. 311, no. 2, pp. 222–229, 1973.
- [133] P. Seeman, "The membrane actions of anesthetics and tranquilizers.," *Pharmacol. Rev.*, vol. 24, no. 4, pp. 583–655, Dec. 1972.
- [134] M. S. I. Shaikh, N. D. Derle, and R. Bhamber, "Permeability enhancement techniques for poorly permeable drugs: A review," *J. Appl. Pharm. Sci.*, vol. 2, no. 7, pp. 34–39, 2012.
- [135] L. Yang, H. Zhang, M. Mikov, and I. G. Tucker, "Physicochemical and Biological Characterization of Monoketocholic Acid , a Novel Permeability Enhancer," *Mol. Pharm.*, vol. 6, no. 2, pp. 445–456, 2009.
- [136] A. A. Gurtovenko, J. Anwar, and W. Yorkshire, "Modulating the Structure and Properties of Cell Membranes : The Molecular Mechanism of Action of Dimethyl Sulfoxide," *J. Phys. Chem. B*, vol. 111, pp. 10453–10460, 2007.
- [137] S. Peddinghaus *et al.*, "Quantitative assessment of the embryotoxic potential of NSO-heterocyclic compounds using zebrafish (*Danio rerio*)," *Reprod. Toxicol.*, vol. 33, no. 2, pp.

224–232, 2012.

- [138] L. Robbiano, D. Baroni, R. Carrozzino, E. Mereto, and G. Brambilla, “DNA damage and micronuclei induced in rat and human kidney cells by six chemicals carcinogenic to the rat kidney,” *Toxicology*, vol. 204, no. 2–3, pp. 187–195, 2004.
- [139] National Center for Biotechnology And Information, “PubChem.” [Online]. Available: <https://pubchem.ncbi.nlm.nih.gov/>. [Accessed: 10-May-2019].
- [140] S. Soundararajan and S. V. Anantkrishnan, “Dipole moments of tetrahydropyran and dihydropyran,” *Proc. Indian Acad. Sci. - Sect. A*, vol. 37, no. 4, pp. 578–583, 1953.
- [141] J. R. Partington and D. I. Coomber, “Dipole Moment and Structure of Morpholine,” *Nature*, vol. 141, no. 3577, p. 918, 1938.
- [142] J. S. Kim, “Production, separation and applications of phenolic-rich bio-oil - A review,” *Bioresour. Technol.*, vol. 178, pp. 90–98, 2015.
- [143] D. Duan *et al.*, “Renewable phenol production from lignin with acid pretreatment and ex-situ catalytic pyrolysis,” *J. Clean. Prod.*, vol. 231, pp. 331–340, 2019.
- [144] S. H. Lin and R. S. Juang, “Adsorption of phenol and its derivatives from water using synthetic resins and low-cost natural adsorbents: A review,” *J. Environ. Manage.*, vol. 90, no. 3, pp. 1336–1349, 2009.
- [145] C. G. Lee, S. H. Hong, S. G. Hong, J. W. Choi, and S. J. Park, “Production of Biochar from Food Waste and its Application for Phenol Removal from Aqueous Solution,” *Water. Air. Soil Pollut.*, vol. 230, no. 3, 2019.
- [146] Z. Zhang, K. Li, S. Ma, M. Cui, Q. Lu, and Y. Yang, “Fast pyrolysis of biomass catalyzed by magnetic solid base catalyst in a hydrogen atmosphere for selective production of phenol,” *Ind. Crops Prod.*, vol. 137, no. April, pp. 495–500, 2019.
- [147] A. Akyol, B. Samuk, M. Kobya, and E. Demirbas, “Treatment of phenol formaldehyde production wastewater by electrooxidation-electrofenton successive processes,” *Sep. Sci. Technol.*, vol. 55, no. 15, pp. 2830–2843, 2020.
- [148] European Chemicals Bureau, “European Union Risk Assessment Report On Phenol,” Germany, 2006.
- [149] B. R. Giri, F. Khaled, M. Szori, B. Viskolcz, and A. Farooq, “An experimental and theoretical kinetic study of the reaction of OH radicals with tetrahydrofuran,” *Proc. Combust. Inst.*, vol. 36, no. 1, pp. 143–150, Jan. 2017.
- [150] F. Zhang *et al.*, “Synthesis of Tetrahydropyran from Tetrahydrofurfuryl Alcohol over Cu – ZnO / Al<sub>2</sub>O<sub>3</sub> under a Gaseous-Phase Condition,” *Catalysts*, vol. 8, no. 105, pp. 1–11, 2018.
- [151] S. Gruet, O. Pirali, A. L. Steber, and M. Schnell, “The structural determination and skeletal ring modes of tetrahydropyran,” *Phys. Chem. Chem. Phys.*, vol. 12, no. 1975, 2019.
- [152] B. Rotavera *et al.*, “Influence of oxygenation in cyclic hydrocarbons on chain-termination reactions from R + O<sub>2</sub>: Tetrahydropyran and cyclohexane,” *Proc. Combust. Inst.*, vol. 36, no. 1, pp. 597–606, 2017.
- [153] L. S. Tran *et al.*, “Pyrolysis and combustion chemistry of tetrahydropyran: Experimental and modeling study,” *Combust. Flame*, vol. 162, no. 11, pp. 4283–4303, 2015.
- [154] V. K. Sharma, S. Malik, and S. Solanki, “Thermodynamic Studies of Molecular Interactions in Mixtures Containing Tetrahydropyran, 1,4-Dioxane, and Cyclic Ketones,” *J. Chem. Eng. Data*, vol. 62, no. 2, pp. 623–632, 2017.
- [155] N. M. Nasir, K. Ermanis, and P. A. Clarke, “Strategies for the construction of tetrahydropyran rings in the synthesis of natural products,” *Org. Biomol. Chem.*, vol. 12, no. 21, pp. 3323–3335, 2014.
- [156] M. J. Zenker, R. C. Borden, and M. A. Barlaz, “Occurrence and Treatment of 1,4-Dioxane in Aqueous Environments,” *Environ. Eng. Sci.*, vol. 20, no. 5, pp. 423–432, Sep. 2003.
- [157] Agency for Toxic Substances & Disease Registry, “Toxicological profile for 1,4-dioxane,” 2012. [Online]. Available: <https://www.atsdr.cdc.gov/toxprofiles/tp.asp?id=955&tid=199>.

[Accessed: 04-Apr-2019].

- [158] U. Karges, J. Becker, and W. Püttmann, "1,4-Dioxane pollution at contaminated groundwater sites in western Germany and its distribution within a TCE plume," *Sci. Total Environ.*, vol. 619–620, pp. 712–720, 2018.
- [159] S. D. Richardson and T. A. Ternes, "Water Analysis: Emerging Contaminants and Current Issues," *Anal. Chem.*, vol. 83, no. 12, pp. 4614–4648, Jun. 2011.
- [160] Institute for Health and Consumer Protection, "European Union Risk Assessment Report: 1,4-dioxane," European Communities, 2002.
- [161] R. D. Harrison, D. J. Marino, C. C. Conaway, L. F. Rubin, and J. Gandy, "Chronic morpholine exposure of rats," *Toxicol. Sci.*, vol. 12, no. 3, pp. 491–507, 1989.
- [162] R. Kumar, "Health effects of morpholine based coating for fruits and vegetables," *Int. J. Med. Res. Heal. Sci.*, vol. 5, no. 9, pp. 32–38, 2016.
- [163] P. Cao *et al.*, "Concentration of morpholine residues in major fruits and juices and its dietary exposure in China," *Food Addit. Contam. - Part A Chem. Anal. Control. Expo. Risk Assess.*, vol. 36, no. 1, pp. 26–34, 2019.
- [164] P. Besse *et al.*, "Degradation of morpholine and thiomorpholine by an environmental Mycobacterium involves a cytochrome P450. Direct evidence of intermediates by in situ 1H NMR," *J. Mol. Catal. - B Enzym.*, vol. 5, no. 1–4, pp. 403–409, 1998.
- [165] M. M. Aly, "Degradation of morpholine by Mycobacterium sp. Isolated from contaminated wastewater collected from Egypt," *African J. Biotechnol.*, vol. 10, no. 42, pp. 8351–8358, 2011.
- [166] W. D. Di Marzio, M. Sáenz, J. Alberdi, M. Tortorelli, and G. Silvana, "Risk assessment of domestic and industrial effluents unloaded into a freshwater environment," *Ecotoxicol. Environ. Saf.*, vol. 61, no. 3, pp. 380–391, 2005.
- [167] A. Swain, K. V. Waterhouse, W. A. Venables, A. G. Calley, and S. E. Lowe, "Biochemical studies of morpholine catabolism by an environmental mycobacterium," *Appl. Microbiol. Biotechnol.*, vol. 35, no. 1, pp. 110–114, 1991.
- [168] T. Sakakura, J. C. Choi, and H. Yasuda, "Transformation of carbon dioxide," *Chem. Rev.*, vol. 107, no. 6, pp. 2365–2387, 2007.
- [169] X. L. L. He, "Synthesis of Lactones and Other Heterocycles," *Top. Curr. Chem.*, vol. 375, no. 2, pp. 1–32, 2017.
- [170] M. Liu, Y. Sun, Y. Liang, and B. Lin, "Highly Efficient Synthesis of Functionalizable Polymers from a CO<sub>2</sub> / 1,3-Butadiene-Derived Lactone," *ACS Macro Lett.*, vol. 6, pp. 1373–1378, 2017.
- [171] S. Zhang and Z. Liu, "Advances in the biological fixation of carbon dioxide by microalgae," *J. Chem. Technol. Biotechnol.*, vol. 96, no. 6, pp. 1475–1495, 2021.
- [172] R. Dalpozzo, N. Della Ca', B. Gabriele, and R. Mancuso, "Recent Advances in the Chemical Fixation of Carbon Dioxide: A Green Route to Carbonylated Heterocycle Synthesis," *Catalysts*, vol. 9, no. 6, p. 511, 2019.
- [173] C. Chien Truong and D. Kumar Mishra, "Catalyst-free fixation of carbon dioxide into value-added chemicals: a review," *Environ. Chem. Lett.*, vol. 19, pp. 911–940, 2021.
- [174] P. Braunstein, D. Matt, and D. Nobel, "Carbon Dioxide Activation and Catalytic Lactone Synthesis by Telomerization of Butadiene and CO<sub>2</sub>," *J. Am. Chem. Soc.*, vol. 110, no. 10, pp. 3207–3212, 1988.
- [175] L. Chen, Y. Li, S. Yue, J. Ling, X. Ni, and Z. Shen, "Chemoselective RAFT Polymerization of a Trivinyl Monomer Derived from Carbon Dioxide and 1,3-Butadiene: From Linear to Hyperbranched," *Macromolecules*, vol. 50, no. 24, pp. 9598–9606, 2017.
- [176] M. Aresta, A. Dibenedetto, and A. Angelini, "Catalysis for the Valorization of Exhaust Carbon: from CO<sub>2</sub> to Chemicals, Materials, and Fuels. Technological Use of CO<sub>2</sub>," *Chem. Rev.*, vol. 114, no. 3, pp. 1709–1742, Feb. 2014.

- [177] Y. Niu and H. Li, "Alternating copolymerization of carbon dioxide and cyclohexene oxide catalyzed by salen CoIII(acetate) complexes," *Colloid Polym. Sci.*, vol. 291, no. 9, pp. 2181–2189, 2013.
- [178] Y. C. Xu, H. Zhou, X. Y. Sun, W. M. Ren, and X. B. Lu, "Crystalline Polyesters from CO<sub>2</sub> and 2-Butyne via  $\alpha$ -Methylene- $\beta$ -butyrolactone Intermediate," *Macromolecules*, vol. 49, no. 16, pp. 5782–5787, 2016.
- [179] R. Nakano, S. Ito, and K. Nozaki, "Copolymerization of carbon dioxide and butadiene via a lactone intermediate," *Nat. Chem.*, vol. 6, no. 4, pp. 325–331, 2014.
- [180] B. Walker and L. D. Stokes, "Synthetic Polymers-Olefin, Diene Elastomers, and Vinyl Halides," in *Patty's Toxicology*, vol. 4, Hoboken, NJ, USA: John Wiley & Sons, Inc., 2012, pp. 891–916.
- [181] P. D. Hustad, "Frontiers in olefin polymerization: Reinventing the world's most common synthetic polymers," *Science (80-. )*, vol. 325, no. 5941, pp. 704–707, 2009.
- [182] M. L. Lejkowski *et al.*, "The first catalytic synthesis of an acrylate from CO<sub>2</sub> and an alkene-A rational approach," *Chem. - A Eur. J.*, vol. 18, no. 44, pp. 14017–14025, 2012.
- [183] J. Takaya, K. Sasano, and N. Iwasawa, "Efficient one-to-one coupling of easily available 1,3-dienes with carbon dioxide," *Org. Lett.*, vol. 13, no. 7, pp. 1698–1701, 2011.
- [184] K. Soga, S. Hosoda, and S. Ikeda, "Copolymerization of carbon dioxide and some diene compounds," *Die Makromol. Chemie*, vol. 176, no. 6, pp. 1907–1911, 1975.
- [185] K. Soga, M. Sato, S. Hosoda, and S. Ikeda, "Copolymerization of methyl vinyl ether and carbon dioxide," *J. Polym. Sci. Polym. Lett. Ed.*, vol. 13, no. 9, pp. 543–548, Sep. 1975.
- [186] C. J. Price, B. J. E. Reich, and S. A. Miller, "Thermodynamic and Kinetic Considerations in the Copolymerization of Ethylene and Carbon Dioxide," *Macromolecules*, vol. 39, no. 8, pp. 2751–2756, 2006.
- [187] O. Robles-Vásquez *et al.*, "Microemulsion polymerization of 1,3-butadiene'," *Polym. Bull.*, vol. 66, pp. 341–349, 2011.
- [188] F. Jing *et al.*, "Direct dehydration of 1,3-butanediol into butadiene over aluminosilicate catalysts," *Catal. Sci. Technol.*, vol. 6, pp. 5830–5840, 2016.
- [189] C. Pinel, P. Fuertes, and C. Petitjean, "Aqueous-Phase Hydrogenation of Biomass-Based Succinic Acid to 1,4-Butanediol Over Supported Bimetallic Catalysts," *Top. Catal.*, vol. 53, pp. 1270–1273, 2010.
- [190] Y. Sasaki, Y. Inoue, and H. Hashimoto, "Reaction of carbon dioxide with butadiene catalysed by palladium complexes. Synthesis of 2-ethylidenehept-5-en-4-olide," *J. Chem. Soc. Chem. Commun.*, no. 15, pp. 605–606, 1976.
- [191] L. Chen, J. Ling, X. Ni, and Z. Shen, "Synthesis and Properties of Networks Based on Thiolene Chemistry Using a CO<sub>2</sub>-Based  $\delta$ -Lactone," *Macromol. Rapid Commun.*, vol. 39, no. 23, pp. 1–6, 2018.
- [192] A. Behr and G. Henze, "Use of carbon dioxide in chemical syntheses via a lactone intermediate," *Green Chem.*, vol. 13, no. 1, pp. 25–39, 2011.
- [193] A. Behr, P. Bahke, B. Klinger, and M. Becker, "Application of carbonate solvents in the telomerisation of butadiene with carbon dioxide," *J. Mol. Catal. A Chem.*, vol. 267, no. 1–2, pp. 149–156, 2007.
- [194] A. Behr and M. Becker, "The telomerisation of 1,3-butadiene and carbon dioxide: process development and optimisation in a continuous miniplant," *Dalt. Trans.*, vol. Oct, no. 38, pp. 4607–4613, 2006.
- [195] developed by ChemAxon ([www.chemaxon.com](http://www.chemaxon.com)), "Chemicalize." [Online]. Available: <https://chemicalize.com/>. [Accessed: 22-Feb-2021].
- [196] Advanced Chemistry Development Inc Toronto. ON. Canada, "ACD/Labs Percepta Platform - PhysChem Module," 2021. [Online]. Available: [www.acdlabs.com](http://www.acdlabs.com). [Accessed: 22-Feb-2021].

- [197] M. J. Frisch *et al.*, “Gaussian09.” Wallingford CT., 2009.
- [198] A. Becke, “Density Functional Thermochemistry III The Role of Exact Exchange,” *J. Chem. Phys.*, vol. 98, pp. 5648–5652, 1993.
- [199] C. Lee, W. Yang, and R. G. Parr, “Development of the Colle-Salvetti correlation-energy formula into a functional of the electron density,” *Phys Rev B Condens Matter*, vol. 37, no. 2, pp. 785–789, 1988.
- [200] R. K. Henderson *et al.*, “Green Chemistry Expanding GSK’s solvent selection guide – embedding sustainability into solvent selection starting at medicinal chemistry,” *Green Chem.*, vol. 13, pp. 854–862, 2011.
- [201] C. P. Aschcroft, P. J. Dunn, J. D. Hayler, and A. S. Wells, “Survey of Solvent Usage in Papers Published in Organic Process Research and Development 1997-2012 .,” *Org. Process Res. Dev.*, vol. 19, no. 7, pp. 740–747, 2014.
- [202] S. Abou-Shehada, J. H. Clark, G. Paggiola, and J. Sherwood, “Tunable solvents: Shades of green,” *Chem. Eng. Process. Process Intensif.*, vol. 99, pp. 88–96, 2016.
- [203] P. F. McMillan and H. E. Stanley, “Fluid phases: Going supercritical,” *Nat. Phys.*, vol. 6, no. 7, pp. 479–480, 2010.
- [204] C. A. Eckert, B. L. Knutson, and P. G. Debenedetti, “Supercritical fluids as solvents for chemical and materials processing,” *Nature*, vol. 383, no. 6598, pp. 313–318, 1996.
- [205] P. F. F. da S. Rui, T. A. P. Rocha-santos, and A. C. Duarte, “Supercritical fluid extraction of bioactive compounds,” *Trends Anal. Chem.*, vol. 76, pp. 40–51, 2016.
- [206] I. Skarmoutsos and E. Guardia, “Local Structural Effects and Related Dynamics in Supercritical Ethanol . 2. Hydrogen-Bonding Network and Its Effect on Single Reorientational Dynamics,” *J. Phys. Chem. B*, vol. 113, pp. 8898–8910, 2009.
- [207] M. C. Bubalo, S. Vidovic, I. R. Redovnikovic, and S. Jokic, “Green Solvents for Green Technologies,” *J. Chem. Technol. Comput.*, vol. 90, no. 9, pp. 1631–1639, 2015.
- [208] T. Adschiri and A. Yoko, “Supercritical fluids for nanotechnology,” *J. Supercrit. Fluids*, vol. 134, pp. 167–175, 2018.
- [209] M. Türk and C. Erkey, “Synthesis of supported nanoparticles in supercritical fluids by supercritical fluid reactive deposition: Current state, further perspectives and needs,” *J. Supercrit. Fluids*, vol. 134, pp. 176–183, 2018.
- [210] J. M. Stubbs, “Molecular simulations of supercritical fluid systems,” *J. Supercrit. Fluids*, vol. 108, pp. 104–122, 2016.
- [211] M. Raventós, S. Duarte, and R. Alarcón, “Application and Possibilities of Supercritical CO<sub>2</sub> Extraction in Food Processing Industry: An Overview,” *Food Sci. Technol. Int.*, vol. 8, pp. 269–284, 2002.
- [212] G. D. Smith, R. L. Jaffe, and D. Y. Yoon, “Conformations of 1,2-Dimethoxyethane in the Gas and Liquid Phases from Molecular Dynamics Simulations,” *J. Am. Chem. Soc.*, vol. 117, no. 1, pp. 530–531, 1995.
- [213] D. Paschek, B. Golub, and R. Ludwig, “Hydrogen bonding in a mixture of protic ionic liquids: A molecular dynamics simulation study,” *Phys. Chem. Chem. Phys.*, vol. 17, no. 13, pp. 8431–8440, 2015.
- [214] R. P. Matthews *et al.*, “A structural investigation of ionic liquid mixtures,” *Phys. Chem. Chem. Phys.*, vol. 18, no. 12, pp. 8608–8624, 2016.
- [215] N. Lümme and T. Kraska, “Investigation of the formation of iron nanoparticles from the gas phase by molecular dynamics simulation,” *Nanotechnology*, vol. 15, no. 5, pp. 525–533, 2004.
- [216] R. S. Taylor, L. X. Dang, and B. C. Garrett, “Molecular dynamics simulations of the liquid/vapor interface of SPC/E water,” *J. Phys. Chem.*, vol. 100, no. 28, pp. 11720–11725, 1996.
- [217] J. T. Fern, D. J. Keffer, and W. V. Steele, “Vapor - Liquid equilibrium of ethanol by molecular

- dynamics simulation and voronoi tessellation,” *J. Phys. Chem. B*, vol. 111, no. 46, pp. 13278–13286, 2007.
- [218] S. Patel, W. V. Wilding, and R. L. Rowley, “The use of two-phase molecular dynamics simulations to determine the phase behavior and critical point of propane molecular models,” *J. Chem. Phys.*, vol. 134, no. 2, 2011.
- [219] M. Mecke, J. Winkelmann, and J. Fischer, “Molecular dynamics simulation of the liquid-vapor interface: The Lennard-Jones fluid,” *J. Chem. Phys.*, vol. 107, no. 21, pp. 9264–9270, 1997.
- [220] V. V. Zhakhovskii and S. I. Anisimov, “Molecular-dynamics simulation of evaporation of a liquid,” *J. Exp. Theor. Phys.*, vol. 84, no. 4, pp. 734–745, 1997.
- [221] A. Idrissi, I. Vyalov, N. Georgi, and M. Kiselev, “On the characterization of inhomogeneity of the density distribution in supercritical fluids via molecular dynamics simulation and data mining analysis,” *J. Phys. Chem. B*, vol. 117, no. 40, pp. 12184–12188, 2013.
- [222] J. G. Harris and K. H. Yung, “Carbon dioxide’s liquid-vapor coexistence curve and critical properties as predicted by a simple molecular model,” *J. Phys. Chem.*, vol. 99, no. 31, pp. 12021–12024, 1995.
- [223] J. J. Potoff and J. I. Siepmann, “Vapor–liquid equilibria of mixtures containing alkanes, carbon dioxide, and nitrogen,” *AIChE J.*, vol. 47, no. 7, pp. 1676–1682, Jul. 2001.
- [224] O. A. Moulton, G. A. Orozco, I. N. Tsimpanogiannis, A. Z. Panagiotopoulos, and I. G. Economou, “Atomistic molecular dynamics simulations of H<sub>2</sub>O diffusivity in liquid and supercritical CO<sub>2</sub>,” *Mol. Phys.*, vol. 113, no. 17–18, pp. 2805–2814, Sep. 2015.
- [225] M. A. González, “Force fields and molecular dynamics simulations,” *Collect. SFN*, vol. 12, pp. 169–200, 2011.
- [226] G. Raabe, *Applications and Perspectives Molecular Simulation Studies on Thermophysical Properties With Application to Working Fluids*. Braunschweig: Springer, 2017.
- [227] M. P. Allen, “Introduction to molecular dynamics simulation,” *Comput. Soft Matter From Synth. Polym. to Proteins*, vol. 23, no. 2, pp. 1–28, 2004.
- [228] S. A. Hollingsworth and R. O. Dror, “Molecular Dynamics Simulation for All,” *Neuron*, vol. 99, no. 6, pp. 1129–1143, 2018.
- [229] S. Piana, K. Lindorff-Larsen, and D. E. Shaw, “Atomic-level description of ubiquitin folding,” *Proc. Natl. Acad. Sci. U. S. A.*, vol. 110, no. 15, pp. 5915–20, 2013.
- [230] T. Reddy *et al.*, “Nothing to Sneeze At: A Dynamic and Integrative Computational Model of an Influenza A Virion,” *Structure*, vol. 23, no. 3, pp. 584–597, 2015.
- [231] Y. Shibuta, S. Sakane, E. Miyoshi, S. Okita, T. Takaki, and M. Ohno, “Heterogeneity in homogeneous nucleation from billion-atom molecular dynamics simulation of solidification of pure metal,” *Nat. Commun.*, vol. 8, no. 1, pp. 1–8, 2017.
- [232] N. Nguyen *et al.*, “Modeling in the Time of COVID-19: Statistical and Rule-based Mesoscale Models,” *IEEE Trans. Vis. Comput. Graph.*, vol. 27, no. 2, pp. 722–732, 2021.
- [233] A. Hospital, J. R. Goñi, M. Orozco, and J. Gelpi, “Molecular dynamics simulations: Advances and applications,” *Adv. Appl. Bioinforma. Chem.*, vol. 8, pp. 37–47, 2015.
- [234] U. Essmann, L. Perera, M. L. Berkowitz, T. Darden, H. Lee, and L. G. Pedersen, “A smooth particle mesh Ewald method,” *J. Chem. Phys.*, vol. 103, no. 19, pp. 8577–8593, Nov. 1995.
- [235] R. W. Pastor and A. D. MacKerell, “Development of the CHARMM force field for lipids,” *J. Phys. Chem. Lett.*, vol. 2, no. 13, pp. 1526–1532, 2011.
- [236] J. Kleinjung and F. Fraternali, “Design and application of implicit solvent models in biomolecular simulations,” *Curr. Opin. Struct. Biol.*, vol. 25, pp. 126–134, 2014.
- [237] R. Anandakrishnan, A. Drozdetski, R. C. Walker, and A. V. Onufriev, “Speed of conformational change: Comparing explicit and implicit solvent molecular dynamics simulations,” *Biophys. J.*, vol. 108, no. 5, pp. 1153–1164, 2015.
- [238] H. I. Ingólfsson *et al.*, “The power of coarse graining in biomolecular simulations,” *Wiley*

- Interdiscip. Rev. Comput. Mol. Sci.*, vol. 4, no. 3, pp. 225–248, 2014.
- [239] S. O. Yesylevskyy, L. V. Schäfer, D. Sengupta, and S. J. Marrink, “Polarizable water model for the coarse-grained MARTINI force field,” *PLoS Comput. Biol.*, vol. 6, no. 6, pp. 1–17, 2010.
- [240] R. E. Skyner, J. L. McDonagh, C. R. Groom, T. van Mourik, and J. B. O. Mitchell, “A review of methods for the calculation of solution free energies and the modelling of systems in solution,” *Phys. Chem. Chem. Phys.*, vol. 17, no. 9, pp. 6174–6191, 2015.
- [241] M. W. Mahoney and W. L. Jorgensen, “A five-site model for liquid water and the reproduction of the density anomaly by rigid, nonpolarizable potential functions,” *J. Chem. Phys.*, vol. 112, no. 20, pp. 8910–8922, 2000.
- [242] M. Praprotnik, D. Janezic, and J. Mavri, “Temperature dependence of water vibrational spectrum: A molecular dynamics simulation study,” vol. 108, no. 50, pp. 11056–11062, 2004.
- [243] M. P. Allen and D. J. Tildesley, *Computer simulation of Liquids*, 2nd Editio. Oxford: Oxford Univ. Press, 2017.
- [244] M. Deserno and C. Holm, “How to mesh up Ewald sums. I. a theoretical and numerical comparison of various particle mesh routines,” *J. Chem. Phys.*, vol. 109, no. 18, pp. 7678–7693, 1998.
- [245] J. C. Phillips *et al.*, “Scalable molecular dynamics with NAMD,” *J. Comput. Chem.*, vol. 26, no. 16, pp. 1781–1802, 2005.
- [246] D. A. Case *et al.*, “The Amber biomolecular simulation programs,” *J. Comput. Chem.*, vol. 26, no. 16, pp. 1668–1688, 2005.
- [247] A. R. Leach, “Molecular modelling: principles and applications,” *Culture Ethnicity and Conflict*, no. 2nd. p. 744, 2001.
- [248] W. C. Swope, H. C. Andersen, P. H. Berens, and K. R. Wilson, “A computer simulation method for the calculation of equilibrium constants for the formation of physical clusters of molecules: Application to small water clusters,” *J. Chem. Phys.*, vol. 76, no. 1, pp. 637–649, 1982.
- [249] J. P. Ryckaert, G. Ciccotti, and H. J. C. Berendsen, “Numerical integration of the cartesian equations of motion of a system with constraints: molecular dynamics of n-alkanes,” *J. Comput. Phys.*, vol. 23, no. 3, pp. 327–341, 1977.
- [250] H. C. Andersen, “Rattle: A ‘velocity’ version of the shake algorithm for molecular dynamics calculations,” *J. Comput. Phys.*, vol. 52, no. 1, pp. 24–34, 1983.
- [251] S. Miyamoto and P. A. Kollman, “Settle: An analytical version of the SHAKE and RATTLE algorithm for rigid water models,” *J. Comput. Chem.*, vol. 13, no. 8, pp. 952–962, Oct. 1992.
- [252] B. Hess, “P-LINCS: A parallel linear constraint solver for molecular simulation,” *J. Chem. Theory Comput.*, vol. 4, no. 1, pp. 116–122, 2008.
- [253] H. J. C. Berendsen, J. P. M. Postma, W. F. van Gunsteren, A. DiNola, and J. R. Haak, “Molecular dynamics with coupling to an external bath,” *J. Chem. Phys.*, vol. 81, no. 8, pp. 3684–3690, Oct. 1984.
- [254] S. Nosé, “A molecular dynamics method for simulations in the canonical ensemble,” *Mol. Phys.*, vol. 52, no. 2, pp. 255–268, Jun. 1984.
- [255] W. G. Hoover, “Canonical dynamics: Equilibrium phase-space distributions,” *Phys. Rev. A*, vol. 31, no. 3, pp. 1695–1697, Mar. 1985.
- [256] H. C. Andersen, “Molecular dynamics simulations at constant pressure and / or temperature,” *J. Chem. Phys.*, vol. 72, no. 2384, 1980.
- [257] M. Parrinello and A. Rahman, “Polymorphic transitions in single crystals: A new molecular dynamics method,” *J. Appl. Phys.*, vol. 52, no. 12, pp. 7182–7190, Dec. 1981.
- [258] L. Kiss and G. Láng, *Elektrokémia*. Budapest: Semmelweis Kiadó, 2011.
- [259] C. A. Reynolds and P. M. King, “Free energy calculations in molecular biophysics,” *Mol. Phys. An Int. J. Interface Between Chem. Phys.*, vol. 72, no. 2, pp. 251–275, 1992.

- [260] C. D. Christ, A. E. Mark, F. Wilfred, and A. N. Gunsteren, “Basic Ingredients of Free Energy Calculations : A Review,” *J. Comput. Chem.*, vol. 31, no. 8, pp. 1569–1582, 2009.
- [261] M. E. Tuckerman, *Statistical Mechanics: Theory and Molecular Simulation*. New York: Oxford University Press, 2010.
- [262] L. Sutto, M. D. Abramo, and F. L. Gervasio, “Comparing the Efficiency of Biased and Unbiased Molecular Dynamics in Reconstructing the Free Energy Landscape of Met-Enkephalin,” *J. Chem. Theory Comput.*, vol. 6, pp. 3640–3646, 2010.
- [263] T. Steinbrecher, R. Abel, A. Clark, and R. Friesner, “Free Energy Perturbation Calculations of the Thermodynamics of Protein Side-Chain Mutations,” *J. Mol. Biol.*, vol. 429, no. 7, pp. 923–929, 2017.
- [264] W. L. Jorgensen and L. L. Thomas, “Perspective on free-energy perturbation calculations for chemical equilibria,” *J. Chem. Theory Comput.*, vol. 4, no. 6, pp. 869–876, 2008.
- [265] A. V. Marenich, C. J. Cramer, and D. G. Truhlar, “Universal Solvation Model Based on Solute Electron Density and on a Continuum Model of the Solvent Defined by the Bulk Dielectric Constant and Atomic Surface Tensions,” *J. Phys. Chem. B*, vol. 113, no. 9, pp. 6378–6396, 2009.
- [266] A. V. Marenich, C. J. Cramer, and D. G. Truhlar, “Universal solvation model based on the generalized born approximation with asymmetric descreening,” *J. Chem. Theory Comput.*, vol. 5, no. 9, pp. 2447–2464, 2009.
- [267] J. F. Dama, M. Parrinello, and G. A. Voth, “Well-tempered metadynamics converges asymptotically,” *Phys. Rev. Lett.*, vol. 112, no. 24, pp. 1–6, 2014.
- [268] R. Vácha, P. Slavíček, M. Mucha, B. J. Finlayson-Pitts, and P. Jungwirth, “Adsorption of Atmospherically Relevant Gases at the Air/Water Interface: Free Energy Profiles of Aqueous Solvation of N<sub>2</sub>, O<sub>2</sub>, O<sub>3</sub>, OH, H<sub>2</sub>O, HO<sub>2</sub>, and H<sub>2</sub>O<sub>2</sub>,” *J. Phys. Chem. A*, vol. 108, no. 52, pp. 11573–11579, Dec. 2004.
- [269] A. Arslanargin and T. L. Beck, “Free energy partitioning analysis of the driving forces that determine ion density profiles near the water liquid-vapor interface,” *J. Chem. Phys.*, vol. 136, no. 10, p. 104503, 2012.
- [270] J. T. Fern, D. J. Keffer, and W. V. Steele, “Measuring coexisting densities from a two-phase molecular dynamics simulation by voronoi tessellations,” *J. Phys. Chem. B*, vol. 111, no. 13, pp. 3469–3475, 2007.
- [271] Z. B. Rózsa, B. Minofar, D. Řeha, B. Viskolcz, and M. Szóri, “From the vapor-liquid equilibrium to the supercritical condition. Molecular dynamics modeling of 1,3-butadiene,” *J. Mol. Liq.*, 2020.
- [272] S. Moodley, E. Johansson, K. Bolton, and D. Ramjugernath, “Gibbs ensemble Monte Carlo simulations of binary vapour–liquid–liquid equilibrium: application to n-hexane–water and ethane–ethanol systems,” *Mol. Simul.*, vol. 36, no. 10, pp. 758–762, 2010.
- [273] B. L. Eggimann *et al.*, “Assessing the Quality of Molecular Simulations for Vapor – Liquid Equilibria: An Analysis of the TraPPE Database,” *J. Chem. Eng. Data*, vol. 65, no. 3, pp. 1330–1344, 2020.
- [274] M. Lísal, W. R. Smith, and I. Nezbeda, “Accurate vapour – liquid equilibrium calculations for complex systems using the reaction Gibbs ensemble Monte Carlo simulation method,” *Fluid Phase Equilib.*, vol. 181, no. 1–2, pp. 127–146, 2001.
- [275] A. Lotfi, J. Vrabc, and J. Fischer, “Vapour liquid equilibria of the Lennard-Jones fluid from the NpT plus test particle method,” *Mol. Phys.*, vol. 76, no. 6, pp. 1319–1333, 1992.
- [276] G. Kronome, I. Szalai, M. Wendland, and J. Fischer, “Extension of the NpT + test particle method for the calculation of phase equilibria of nitrogen + ethane,” *J. Mol. Liq.*, vol. 85, pp. 237–247, 2000.
- [277] I. Szalai, D. Henderson, D. Boda, and K. Chan, “Thermodynamics and structural properties of the dipolar Yukawa fluid,” *J. Chem. Phys.*, vol. 111, no. 1, pp. 337–344, 1999.
- [278] M. C. Muniz, F. Paesani, T. E. Gartner, M. Riera, and C. Knight, “Vapor – liquid equilibrium

- of water with the MB-pol many-body potential Vapor – liquid equilibrium of water with the MB-pol many-body potential,” *J. Chem. Phys.*, vol. 154, pp. 211103-1–7, 2021.
- [279] D. Duque and L. F. Vega, “Some issues on the calculation of interfacial properties by molecular simulation Some issues on the calculation of interfacial properties by molecular simulation,” *J. Chem. Phys.*, vol. 121, no. 17, pp. 8611–8617, 2004.
- [280] E. L. Granados-Bazán, S. E. Quiñones-Cisneros, and U. K. Deiters, “Interfacial properties of binary mixtures of Lennard-Jones chains in planar interfaces by molecular dynamics simulation Interfacial properties of binary mixtures of Lennard-Jones chains in planar interfaces by molecular dynamics simulation,” *J. Chem. Phys.*, vol. 154, p. 084704, 2021.
- [281] J. C. Pàmies, C. McCabe, P. T. Cummings, and L. F. Vega, “Coexistence Densities of Methane and Propane by Canonical Molecular Dynamics and Gibbs Ensemble Monte Carlo Simulations Coexistence Densities of Methane and Propane by Canonical Molecular Dynamics and Gibbs Ensemble Monte Carlo Simulations,” *Mol. Simul.*, vol. 29, no. 6–7, pp. 463–470, 2003.
- [282] F. Aurenhammer, “Voronoi diagrams - a survey of a fundamental geometric data structure,” *ACM Comput. Surv.*, vol. 23, no. 3, pp. 345–405, 1991.
- [283] K. M. Merz and B. Roux, *Biological membranes: a molecular perspective from computation and experiment*. Boston: Birkhauser, 1996.
- [284] C. J. Dickson, L. Rosso, R. M. Betz, R. C. Walker, and I. R. Gould, “GAFFlipid: a General Amber Force Field for the accurate molecular dynamics simulation of phospholipid,” *Soft Matter*, vol. 8, no. 37, p. 9617, 2012.
- [285] D. Poger, B. Caron, and A. E. Mark, “Validating lipid force fields against experimental data: Progress, challenges and perspectives,” *Biochim. Biophys. Acta - Biomembr.*, vol. 1858, no. 7, pp. 1556–1565, 2016.
- [286] W. Shinoda and S. Okazaki, “A Voronoi analysis of lipid area fluctuation in a bilayer,” *J. Chem. Phys.*, vol. 109, no. 4, pp. 1517–1521, 1998.
- [287] G. Lukat, J. Kru, and B. Sommer, “APL @ Voro : A Voronoi-Based Membrane Analysis Tool for GROMACS Trajectories,” *J. Chem. Inf. Model.*, vol. 53, no. 11, pp. 2908–2925, 2013.
- [288] T. Mori, F. Ogushi, and Y. Sugita, “Analysis of lipid surface area in protein-membrane systems combining voronoi tessellation and monte carlo integration methods,” *J. Comput. Chem.*, vol. 33, no. 3, pp. 286–293, 2012.
- [289] S. Y. Cheng, H. V Duong, C. Compton, M. W. Vaughn, H. Nguyen, and K. H. Cheng, “Characterization of 3D Voronoi tessellation nearest neighbor lipid shells provides atomistic lipid disruption profile of protein containing lipid membranes,” *Biophys. Chem.*, vol. 198, pp. 22–35, 2015.
- [290] D. Exerowa and D. Kashchiev, “Hole-mediated stability and permeability of bilayers,” *Contemp. Phys.*, vol. 27, no. 5, pp. 429–461, 1986.
- [291] H. Trauble, “The Movement of Molecules Across Lipid Membranes: A Molecular Theory,” *J. Membr. Biol.*, vol. 4, pp. 193–208, 1971.
- [292] G. Van Rossum, *Python tutorial*. Amsterdam: Technical Report CS-R9526, 1995.
- [293] N. Michaud-Agrawal, J. E. Denning, T. B. Woolf, and O. Beckstein, “MDAnalysis: A Toolkit for the Analysis of Molecular Dynamics Simulations,” *J. Comput. Chem.*, vol. 32, pp. 2319–2327, 2011.
- [294] J. D. Bernal, “A Geometrical Approach to the Structure Of Liquids,” *Nature*, vol. 183, pp. 141–147, 1959.
- [295] S. W. Sloan, “A fast algorithm for constructing Delaunay triangulations in the plane,” *Adv. Eng. Softw.*, vol. 9, no. 1, pp. 34–55, 1987.
- [296] G. Cevc, *Phospholipids Handbook*. New York: Marcel Decker, Inc., 1993.
- [297] W. Humphrey, A. Dalke, and K. Schulten, “VMD: Visual Molecular Dynamics,” *J. Mol.*

- Graph.*, vol. 14, no. 1, pp. 33–38, 1996.
- [298] G. A. Tribello, M. Bonomi, D. Branduardi, C. Camilloni, and G. Bussi, “PLUMED 2 : New feathers for an old bird,” *Comput. Phys. Commun.*, vol. 185, no. 2, pp. 604–613, 2014.
- [299] M. Bonomi *et al.*, “PLUMED : A portable plugin for free-energy calculations with molecular,” *Comput. Phys. Commun.*, vol. 180, no. 10, pp. 1961–1972, 2009.
- [300] E. L. Wu *et al.*, “CHARMM-GUI Membrane Builder - Toward realistic biological membrane simulations,” *J. Comput. Chem.*, vol. 35, no. 27, pp. 1997–2004, Oct. 2014.
- [301] J. Lee *et al.*, “CHARMM-GUI Input Generator for NAMD, GROMACS, AMBER, OpenMM, and CHARMM/OpenMM Simulations Using the CHARMM36 Additive Force Field,” *J. Chem. Theory Comput.*, vol. 12, no. 1, pp. 405–413, Jan. 2016.
- [302] A. Khondker *et al.*, “Partitioning of caffeine in lipid bilayers reduces membrane fluidity and increases membrane thickness,” *Phys. Chem. Chem. Phys.*, vol. 19, no. 10, pp. 7101–7111, 2017.
- [303] M. Ganjali Koli and K. Azizi, “The partition and transport behavior of cytotoxic ionic liquids (ILs) through the DPPC bilayer: Insights from molecular dynamics simulation,” *Mol. Membr. Biol.*, vol. 33, no. 3–5, pp. 64–75, 2016.
- [304] Z. B. Rózsa, L. J. Németh, B. Jójárt, K. Nehéz, B. Viskolcz, and M. Szöri, “Molecular Dynamics and Metadynamics Insights of 1,4-Dioxane-Induced Structural Changes of Biomembrane Models,” *J. Phys. Chem. B*, vol. 123, no. 37, pp. 7869–7884, 2019.
- [305] K. J. Oh and M. L. Klein, “Effects of Halothane on Dimyristoylphosphatidylcholine Lipid Bilayer Structure : A Molecular Dynamics Simulation Study,” *Korean Chem. Soc.*, vol. 30, no. 9, pp. 2087–2092, 2009.
- [306] W. L. Jorgensen, J. Chandrasekhar, J. D. Madura, R. W. Impey, and M. L. Klein, “Comparison of simple potential functions for simulating liquid water,” *J. Chem. Phys.*, vol. 79, no. 2, pp. 926–935, Jul. 1983.
- [307] K. Vanommeslaeghe *et al.*, “CHARMM general force field: A force field for drug-like molecules compatible with the CHARMM all-atom additive biological force fields,” *J. Comput. Chem.*, vol. 31, no. 4, pp. 671–690, Mar. 2010.
- [308] A. J. Metso, A. Jutila, J. P. Mattila, J. M. Holopainen, and P. K. J. Kinnunen, “Nature of the main transition of dipalmitoylphosphocholine bilayers inferred from fluorescence spectroscopy,” *J. Phys. Chem. B*, vol. 107, no. 5, pp. 1251–1257, 2003.
- [309] J. Suurkuusk, B. R. Lentz, Y. Barenholz, R. L. Biltonen, and T. E. Thompson, “A Calorimetric and Fluorescent Probe Study of the Gel-Liquid Crystalline Phase Transition in Small, Single-Lamellar Dipalmitoylphosphatidylcholine Vesicles,” *Biochemistry*, vol. 15, no. 7, pp. 1393–1401, 1976.
- [310] R. L. Biltonen and D. Lichtenberg, “The use of differential scanning calorimetry as a tool to characterize liposome preparations,” *Chem. Phys. Lipids*, vol. 64, no. 1–3, pp. 129–142, 1993.
- [311] U. Essmann, L. Perera, M. L. Berkowitz, T. Darden, H. Lee, and L. G. Pedersen, “A smooth particle mesh Ewald method,” *J. Chem. Phys.*, vol. 103, no. 19, pp. 8577–8593, Nov. 1995.
- [312] A. Maciejewski, M. Pasenkiewicz-Gierula, O. Cramariuc, I. Vattulainen, and T. Rog, “Refined OPLS all-atom force field for saturated phosphatidylcholine bilayers at full hydration,” *J. Phys. Chem. B*, vol. 118, no. 17, pp. 4571–4581, 2014.
- [313] L. S. Dodda, I. C. De Vaca, J. Tirado-Rives, and W. L. Jorgensen, “LigParGen web server: An automatic OPLS-AA parameter generator for organic ligands,” *Nucleic Acids Res.*, vol. 45, no. W1, pp. W331–W336, 2017.
- [314] L. S. Dodda, J. Z. Vilseck, J. Tirado-Rives, and W. L. Jorgensen, “1.14\*CM1A-LBCC: Localized Bond-Charge Corrected CM1A Charges for Condensed-Phase Simulations,” *J. Phys. Chem. B*, vol. 121, no. 15, pp. 3864–3870, 2017.
- [315] W. L. Jorgensen, J. Tirado-rives, and F. Fields, “Potential energy functions for atomic-level simulations of water and organic and biomolecular systems,” *PNAS*, vol. 102, no. 19, pp. 6665–6670, 2005.

- [316] D. Shivakumar, J. Williams, Y. Wu, W. Damm, J. Shelley, and W. Sherman, "Prediction of Absolute Solvation Free Energies using Molecular Dynamics Free Energy Perturbation and the," *J. Chem. Theory Comput.*, vol. 6, pp. 1509–1519, 2010.
- [317] B. Anantharaman and C. F. Melius, "Bond additivity corrections for G3B3 and G3MP2B3 quantum chemistry methods," *J. Phys. Chem. A*, vol. 109, no. 8, pp. 1734–47, Mar. 2005.
- [318] A. G. Baboul, L. a. Curtiss, P. C. Redfern, and K. Raghavachari, "Gaussian-3 theory using density functional geometries and zero-point energies," *J. Chem. Phys.*, vol. 110, no. 16, p. 7650, 1999.
- [319] C. Y. Peng, P. Y. Ayala, H. B. Schlegel, and M. J. Frisch, "Using redundant internal coordinates to optimize equilibrium geometries and transition states," *J. Comput. Chem.*, vol. 17, pp. 49–56, 1996.
- [320] Y. Deng and R. Benoit, "Hydration of Amino Acid Side Chains: Nonpolar and Electrostatic Contributions Calculated from Staged Molecular Dynamics Free Energy Simulations with Explicit Water Molecules," *J. Phys. Chem. B*, vol. 108, no. 42, pp. 16567–16576, 2004.
- [321] C. H. Bennett, "Efficient Estimation of Free Energy Differences from Monte Carlo Data," *JOURNAL. Comput. Phys.*, vol. 22, no. 2, pp. 245–268, 1976.
- [322] J. Hine and P. K. Mookerjee, "The Intrinsic Hydrophilic Character of Organic Compounds. Correlations in Terms of Structural Contributions," *J. Org. Chem.*, vol. 40, no. 3, pp. 292–298, 1975.
- [323] R. Wolfenden, Y.-L. Liang, M. Matthews, and R. Williams, "Cooperativity and Anticooperativity in Solvation by Water: Imidazoles, Quinones, Nitrophenols, Nitrophenolate, and Nitrothiophenolate Ions," *J. Am. Chem. Soc.*, vol. 109, no. 2, pp. 463–466, 1987.
- [324] W. Z. Ou-Yang, Z. Y. Lu, T. F. Shi, Z. Y. Sun, and L. J. An, "A molecular-dynamics simulation study on the dependence of Lennard-Jones gas-liquid phase diagram on the long-range part of the interactions," *J. Chem. Phys.*, vol. 123, no. 23, 2005.
- [325] J.-P. Douliez, A. Léonard, and E. J. Dufourc, "Restatement of order parameters in biomembranes: calculation of C-C bond order parameters from C-D quadrupolar splittings," *Biophys. J.*, vol. 68, no. 5, pp. 1727–1739, 1995.
- [326] "Dortmund Data Bank," 2019. [Online]. Available: <http://www.ddbst.com>. [Accessed: 04-Sep-2019].
- [327] A. Klamt, "COSMO-RS for aqueous solvation and interfaces," *Fluid Phase Equilib.*, vol. 407, pp. 152–158, Jan. 2016.
- [328] J. Comer, K. Schulten, and C. Chipot, "Permeability of a Fluid Lipid Bilayer to Short-Chain Alcohols from First Principles," *J. Chem. Theory Comput.*, vol. 13, no. 6, pp. 2523–2532, 2017.
- [329] B. L. Lee and K. Kuczera, "Simulating the free energy of passive membrane permeation for small molecules," *Mol. Simul.*, vol. 44, no. 13–14, pp. 1147–1157, 2018.
- [330] P. Kumari, S. Kaur, S. Sharma, and H. K. Kashyap, "Impact of amphiphilic molecules on the structure and stability of homogeneous sphingomyelin bilayer: Insights from atomistic simulations," *J. Chem. Phys.*, vol. 148, p. 165102, 2018.
- [331] W. Shinoda, "Permeability across lipid membranes," *Biochim. Biophys. Acta - Biomembr.*, vol. 1858, no. 10, pp. 2254–2265, 2016.
- [332] D. Poger and A. E. Mark, "On the Validation of Molecular Dynamics Simulations of Saturated and cis -Monounsaturated Phosphatidylcholine Lipid Bilayers : A Comparison with Experiment," *J. Chem. Theory Comput.*, vol. 6, pp. 325–336, 2010.
- [333] S. O. Yesylevskyy and C. Ramseyer, "Determination of mean and Gaussian curvatures of highly curved asymmetric lipid bilayers: The case study of the influence of cholesterol on the membrane shape," *Phys. Chem. Chem. Phys.*, vol. 16, no. 32, pp. 17052–17061, 2014.
- [334] S. J. Marrink and H. J. C. Berendsen, "Permeation process of small molecules across lipid membranes studied by molecular dynamics simulations," *J. Phys. Chem.*, vol. 100, no. 95,

- pp. 16729–16738, 1996.
- [335] K. Ohki, K. Tamura, and I. Hatta, “Ethanol induces interdigitated gel phase (LBI) between lamellar gel phase (LB,) and ripple phase in phosphatidylcholine membranes : a scanning density meter study,” *Biochim. Biophys. Acta*, vol. 1028, pp. 215–222, 1990.
- [336] L. G. M. Basso, R. Z. Rodrigues, R. M. Z. G. Naal, and A. J. Costa-filho, “Effects of the antimalarial drug primaquine on the dynamic structure of lipid model membranes,” *BBA - Biomembr.*, vol. 1808, no. 1, pp. 55–64, 2011.
- [337] C. Matsingou and C. Demetzos, “Calorimetric study on the induction of interdigitated phase in hydrated DPPC bilayers by bioactive labdanes and correlation to their liposome stability The role of chemical structure,” *Chem. Phys. Lipids*, vol. 145, pp. 45–62, 2007.
- [338] V. I. Gordeliy, M. A. Kiselev, P. Lesieur, A. V. Pole, and J. Teixeira, “Lipid Membrane Structure and Interactions in Dimethyl Sulfoxide / Water Mixtures,” *Biophys. J.*, vol. 75, no. 5, pp. 2343–2351, 1998.
- [339] J. P. M. Jambeck and A. P. Lyubartsev, “Exploring the Free Energy Landscape of Solutes Embedded in Lipid Bilayers,” *J. Phys. Chem. Lett.*, vol. 4, pp. 1781–1787, 2013.
- [340] H. Lu and J. Marti, “Cellular absorption of small molecules: free energy landscapes of melatonin binding at phospholipid membranes,” *Sci. Rep.*, vol. 10, no. 1, p. 9235, Dec. 2020.
- [341] J. Juracka, M. Srejber, M. Meliková, V. Bazgier, and K. Berka, “MolMeDB: Molecules on Membranes Database,” *Database*, vol. 2019, p. baz078, 2019.
- [342] F. J. Wegner, “Corrections to scaling laws,” *Phys. Rev. B*, vol. 5, no. 11, pp. 4529–4536, 1972.
- [343] C. Vega, J. L. F. Abascal, and I. Nezbeda, “Vapor-liquid equilibria from the triple point up to the critical point for the new generation of TIP4P-like models: TIP4P/Ew, TIP4P/2005, and TIP4P/ice,” *J. Chem. Phys.*, vol. 125, no. 3, 2006.
- [344] B. Fábíán, G. Horvai, A. Idrissi, and P. Jedlovszky, “Vapour-liquid equilibrium of acetone-CO<sub>2</sub> mixtures of different compositions at the vicinity of the critical point,” *J. CO<sub>2</sub> Util.*, vol. 34, no. July, pp. 465–471, 2019.
- [345] M. Ley-Koo and M. S. Green, “Consequences of the Renormalization Group for the Thermodynamics of Fluids Near the Critical Point,” *Phys. Rev. A*, vol. 23, no. 5, pp. 2650–2659, 1981.
- [346] S. Reif-Acherman, “The History of the Rectilinear Diameter Law,” *Quim. Nova*, vol. 33, no. 9, pp. 2003–2010, 2010.
- [347] A. Pelissetto and E. Vicari, “Critical phenomena and renormalization-group theory,” *Phys. Rep.*, vol. 368, no. 6, pp. 549–727, 2002.
- [348] M. G. Martin and J. I. Siepmann, “Transferable potentials for phase equilibria. 1. United-atom description of n-alkanes,” *J. Phys. Chem. B*, vol. 102, no. 14, pp. 2569–2577, 1998.
- [349] OriginLab Corporation, “OriginPro, Version 2018.” Northampton, MA, USA.
- [350] P. T. Boggs, C. H. Spiegelman, J. R. Donaldson, and R. B. Schnabel, “A Computational Examination of Orthogonal Distance Regression,” *J. Econom.*, vol. 38, pp. 169–201, 1988.
- [351] C. Tsonopoulos, E. Company, P. O. Box, and F. Park, “Vapor-Liquid Critical Properties of Elements and Compounds. 6 . Unsaturated Aliphatic Hydrocarbons Constantine,” *J. Chem. Eng. Data*, vol. 41, no. 4, pp. 645–656, 1996.
- [352] European Chemicals Bureau, “European Union Risk Assessment Report - 1,3-BUTADIENE,” Luxembourg, 2002.
- [353] R. A. Horváth, B. Fábíán, M. Sz, and P. Jedlovszky, “Investigation of the liquid-vapour interface of aqueous methylamine solutions by computer simulation methods ☆,” *J. Mol. Liq.*, vol. 288, p. 110978, 2019.
- [354] B. Kiss, B. Fábíán, A. Idrissi, M. Sz, and P. Jedlovszky, “Investigation of the Liquid-Vapor Interface of Water-Formamide Mixtures by Computer Simulation and Intrinsic Surface Analysis Investigation of the Liquid-Vapor Interface of Water- Formamide Mixtures by

- Computer Simulation and Intrinsic Surface Analysis,” *J. Phys. Chem. C*, vol. 122, no. 34, pp. 19639–19651, 2018.
- [355] M. Abraham, M. C. Abraham, and I. Ziogas, “Surface Tension of Liquids from Molten Nitrate Mixtures to Water,” *J. Am. Chem. Soc.*, vol. 113, no. 23, pp. 8583–8590, 1991.
- [356] F. Eisenhaber, P. Lijnzaad, P. Argos, and C. Sander, “The Double Cubic Lattice Method : Efficient Approaches to Numerical Integration of Surface Area and Volume and to Dot Surface Contouring of Molecular Assemblies,” *J. Comput. Chem.*, vol. 16, no. 3, pp. 273–284, 1995.

## 9 LIST OF PUBLICATIONS

### Publications related to the subject of the dissertation:

**Rózsa, Zsófia Borbála;** Németh, Lukács József; Jójárt, Balázs; Nehéz, Károly; Viskolcz, Béla; Szőri, Milán

Molecular Dynamics and Metadynamics Insights of 1,4-Dioxane-Induced Structural Changes of Biomembrane Models

JOURNAL OF PHYSICAL CHEMISTRY B: acs.jpcc.9b04313 (2019)

**Rózsa, Zsófia Borbála;** Minofar, Babak; Řeha, David; Viskolcz, Béla; Szőri, Milán

From the vapor-liquid equilibrium to the supercritical condition. Molecular dynamics modeling of 1,3-butadiene

JOURNAL OF MOLECULAR LIQUIDS 315, 113702 (2020)

**Rózsa, Zsófia Borbála;** Szőri-Dorogházi, Emma; Viskolcz, Béla; Szőri, Milán

Transmembrane penetration mechanism of cyclic pollutants inspected by molecular dynamics and metadynamics: the case of morpholine, phenol, 1,4-dioxane and oxane

PHYSICAL CHEMISTRY CHEMICAL PHYSICS: 28. 15338-15351. 14 p. (2021)

**Rózsa Zsófia Borbála;** Thangaraj Ravikumar; Viskolcz Béla; Szőri Milán

Foreseeing the future of green Technology. Molecular dynamic investigation on passive membrane penetration by the products of the CO<sub>2</sub> and 1,3-butadiene reaction

JOURNAL OF MOLECULAR LIQUIDS 361, 1, 119581. (2022)

### Further publications

Cheikh, Wafaa ; **Rózsa, Zsófia Borbála;** Camacho López, Christian Orlando; Mizsey, Péter; Viskolcz, Béla; Szőri, Milán; Fejes, Zsolt

Urethane Formation with an Excess of Isocyanate or Alcohol: Experimental and Ab Initio Study

POLYMERS 11 : 10 p. 1543 , 11 p. (2019)

Illés, Ádám; **Rózsa, Zsófia Borbála;** Thangaraj, Ravikumar; Décsiné Gombos, Erzsébet; Dóbé, Sándor; Giri, Binod Raj; Szőri, Milán

An experimental and theoretical kinetic study of the reactions of hydroxyl radicals with tetrahydrofuran and two deuterated tetrahydrofurans

CHEMICAL PHYSICS LETTERS 776 Paper: 138698 , 7 p. (2021)

### Presentations related to the dissertation

5th Visegrad Symposium on Structural Systems Biology (Szeged, Magyarország) 2015

*Mapping out the 366 shades of the C<sub>4</sub>H<sub>8</sub>O<sub>2</sub> isomers*

8th Visegrad Symposium on Structural Systems Biology (Losonc, Slovakia) 2018

*Dioxane-induced changes on the interfacial region of phosphatidyl-choline membranes*

KeMoMo-QSAR Szimpózium (Szeged, Hungary) 2019

*Az 1,3-butadién strukturális változásainak megértése molekuláris szinten a gőz-folyadék egyensúlytól a szuperkritikus állapotig*

Eötvös-Symposium (Miskolc, Hungary) 2019

*Molecular Understanding of Structural Changes of 1,3-Butadiene from Vapor-Liquid Equilibrium to Supercritical Conditions*

9th Visegrad Symposium on Structural Systems Biology (Szilvásvárad, Hungary) 2019

*Molecular Dynamics and Metadynamics Insights of 1,4-Dioxane Induced Structural Changes of Biomembrane Models*

10th Visegrad Symposium on Structural Systems Biology (Nové Hradý, Czech Republic) 2022

*Molecular-level understanding of membrane permeation of some chemicals*

### **Further Presentations**

Annual Summer School in Molecular Biophysics and Systems Biology (Nové Hradý, Czech Republic) 2018

*The effect of fatty acids on the conformation of protein channel TRAAK*

### **Posters related to the dissertation**

7th Visegrad Symposium on Structural Systems Biology (Nové Hradý, Czech Republic) 2017

*A molecular dynamics study on the effects of 1,4-dioxane on model membranes*

### **Further posters**

4th Visegrad Symposium on Structural Systems Biology (Nové Hradý, Czech Republic) 2014

*A theoretical analysis on the thermodynamic stability of various constitutional isomers of C<sub>4</sub>H<sub>8</sub>O<sub>2</sub>*